University of Kentucky Master's Theses　　　　　　　　　　　Graduate School

2003

ANALYSIS AND APPLICATION OF CAPACITIVE DISPLACEMENT SENSORS TO CURVED SURFACES

Philip T. Smith Jr.
University of Kentucky, psmith@engr.uky.edu

Abstract of Thesis

ANALYSIS AND
APPLICATION OF
CAPACITIVE DISPLACEMENT SENSORS TO
CURVED SURFACES

Capacitive displacement sensors have many applications where non-contact, high precision measurement of a surface is required. Because of their non-contact nature they can easily measure conductive surfaces that are flexible or otherwise unable to be measured using a contact probe. Since the output of the capacitance gage is electrical, data points can be collected quickly and averaged to improve statistics.

It is often necessary for capacitive displacement sensors to gage the distance from a curved (non-flat) surface. Although displacements can easily be detected, the calibration of this output can vary considerably from the flat case. Since a capacitance gage is typically factory-calibrated against a flat reference, the experimental output contains errors in both gain and linearity. A series of calibration corrections is calculated for rectifying this output.

Capacitance gages are also limited in their overall displacement travel. A support stage is described that, along with control electronics, allow the properties of the capacitance gage to be combined with an interferometer to overcome this displacement limitation. Finally, an application is proposed that would make use of the capacitance sensor and support stage assembly.

KEYWORDS: Capacitance gage, electric field, finite element analysis, gossamer mirror

Philip T. Smith Jr.

October 5, 2003

ANALYSIS AND
APPLICATION OF
CAPACITIVE DISPLACEMENT SENSORS TO
CURVED SURFACES

By

Philip T. Smith Jr.

Dr. R. Ryan Vallance
Director of Thesis

Dr. George Huang
Director of Graduate Studies

October 5, 2003

Rules for the Use of Theses

Unpublished theses submitted for the Master's degree and deposited in the University of Kentucky Library are as a rule open for inspection, but are to be used only with due regard to the rights of the authors. Bibliographical references may be noted, but quotations or summaries of parts may be published only with the permission of the author, and with the usual scholarly acknowledgments.

Extensive copying or publication of the thesis in whole or in part also requires the consent of the Dean of the Graduate School of the University of Kentucky.

THESIS

Philip T. Smith Jr.

The Graduate School

University of Kentucky

2003

ANALYSIS AND
APPLICATION OF
CAPACITIVE DISPLACEMENT SENSORS TO
CURVED SURFACES

_____

THESIS

_____

A thesis submitted in partial fulfillment of the requirements for the degree of
MSME in the College of Engineering at the University of Kentucky

By

Philip T. Smith Jr.

Lexington, Kentucky

Director: Dr. R. R. Vallance, Assistant Professor of Mechanical Engineering

Lexington, Kentucky

2003

Acknowledgements

From my first visit to the University of Kentucky in the spring of 2000 until now I have been granted an astonishing level of access to the faculty of the Mechanical Engineering department, and for this I am tremendously grateful. At the top of this list belongs Dr. Ryan Vallance, who has been extremely flexible when both my research and my scheduling have taken abrupt directional changes. Over three years he has given me many of the building blocks from which I have been able to construct this work.

I would also like to thank Dr. Suzanne Smith, who tolerated a great deal of programming questions, usually asked at the eleventh hour. Dr. Eric Marsh of the Pennsylvania State University looked at many convoluted interpretations of the data in Chapters 2 and 3 before several sources of error were eliminated. Dr. Bruce Walcott set the bar very high both in his teaching and in his expectations, and it was a tremendous challenge keeping up. Thanks also to Dr. Pinar Mengüç, who tolerated several early morning *gedanken* experiments over bagels.

Finally, I would like to thank my wife, Jana Riess, for her unwavering support of my efforts at continuing my education. Without her words of encouragement and her understanding of the writing process, I would never have made it this far. Words cannot thank her enough.

Table of Contents

List of Tables

List of Figures

List of Files

Filename	Size
ptsmith.pdf	4.5 Mbytes

1: Introduction

Capacitance displacement sensors or "gages" are used in precision engineering applications such as metrology (dimensional, form, and machine) and precision machines. Capacitance gages are suitable for these applications since they provide high sensitivity, non-contact measurement, and a wide range of bandwidths. Engineers often assume that their displacement sensor measurements are perfectly linear and calibrated irrespective of operating conditions, but in many situations this is not the case. In particular a capacitance displacement gage will show erroneous output when it is used in combination with a convex spherical surface rather than a flat surface. The errors arising from this operating condition can be significant in several common applications.

The calibration of capacitance gages changes when comparing output from flat versus spherical surfaces due to the change in capacitances within the system. These changes will be modeled using finite element software, and the resulting data will be used to create "error maps" for specific diameter spheres. Finally, these error maps will be proven to be valid by applying the theoretical corrections to experimental results.

Another capacitance gage limitation, that of a small overall sensing range, can be overcome by combining the capacitance gage with a second displacement sensor. This assembly can be electronically controlled to maintain a constant distance from a target surface, and a machine is proposed that takes advantage of such a subassembly. The control subassembly will be validated experimentally using equipment available in the laboratory.

This chapter begins by introducing the fundamentals of capacitance displacement gages and a few common applications. These applications include piezo feedback in nanopositioning stages and spindle metrology measurements. Second, this chapter will open the "black box" and look at some of the electronic and electrostatic issues involved with capacitance gages, including closed-form approximations and linearity considerations.

1.1 Capacitance Sensors Overview

Capacitance is the property of a conductor or a system of conductors to store and release energy by storing electrons. The fundamental relationship between charge Q, capacitance C, and voltage potential V, is given by Eq. (1-1). The energy stored in a capacitor is given by Eq. (1-2). From these equations it is apparent that the charge and therefore energy storage ability goes up as capacitance increases.

$$Q = C \cdot V$$

(1-1)

$$W = \tfrac{1}{2} C V^2$$

(1-2)

Because electrons are naturally repelled by each other and are drawn to positive charges (i.e., a material with a dearth of electrons), the most common capacitor arrangements have two conductive plates separated by only a thin layer of insulator (dielectric). When one plate is charged negatively and the other charged positively, many more electrons can be stored since the electrons on the negative plate are drawn to the holes on the positively charged plate. A smaller gap between the plates produces a higher capacitance. If the gap distance is variable, the capacitance between the two plates will vary as well.

Commercially available capacitance sensors utilize either a varying gap or varying area to change their capacitance as a function of displacement. They are used in applications requiring high sensitivity, non-contact displacement measurement. In nearly all commercial capacitance gage applications the gage is placed in close proximity to a conductive target surface that is electrically grounded. During operation, an AC circuit at a frequency of a few kHz modulates the voltage on the "sensing" conductor and determines its capacitance relative to the grounded plane. Figure 1-1 shows a commercially available capacitance displacement sensor that is manufactured and sold by Lion Precision, Inc. (Minneapolis, MN). On this sensor the central conductor or "sensing element" is ground flat and perpendicular to the housing. This conductor is separated from the "guard ring" by an insulating material. The guard ring is kept at approximately the same potential voltage as the sensing element, but is not part of the sensing circuit. This guard ring geometry minimizes the spreading or "fringe effects" of the electric field near the edges of the sensing element, as will be discussed in detail in Chapter 2. By minimizing the fringing the linearity is improved and the gage is also somewhat protected from spurious external electric

fields from other voltage sources. The dimensions of the capacitance gage conductors and insulators are shown in Figure 1-2.
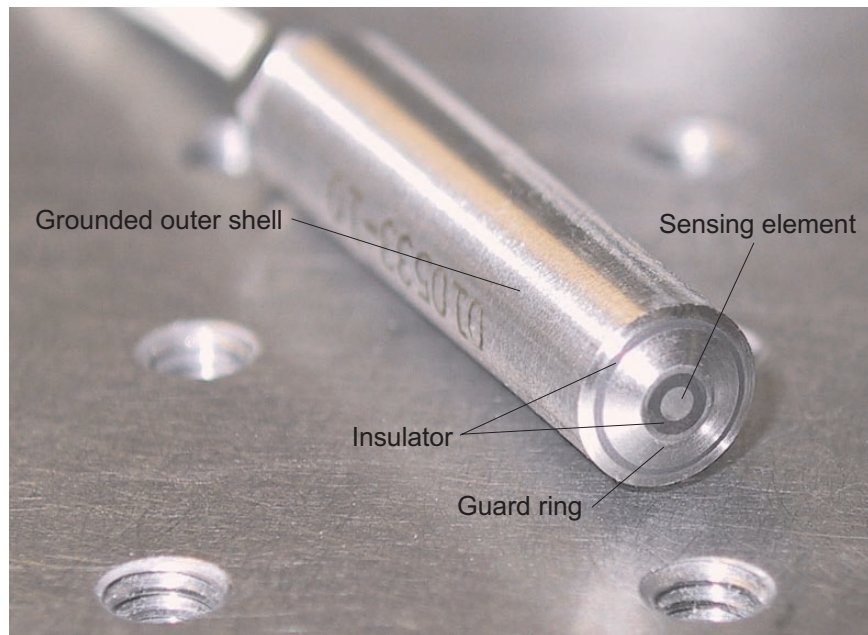
Figure 1-1. Lion Precision capacitance gage with key components labeled.
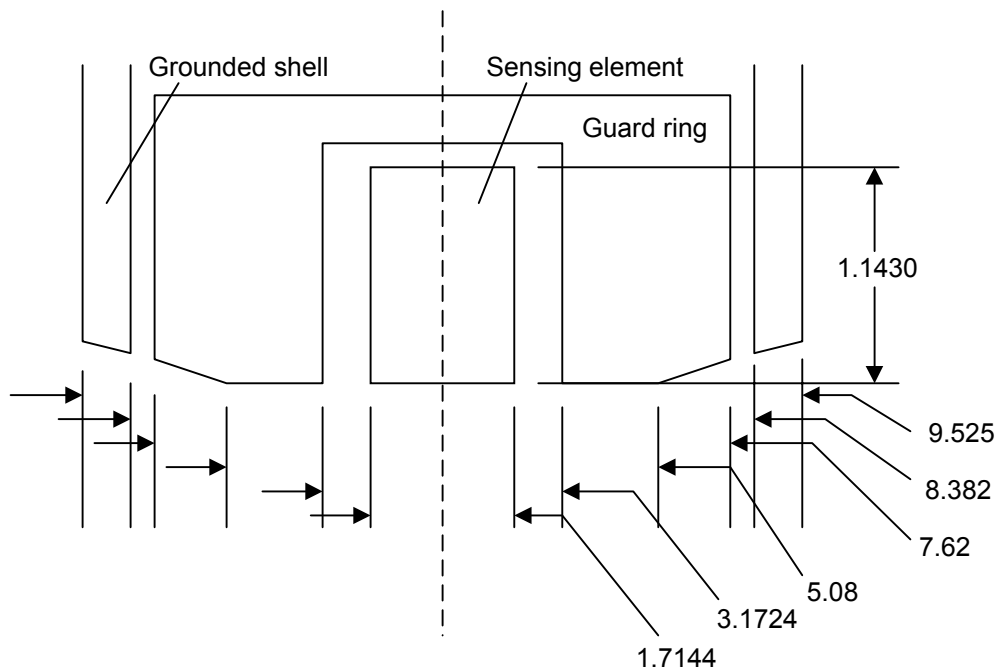
Figure 1-2. Cross section of capacitance sensor. All dimensions in mm.

1.1.1 Closed-form approximate solutions

The capacitance of an idealized parallel plate capacitor has a simple closed-form solution, shown in Eq. (1-3). The capacitance C is directly proportional to the surface area A of each plate, the electric field permittivity of free space ε_0, and the relative permittivity of the insulator between the plates ε_R. The capacitance C is inversely proportional to the distance d between the plates. This formulation is considered only a first order approximation since it neglects fringe effects and any thickness of the plates. It assumes that the electric field is perfectly uniform across the gap between the plates and is zero elsewhere. Graphically, the electric field lines are perpendicular to the surfaces of the plates and have equal magnitude. The equipotential lines (constant voltage) are parallel to the plates and occur at equal spacing.

$$C = \frac{\varepsilon_0 \varepsilon_R A}{d} \tag{1-3}$$

In the unit system (mm, V) applied throughout the capacitance calculations and field simulations of this thesis, the absolute permittivity, ε_0, equals 8.854×10^{-9} $\mu F/mm$. The resulting capacitance values calculated with Eq. (1-3) are therefore in units of μF, which are sometimes converted to picoFarads (pF) for simplicity. The relative permittivity ε_R is a dimensionless quantity greater than 1 that relates the permittivity of the medium between the plates to that of vacuum. Hicks and Atherton [1] suggest using Essen and Froome's [2] relation, which is given in Eq. (1-4), to calculate the relative permittivity of air as a function of temperature T and the partial pressures of dry air (p_1), carbon dioxide (p_2), and water vapor (p_3) in the atmosphere. A typical value for relative permittivity at room temperature is 1.0008, but it will be shown in Section 3.3.3 that this can be assumed to be 1 with no loss of accuracy in the final calculations.

$$\varepsilon_R - 1 = \left[\frac{1553.9}{T} p_1 + \frac{2663.6}{T} p_2 + \frac{1295.2}{T} \left(1 + \frac{5748}{T} \right) p_3 \right] \times 10^{-6} \tag{1-4}$$

The expression for ideal capacitance in Eq. (1-3) is only a first order approximation since it neglects fringe effects and any thickness of the plates. It assumes that the electric field is perfectly uniform across the gap between the plates and zero elsewhere. The electric field lines

are perpendicular to the surfaces of the plates and have equal magnitude, and the equipotential lines (constant voltage) are parallel to the plates and occur at equal spacing. Because the effective area of the plates is increased by fringing at the perimeter of the plates, the actual capacitance is always larger than what Eq. (1-3) suggests; hence the ideal capacitance underestimates the capacitance of the actual system.

A more accurate estimate of the capacitance between two parallel circular plates includes the effect of the electrical field fringing around the perimeter of the plates. Lion [3] suggests that Eq. (1-5) be used to determine a capacitance value C_f that includes fringe effects. The correction factor f in this equation is a function of the plate thickness, s, and the gap distance, d. The value of f is determined from Table 1-1 for a given ratio of plate thickness to gap distance (s/d) [4].

$$C_f = \varepsilon_0 \left\{ \frac{\pi r^2}{d} + r \left[\ln \frac{16 \pi r}{d} + 1 + f \right] \right\}$$
(1-5)

Table 1-1. Fringe effect correction factor f for Eq. (1-5).

s/d	f(s/d)	s/d	f(s/d)
0.02	0.098	0.4	0.84
0.04	0.168	0.6	1.06
0.06	0.230	0.8	1.24
0.08	0.285	1.0	1.39
0.1	0.335	1.2	1.52
0.2	0.54	1.4	1.63

Moon and Sparks [5] provide a third closed-form approximation for the capacitance when the capacitor consists of two thin circular plates with an annular Kelvin guard ring surrounding one plate to reduce fringe effects. This configuration is illustrated in Figure 1-3, where r is the radius of the upper plate and g is the gap between it and the guard ring. This approximation is valid under three conditions: (1) the plates and guard ring are thin, (2) the gap between the upper plate and guard ring (g) is much smaller than the distance between the plates ($g<<d$), and (3) when the width of the guard ring w is about 5 times greater than the distance between the plates ($w \approx 5 \cdot d$).
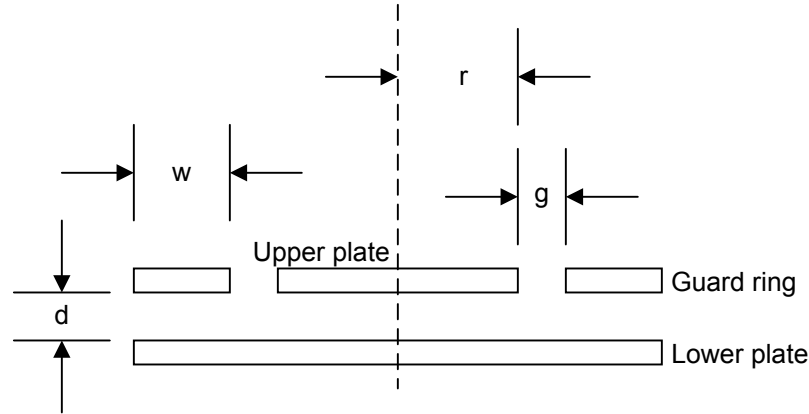
Figure 1-3. Geometry for the Kelvin guard ring approximation.

The Moon and Sparks approximation applies two separate corrections to the ideal capacitance. The first correction is to determine the effective radius, r_e, by combining the radius r and half of the gap, g, between the sensing element and the guard ring. This is shown in Eq. (1-6). The capacitance with this new radius applied is shown in Eq. (1-7). Since the electric field is not parallel in this region there is an additional correction that is a function of the gap g and the distance between plates d. This correction term χ is presented in Eq. (1-8). The resulting capacitance C_g is presented in Eq. (1-9). All three of these closed-form solutions will be compared to finite element calculations in Chapter 2.

$$r_e = r + \frac{g}{2} \tag{1-6}$$

$$C_0 = \frac{\pi \varepsilon_0 r_e^2}{d} \tag{1-7}$$

$$\chi = -\frac{g^2}{2\pi r_e d} \coth\left(\frac{\pi r_e}{d}\right) \tag{1-8}$$

$$C_g = C_0\left[1 + \chi\right] \tag{1-9}$$

Despite being based upon thin conducting plates, the Moon and Sparks approximation has been recommended by several more recent publications, including Heerens and Vermeulen [6], Lanyi [7], and Hicks and Atherton [8].

Another approximation for capacitance was suggested by Brown and Bullied [9] for the case of plates with finite thickness, *s*, and the inclusion of a guard ring. Brown and Bullied's approximation applies a correction factor that depends upon the width of the space between the sensing area and guard ring, *g*, as shown in Eq. (1-10).

$$\chi = \frac{g\left(1+\dfrac{g}{2r}\right)}{r\left(1+\dfrac{0.22g}{d}\right)} \tag{1-10}$$

For the case of a capacitance gage with a guard ring placed in close proximity to a curved surface, no closed form solution is found in the literature. Finite element modeling has been used for both flat surfaces [10] and for rough and tilted surfaces [11] with good results. Applying these methods to a variety of curved surfaces is the next logical step.

1.1.2 Capacitive sensing circuitry

There are many different electrical circuits that linearize the output of the capacitance gage as a function of the gap distance *d*. The simplest measurement system is to drive the capacitor with a sinusoidal current of the form shown in Eq. (1-11) [12]. The resulting voltage is given by the integral in Eq. (1-12), which is solved in Eq. (1-13). The ratio of voltage to current shown in Eq. (1-14) therefore varies with the inverse of capacitance, and this value is therefore directly proportional to the gap distance *d*.

$$I = I_0 \sin \omega t \tag{1-11}$$

$$V = \frac{1}{C}\int I \cdot dt \tag{1-12}$$

$$V = \left(-\frac{I}{\omega C}\right)\cos \omega t \tag{1-13}$$

$$\frac{V}{I} = \left(-\frac{1}{\omega C}\right)\cos \omega t \tag{1-14}$$

In practice, more complex circuits such as those described by Jones and Richards [13] and Hugill [14] incorporate reference capacitors and other elements to stabilize the output. In addition, short-circuiting of the sensing element is a common scenario, so protection from such overloading is necessary.

1.1.3 Calibration of capacitance displacement gages

The calibration of a capacitance gage must be accomplished using one or more devices that are capable of comparable resolution. A displacement sensing interferometer, for example, is able to measure position to within a few percent of the wavelength of the laser illumination used, typically 10 nm for lasers in the visible spectrum. By using a moving target in combination with the readout from such an interferometer, the output of the capacitance gage can be electronically calibrated to a known source.

Without access to the typically proprietary circuit diagrams of their electronics, the overall linearity of a particular capacitance gage system must be determined by examining the calibration data. Indeed, calibration information from Lion Precision, the manufacturer of the capacitance gages used throughout this study, shows this output to be linear to within 0.2% over the entire operational range of the capacitance probe [15].

Finally, it is important to take note of the active range of the commercial capacitance sensor at various gain settings. Throughout the capacitance simulation and analysis a distinction will be made between absolute distances to surfaces, denoted by d, and a relative displacement, denoted by Δd. The chart in Table 1-2 lists both the distance and displacement values, and the output voltages, for the two gain settings of interest.

Table 1-2. Distance and displacement values for the "fine" and "ultrafine" gain settings of a Lion Precision capacitance gage.

Gain setting	Variable	Minimum	Reference (nom.)	Maximum
Fine	Distance d	0.0762 mm (3.0 minch)	0.1016 mm (4.0 minch)	0.1270 mm (5.0 minch)
	Displacement Δd	-0.0254 mm (-1.0 minch)	0.0000 mm (0.0 minch)	0.0254 mm (1.0 minch)
	Voltage, V	-10 V	0 V	+10 V
Ultrafine	Distance d	0.02032 mm (0.8 minch)	0.02540 mm (1.0 minch)	0.03048 mm (1.2 minch)
	Displacement Δd	-0.00508 mm (-0.2 minch)	0.00000 mm (0.0 minch)	0.00508 mm (0.2 minch)
	Voltage, V	-10 V	0 V	+10 V

1.2 Common Applications of Capacitive Displacement Sensors

1.2.1 Feedback in nanopositioning stages

Capacitance gages excel at applications where the travel displacements are small but the demands of sensitivity (output voltage per unit displacement) are great. One example of such an application is for piezo-driven nanopositioning stages. These stages require closed-loop feedback because their piezo actuators exhibit nonlinear time-dependent phenomena such as hysteresis and creep. Because of their high sensitivity and repeatability, these closed loop piezo-stages are often used as the motion control stages of scanning probe microscopes such as scanning tunneling microscopes (STMs) and atomic force microscopes (AFMs). The sample is typically placed on the moveable nanopositioning stage with the probe fixed above it. The piezo stage is easily controlled by the electronic circuits of the AFM, and the capacitance gage maintains the linearity and precision of the required motion. A photograph of a commercially available, closed-loop nanopositioning stage (Polytec PI) that employs piezo actuators and capacitance displacement sensors is shown in Figure 1-4. This stage can be moved 100 μm in X, Y, and Z directions with nanometer resolution. External electronics collect the signals from the capacitance gages and use this information to provide power to the piezo controllers.
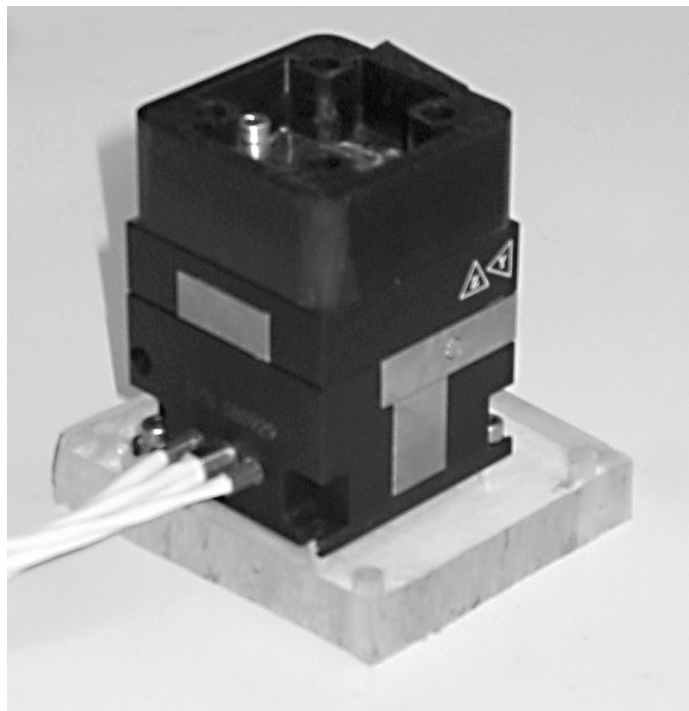
Figure 1-4. A piezo-driven nanopositioning stage.

1.2.2 Spindle metrology

Although capacitance gages are exceptionally accurate in applications involving flat, parallel surfaces, many applications in machine metrology involve rotating axisymmetric artifacts such as a sphere or cylinder. Donaldson reversal, a common method to separate errors due to an imperfect target surface from errors in the axis of rotation, must use as a target a cylindrical or spherical surface. An overhead view of such an application is illustrated in Figure 1-5, which is reproduced from [16].
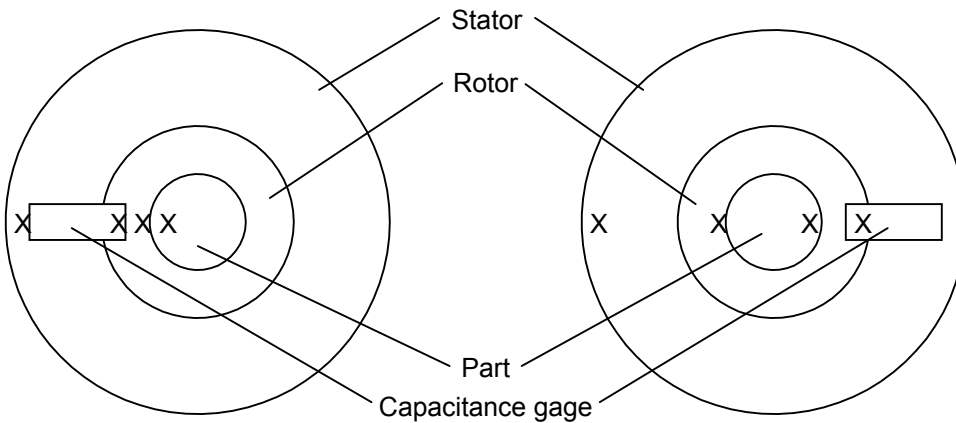
Figure 1-5. Spindle measurement using the Donaldson Reversal technique.

Two measurements are made of a rotating surface, a "normal" and a "reversed" measurement, with both angular and displacement values recorded. Because the reverse placement is 180 degrees out of phase from the normal measurement, the sum of these two measurements represents twice the surface profile, and the difference represents the spindle radial error motion. In equation form from [17], this becomes Eqs. (1-15) to (1-18), where I_1 and I_2 are the forward and reverse measurements, respectively, R is the spindle radial error motion, and B is the surface profile.

$$I_1(\theta) = R(\theta) + B(\theta)$$

(1-15)

$$I_2(\theta) = -R(\theta) + B(\theta)$$

(1-16)

$$R(\theta) = \frac{I_1(\theta) - I_2(\theta)}{2}$$

(1-17)

$$B(\theta) = \frac{I_1(\theta) + I_2(\theta)}{2} \qquad \textbf{(1-18)}$$

The mathematics of the Donaldson reversal technique assume that the sensitivity of the capacitive gage (in V/mm or V/minch) is linear so that the spindle error can be separated from the surface errors. The functions I_1 and I_2 are not measured directly, but are derived from a linear gain G, specifically as shown in Eqs. (1-19) and (1-20).

$$I_1(\theta) = G \cdot V_1(\theta) \qquad \textbf{(1-19)}$$

$$I_2(\theta) = G \cdot V_2(\theta) \qquad \textbf{(1-20)}$$

Plugging these linear functions into the previous equations results in solutions to R and B in terms of G, V_1, and V_2. However this analysis falls apart if we assume that the displacement is not a linear function of V. Assume for a moment that the form of the equation is predominantly linear, with a small quadratic term with coefficient δ. These modified measurements are shown in Eq. (1-21) and Eq. (1-22).

$$I_1(\theta) = G \cdot V_1(\theta) + \delta \cdot V_1^2(\theta) \qquad \textbf{(1-21)}$$

$$I_2(\theta) = G \cdot V_2(\theta) + \delta \cdot V_2^2(\theta) \qquad \textbf{(1-22)}$$

Now the calculations become quite complex and are not easily solved. As will be shown in Chapter 3, in the final analysis both the gain G of the capacitance gage as well as its linearity is compromised when viewing a curved surface.

1.2.3 Reference flat metrology

A reference flat surface can also be measured using a capacitance gage transducer. In particular, a conductive flat can be measured directly, while non-conductive surfaces can be measured indirectly, as described in Section 1.3.1. In either case a linear motion stage is mounted parallel to the reference flat, and the capacitance gage is parallel to the surface. A conductive surface must be grounded to the capacitance gage electronics. The combined error of the reference flat and the linear motion stage must not exceed the active range of the capacitance

11

gage. These two errors are separated using Donaldson reversal, as described by Evans, Hocken, and Estler [18] and also in Section 1.2.2. Unlike the spindle metrology case, as long as the capacitance gage is parallel to the surface, the sensitivity should match the calibrated data.

1.3 Overcoming Limits on the Capacitance Gage Active Range

Like any sensor, capacitance gages are not without their limitations. Generally a capacitance gage is applied only to conductive surfaces. Although non-conductive surfaces can be detected due to differences in relative permeability, the ε_R term from Eq. (1-3), this is an indirect method.

Non-contact methods also suffer when a surface is not perfectly clean. Attempting to measure a machined surface might result in misinformation due to oil or dirt present on the surface. In such cases a contact probe may be a better alternative, since such a probe generally has sufficient force to press against the machined surface.

A third limitation of a capacitance gage is in the overall travel range. Since this is a displacement sensor all points of interest on a surface should be taken with a single measurement. This may prove impossible if the surface has too much variation from ideal or if, as mentioned in Section 1.2.3, the moving stage and the surface to be measured are not parallel. There are workarounds for all three of these limitations.
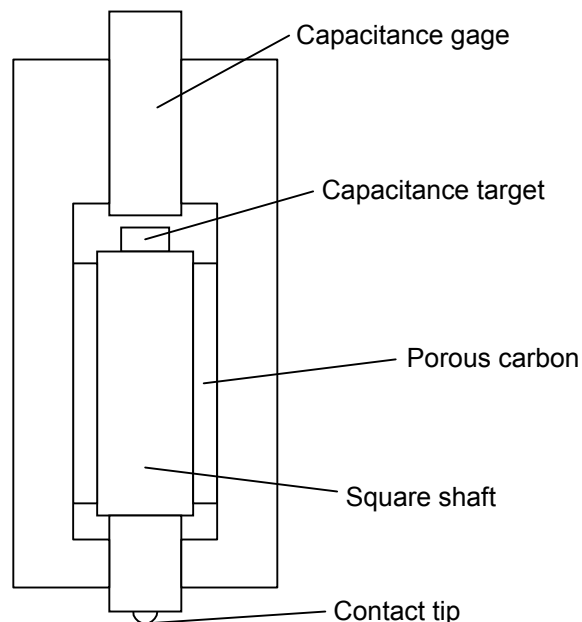
Figure 1-6. Contact probe adapter from Lion Precision.

1.3.1 Adapting for contact sensor arrangement

One solution to both the conductive surface problem as well as the problem of a contaminated surface is to use a capacitance gage in combination with a contact probe. Such a device is available from Lion Precision, their contact probe adapter [19], shown in Figure 1-6. This adapter combines a fixed capacitance gage with a moveable contact probe. The contact probe moves on a small air bearing support, and the displacements are measured using the capacitance gage. Any desired probe tip diameter and material can be accommodated with this arrangement, and the capacitance gage electronics remain unchanged.

1.3.2 Surface tracking

Since capacitance gages have a small active range, applications where more travel is needed require an additional displacement measurement device. A system that combines a large displacement range with similar resolution to the capacitance gage is a laser interferometer. An interferometer uses two pathways, a measurement pathway and a reference pathway, to establish displacement. Light from the laser is divided using a beamsplitter and sent along the two pathways. Once they are recombined the resulting beam intensity will vary as the length of the measurement pathway changes. Ideally, these two pathways both terminate in a retroreflector. The surface conditions required by an interferometer are therefore even more stringent than those required of a capacitance gage.

A measurement scheme previously described [20] uses one sensor to "track" a surface, then uses an interferometer to measure displacement of the tracking component. In this example, an optical head from a compact disc player is used to track a surface with step features. The optical head feedback electronics are designed to produce an optimal spot size for the laser by maintaining a constant distance from the surface. As surface features are encountered, the PZT actuator in the system moves the optical head to compensate. The interferometer measures the movement of the optical head, which corresponds precisely to the surface features. The optical head and measurement setup diagrams from this paper are reproduced in Figure 1-7. Once again, this mode of surface tracking is implemented in the closed-loop system described in Chapter 4.
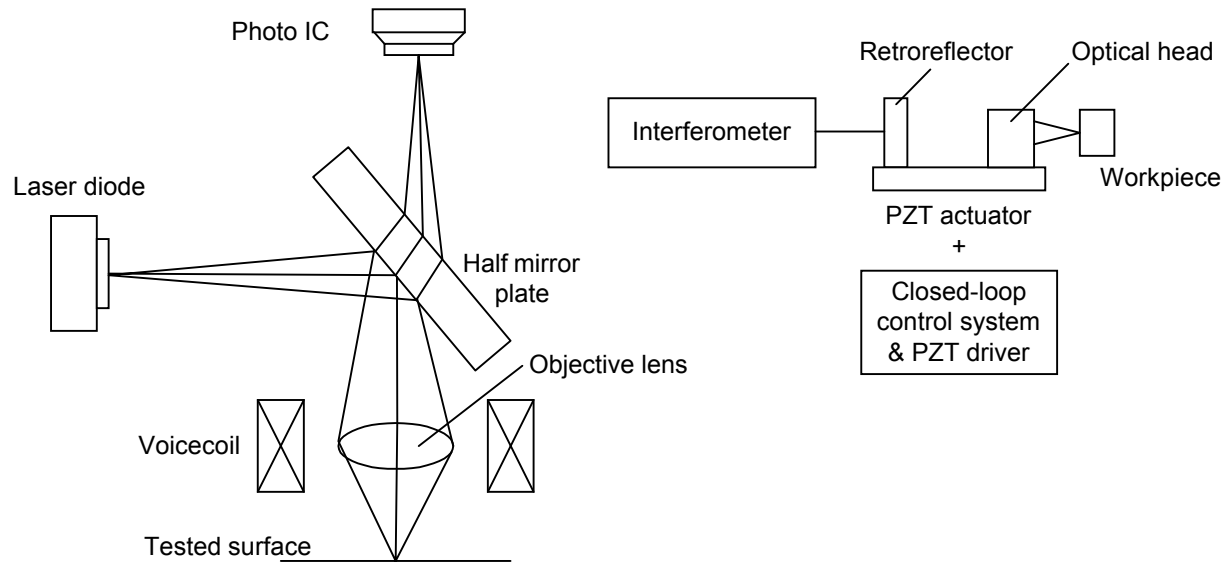
Figure 1-7. Optical head (left) and measurement setup (right) of a surface tracking system.

1.4 A Form Measurement Machine

Designing a subsystem that eliminates one of the primary limitations of a capacitance sensor is not enough to prove its practicality. An application is needed that requires such a subsystem, and a machine must be designed to show how the subsystem is applied.

Large format mirrors for astronomical applications require a precision form over a large area. Future generations of space-based telescopes will likely be dependent on thin "gossamer" optics made from formed and coated polymers. These mirrors, unlike the rigid ones of previous designs, cannot be subjected to the forces of a contact probe without drastically deforming. Non-contact measurement is a necessity.

The travel required to measure such a mirror naturally increases as the size increases. Since these surfaces are not truly spherical even a "perfectly" formed mirror will require some travel of the measurement gage. A subsystem that overcomes this limitation is therefore also necessary for such a machine.

1.5 Conclusions

Capacitance gages are displacement sensors that use the capacitance properties of parallel conductive plates. Although the simplest capacitor configuration is that of two equal-sized parallel plates, in practical applications a third conductor is required to isolate the electric field from outside influences. Closed form approximate solutions exist for several of these geometries, but not for cases of curved target surfaces.

Capacitance gages also suffer from several drawbacks. They are calibrated against a flat surface, therefore they are only accurate when used against such a surface. Unfortunately, some applications such as spindle metrology cannot offer a flat reference surface. The errors in such a measurement must be evaluated so that they can be removed in postprocessing. Capacitance gages are also limited in terms of active sensing range. To overcome this drawback, a capacitance gage can be used to track a surface and its motion followed by a second displacement sensor, such as a laser interferometer. A complete machine design incorporating these components will prove the usefulness of these studies.

2:
Finite Element Analysis of Capacitance Gage Measurements of Spherical Surfaces

2.1 Introduction

Capacitance sensors are used for many non-contact displacement measurement applications. By applying voltage they create an electric field between a central "sensing" element and a grounded, conductive "target" surface. The voltage potential between the two conductors is analogous to the solution of a heat transfer problem between two surfaces whose temperature is fixed. The electric field lines are the gradient of the potential, analogous to the direction of heat flow.

For a flat target the electric field lines are uniform and parallel across most of the sensing area. For a spherical target surface the solution is more complex, and a closed form equation has not been found. To determine the capacitance of this system, a finite element model of a commercially available capacitance sensor and a spherical target is modeled in the Ansys finite element software. Capacitance values are first calculated for various gap distances from a flat surface, then these results are compared to similar capacitance values derived from spherical surfaces.

2.2 Electric Field Analysis Formulation

Most mechanical engineers are familiar with finite element analysis (FEA) packages for use with stress/strain calculations or heat transfer modeling. The software package Ansys, in addition to these options, can also be applied to solve electric or magnetic field problems. As with traditional mechanical problems, a complex electric field problem that cannot be calculated analytically can be solved using a sufficiently refined mesh [21].

As is the case with a heat transfer finite element problem, the electric field solution takes the form of a scalar potential. The formulation for a conduction heat transfer problem is given in

Eq. (2-1), from [22], where q^B is the heat generation rate per unit volume, k_x, k_y, and k_z are thermal conductivities, and θ is the temperature.

$$\frac{\partial}{\partial x}\left(k_x \frac{\partial \theta}{\partial x}\right) + \frac{\partial}{\partial y}\left(k_y \frac{\partial \theta}{\partial y}\right) + \frac{\partial}{\partial z}\left(k_z \frac{\partial \theta}{\partial z}\right) = -q^B \qquad \textbf{(2-1)}$$

Boundary conditions applied to heat transfer problems are either a known temperature on a surface or a known heat flux. If there is no heat generation, then the right hand side of Eq. (2-1) is zero.

Changing the variables of Eq. (2-1) to those generally applied to electrostatic problems, the resulting differential equation is shown in Eq. (2-2). Here q^B represents the presence of charges in the electric field or "charge density," the three ε values are the electric permittivity values of the material, and ϕ is the field potential in volts.

$$\frac{\partial}{\partial x}\left(\varepsilon_x \frac{\partial \phi}{\partial x}\right) + \frac{\partial}{\partial y}\left(\varepsilon_y \frac{\partial \phi}{\partial y}\right) + \frac{\partial}{\partial z}\left(\varepsilon_z \frac{\partial \phi}{\partial z}\right) = -q^B \qquad \textbf{(2-2)}$$

The two possible boundary conditions in an electrostatic problem are either to prescribe the charge density on a boundary, analogous to a fixed heat flux on a boundary in a conduction problem, or to prescribe the field potential (voltage) on a surface, analogous to surfaces of constant temperature.

To describe the effect of charges in an electric field problem (the q^B term) consider an insulator that has been electrically charged by removing or adding electrons. When this insulator is placed in close proximity to other conductors or insulators, electrons will "sense" the charges on the insulator and be either drawn or repulsed by them depending on their sign. The force felt by a single electron is the product of the field potential ϕ and the charge of a single electron, measured in Coulombs. The electric field lines represent the direction and magnitude of the total electrostatic force anywhere in the geometry of the problem. Returning to the conduction heat transfer analogy, electric field potential is analogous to lines of constant temperature, while electric field lines are analogous to the direction of heat flow.

Electric permittivity values (ε) represent a property of an insulator where charges are rearranged in the insulator to counteract the presence of charges on nearby materials. Because an insulator will develop a positive charge when placed in close proximity to a negatively charged

conductor and vice-versa, the electric permittivity of an insulator is always greater than that of vacuum. For this reason electric permittivity is typically broken into two values, the dimensioned constant value ε_0, representing vacuum, and a dimensionless multiplier denoted by ε_R, representing the relative increase in permittivity as a property of the material in the gap. For air the ε_R term is typically 1.0008, varying slightly with temperature and humidity. The electric permittivity is analogous to the conduction coefficient k in a heat transfer problem, since a larger k results in higher heat flux, just as an increase in ε results in higher electric fields within the gap.

For a material with an isotropic electric permittivity, the ε values can be moved to the right hand side of the equation. The differential equation now takes the form of Poisson's Equation, shown in Eq. (2-3).

$$\frac{\partial^2 \phi}{\partial x^2} + \frac{\partial^2 \phi}{\partial y^2} + \frac{\partial^2 \phi}{\partial z^2} = \frac{-q^B}{\varepsilon_0 \varepsilon_R} \tag{2-3}$$

The final step to convert this equation to our usable form is to consider the cylindrical symmetry of the problem at hand. The differential operator is put into cylindrical coordinates (r, θ, and z), but by the definition of an axisymmetric problem, there is to be no dependence on the variable θ. The resulting differential equation is shown in Eq. (2-4).

$$\frac{\partial^2 \phi}{\partial r^2} + \frac{1}{r}\frac{\partial \phi}{\partial r} + \frac{\partial^2 \phi}{\partial z^2} = \frac{-q^B}{\varepsilon_0 \varepsilon_R} \tag{2-4}$$

In the case when no free charges are present within the insulated areas of the capacitor, the q^B term on the right side of the equation goes to zero and the form of Eq. (2-5) is Laplace.

$$\frac{\partial^2 \phi}{\partial r^2} + \frac{1}{r}\frac{\partial \phi}{\partial r} + \frac{\partial^2 \phi}{\partial z^2} = 0 \tag{2-5}$$

A detailed analysis of possible solutions to this form of the Laplace Equation is given in [23] based on certain simplified boundary conditions. Unfortunately, the combined boundary conditions of a cylinder and a sphere are not straightforward, and therefore a finite element solution must be pursued.

2.3 Electrostatic Analyses in Ansys

The complete Ansys code used in these simulations is listed in Appendix B, however, an overview of the commands used is useful as well. Of particular interest are the commands that are unique to an electrostatic analysis.

The method used in Ansys to build these models is to begin with keypoints, then add lines, then areas. Because the model is axisymmetric each 2D area in the model actually represents a 3D volume. After the initial header commands to enter the preprocessor, some values are defined for the geometry of the problem, as shown. Values not initially listed in metric units are converted to metric in a subsequent step. The electrostatic constant ε_0 or EMUNIT is also defined below.

```
finish
/clear                   ! used to erase and start over analysis
/title, Axisymmetric Capacitor, h-Method
/prep7
! Defining the geometry of
! parallel plate capacitor in Ansys.
! Set units to mm, microfarads
emunit,epzro,8.854e-9   !epsilon in uF per mm
! Define Variables
pthick=0.05      ! Thickness of each cap plate
bplater=10       ! Base plate radius in mm
uplater=10       ! Upper plate radius
gap=0.05         ! gap between plates at center
rsph=20          ! radius of surrounding sphere
```

Because the finite element analysis is to be completed several times with different keypoint locations, the geometry of the problem was erased and rebuilt for each analysis. In the code below, *G* is the number of iterations for the loop, *I* is the counter, and *C* is an array that will store capacitance values for each plate spacing, as well as the distance between plates for later reference.

```
! Set the number of loops for the calculation
G=1                    ! number of different gaps to use*************
*dim,C,table,G,2,1   ! dimension the capacitance array
! *******************************************************
! Begin Loop Here
*do,I,1,G
/prep7
gap=gapinit+gapinc*(I-1)
tp=gap+dep
!
! Next 3 lines erase all elements to start over geometry
asel,all
aclear,all
adele,all,,,1
!
! Define keypoints of cap gauge and ref surface
k,1,0,tp
k,2,innerbr,tp
k,3,halfpt,tp
k,4,innerpr,tp
```

From these keypoints, lines are created using appropriate size commands, and areas are defined. Element type 121 is to be used to mesh all of the areas except the edges of the model. This quadratic element can be used for a number of different types of analysis including electrostatic, and it is set for an axisymmetric application. For the material property (MP) command two materials are needed, one for the air gap and one for the plastic that is part of the capacitance gage. Since conductors contain no electric field, the conductors will not need to be meshed. The relative permeability (ε_R) of air is set to 1 and the relative permeability of the plastic is set to the dimensionless value 3.8 per the manufacturer's specifications in the code below.

```
et,1,plane121,,,1,,,,      ! area elements for efield
mp,perx,1,1                ! efield relative permeability
mat,1                      ! using material number 1 (air)
mat,2                      ! defining type 2
mp,perx,2,3.8              ! setting permeability material 2 (plastic)
```

The outer boundary of the model must also be supplied with a boundary condition. To avoid using a large number of elements to mesh the surrounding space, an infinite element type (110) is used for the last row of elements of the model. This quadratic element type can also be used in an axisymmetric problem. In the following code, these elements are applied to certain areas and the "infinite" boundary condition for the outer lines is also set.

```
et,2,infin110,1,0,1        ! infinite boundary elements, axisymmetric
mshkey,2
asel,s,area,,9,9           ! first infinite area
asel,a,area,,18,18         ! second infinite area
amesh,all                  ! mesh infinite sections
lsel,s,,,9,9               ! upper edge
lsel,a,,,28,28             ! right edge
lsel,a,,,38,38             ! right edge
sfl,all,inf                ! set these lines to infinity
```

The next step is to group lines representing a common boundary condition together using the CM command. This is necessary for some of the capacitance calculations. It is helpful for a common boundary to use consecutive line numbers as shown here, so that a single selection command can choose not only the lines but also the associated nodes. The assignment of a particular voltage using the d command is necessary for two-conductor analyses.

```
lsel,s,,,39,40,,1          ! selecting center conductor
d,all,volt,V1              ! apply V1 volts to center conductor
cm,cond1,node              ! Define 1st conductor for cmatrix analysis
lsel,s,,,41,44,,1          ! select ground ring
d,all,volt,V1              ! set voltage ground ring same as center
cm,cond2,node

lsel,s,,,45,47,,1          ! select outer shield
d,all,volt,0               ! set voltage of shield to ground
cm,cond3,node
```

```
lsel,s,,,15,23,,1          ! select lower sphere or plate
d,all,volt,V0              ! set voltage to V0
cm,cond4,node
```

The capacitance values are calculated in one of two ways. For a simple, two-conductor problem the capacitance is calculated by first summing the energy stored in the elements (equivalent to strain energy in a traditional mechanics analysis) to *W*. Then the capacitance of the system is given by Eq. (2-6). For the preliminary analysis, voltages V_1 and V_0 were applied to the conductors and the capacitance value calculated within the Ansys script.

$$C = \frac{2W}{\left(V_1 - V_0\right)^2} \tag{2-6}$$

```
/solution                  ! running solver
solve
finish
!
/post1
etable,sene,sene           ! calculating capacitance
ssum
*get,W,ssum,,item,sene
C=(W*2)/((V1-V0)**2)
*status,C
finish
```

For three or more conductors a special routine in Ansys called CMATRIX must be run. This is discussed in detail in Section 2.6. Once the capacitance is calculated it can be stored in a file or printed in an output window. The loop is then repeated as necessary. The two models discussed in the following sections should help in understanding the Ansys routines.
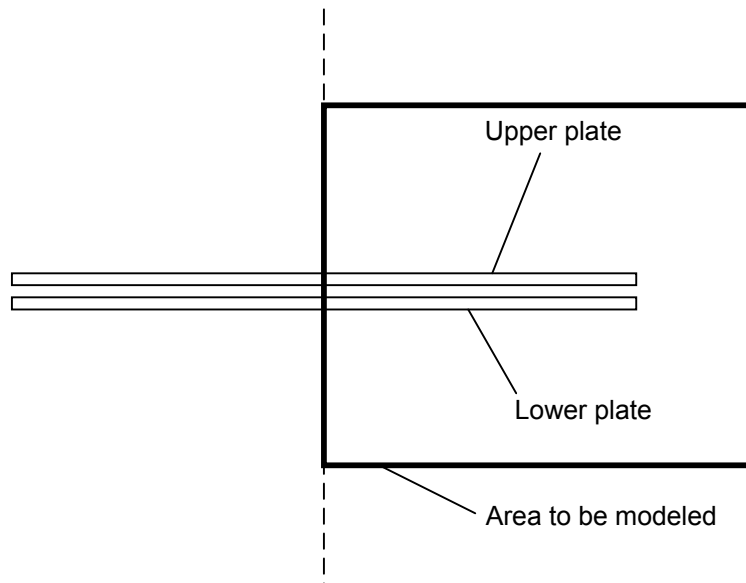
Figure 2-1. Full geometry of parallel-plate problem with area to be modeled.
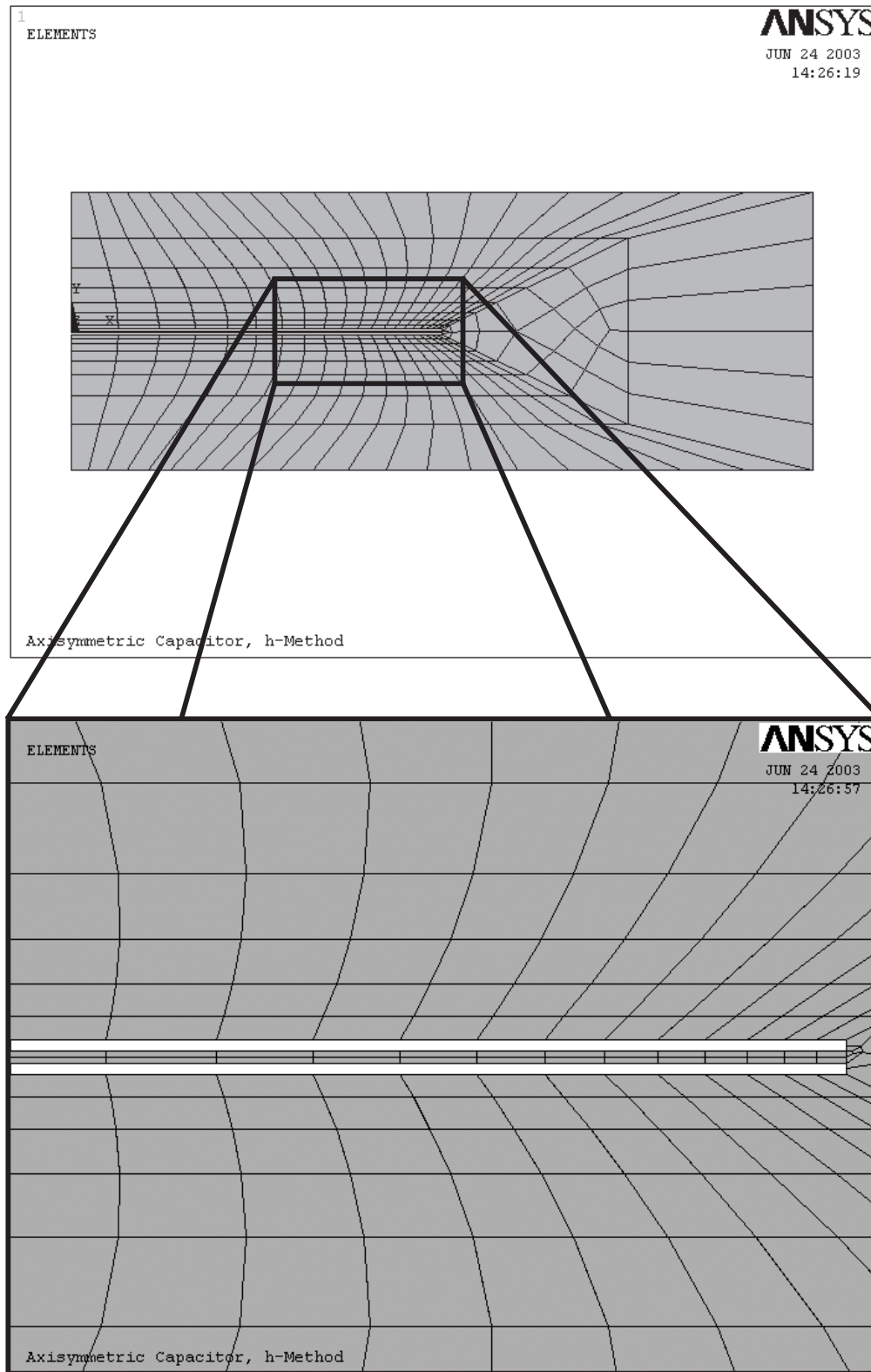
Figure 2-2. Mesh for preliminary finite element model, including detail.

2.4 Parallel Plate Finite Element Model

As a test case for comparison of the finite element model to closed-form solutions, a simplified model of a parallel plate capacitor is built in Ansys. This model consists of two circular parallel plates of thickness 0.05 mm and radius 10 mm, separated by a gap of 0.05 mm. The complete code defining the geometry of this problem appears in Appendix B. This problem is set up with axisymmetric geometry, meaning that only a radial cross section is actually modeled, as shown in Figure 2-1. The left edge of all images from Ansys represents the center of the model and all elements have a three-dimensional volume. With the exception of the leftmost column all elements are actually topologically similar to a toroid (with flattened sides). The mesh is shown in Figure 2-2.

The detailed portion of Figure 2-2 shows that the conductive areas of the model (the white rectangles in this perspective) are not meshed. This is the case in electrostatic modeling for the simple reason that the electric field inside conductors is always zero. This follows from the definition that a conductor; namely, that electrons are free to flow throughout a conductor unimpeded. If an electric field were present within a conductor, charged electrons would feel the resulting force and would rearrange themselves to cancel out the electric field. Conductive surfaces are therefore part of the boundary of the finite element problem.

Of the two boundary conditions mentioned in Section 2.2, the condition applied to conductive surfaces is always that of a fixed potential (voltage). The three surfaces of each plate are therefore assigned a fixed voltage, with different voltages for the upper and lower plates. This is necessary to calculate capacitance (*C*), as energy must first be stored within the mesh before *C* can be calculated.

To prove the validity of the parallel plate finite element model, the result of the capacitance calculation is to be compared against the first two closed form solutions described in Section 1.1.1. Graphically, it is expected that the field potential will be uniformly distributed between the plates as parallel lines and that the electric field vectors are of uniform magnitude between the plates and perpendicular to the conductive surface. The electric field solution is always perpendicular to the surface of a conductor, again by the definition of a conductor. If the electric field vectors at the surface of a conductor have any component along that surface, charges will redistribute themselves to ensure that the field vectors are normal.

From the closed form solution in Eq. (1-3), we set d = 0.05 mm and r = 10 mm. The resulting value for the capacitance C is 55.63 pF. The second closed-form solution, listed in Eq. (1-5), includes fringing and should therefore be more accurate for this arrangement. From Table 1-1, the value of the function f for s = d = 0.05 is 1.39. The closed form calculation using Eq. (1-5) results in the value C = 56.66 pF. These two solutions are the standard by which the Ansys solutions are to be compared.

One axisymmetric solution from Ansys used only element 121 throughout the model. As discussed in Section 2.3, a boundary condition must be applied along the outer edge of elements, in this case setting the potential of these three lines at zero volts. With these conditions and approximately 400 elements, the results of the Ansys calculation are a respectable 57.7 pF. Increasing the number of elements to over 9,000 results in an improvement of the FEA value to 56.79 pF.

One additional improvement is then made to the Ansys model to ensure good agreement with the theoretical values. The outer boundary of the model is not actually at "ground" potential, but instead should be isolated in space from all other conductors. A better model of the system gives the outer elements the property of "infinity," where no electric field lines extend to the outer boundaries of the model (in this axisymmetric model the upper, lower, and right sides). By adding a single row of element 110 to these three sides a result of C = 56.49 pF (an error of 0.3%) is achieved with a mere 394 elements. Details of the potentials and the electric field vectors are shown in Figure 2-3 and Figure 2-4, respectively.

All of the lessons learned while improving this simple model can be applied to the model of the actual capacitance gage geometry, where a closed form solution is not readily available.

2.5 Finite Element Model of Capacitance Sensor

As with the parallel plate capacitance calculation described in Section 2.4, the complete model of the commercially available capacitance gage will be axisymmetric. A drawing of the cross section of the capacitance gage is shown in Figure 2-5, with the area to be modeled highlighted. Per the requirements of the Ansys software package, the left side of the model is the axis of symmetry. Also as in the parallel plate model, this model will be built by defining first keypoints, then lines, then areas. These areas of course represent volumes when the model is rotated about its axis. The author has found that for moderately involved geometries it is better to

build the geometry from the ground up, rather than attempting to define geometric areas first and then subtracting or adding other areas as needed. By building the geometry "by hand," changes made throughout the refinement of the model did not produce unexpected changes in line or area numbering. Such changes are the bane of a script that depends on the sequential numbering of areas to define material properties and boundary conditions.

The keypoints and lines of the capacitance gage and a flat target are shown in Figure 2-6. Lines are created to separate areas that represent conductors and insulators in the capacitance gage, and vertical lines are dropped through the air gap to the lower surface. These additional lines allow every area in the model to be a quadrilateral, making it possible to fill each area entirely with quadrilateral elements.
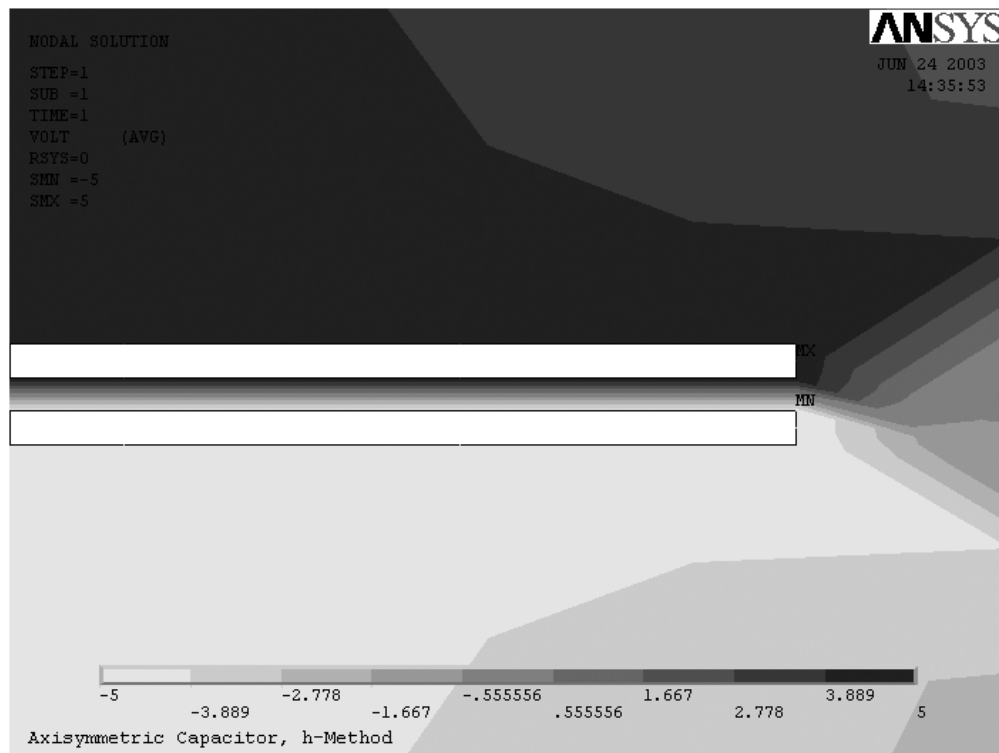
Figure 2-3. Detail of equipotential lines indicating the FEA solution to the parallel plate capacitor problem.
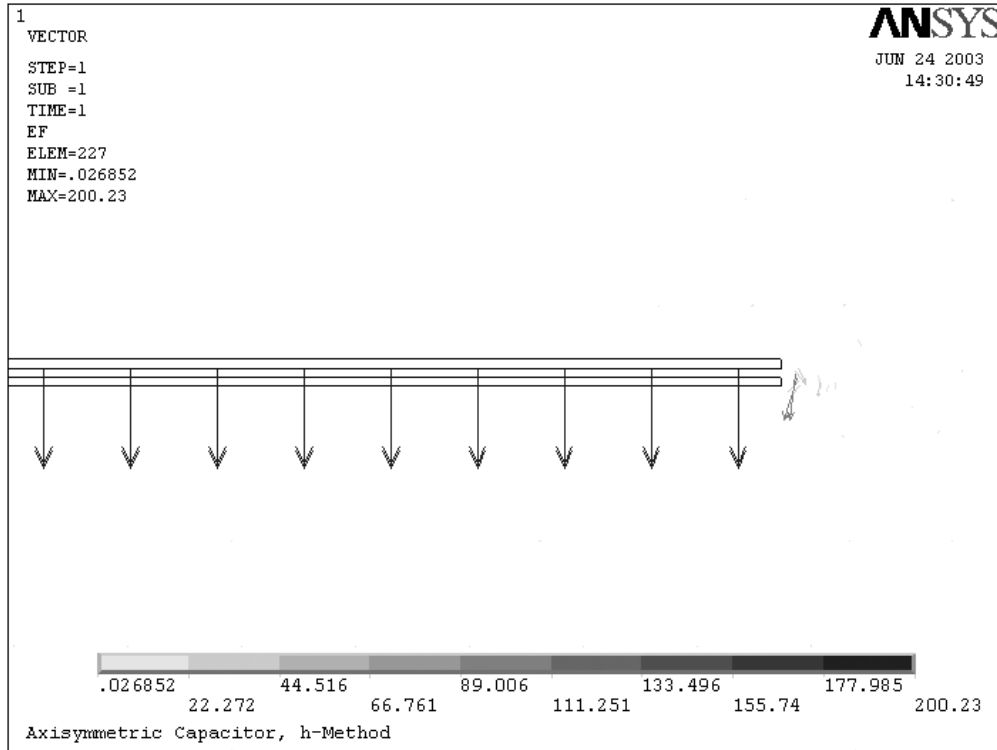
Figure 2-4. Electric field vector solution. The field strength is indicated by the length of each vector.
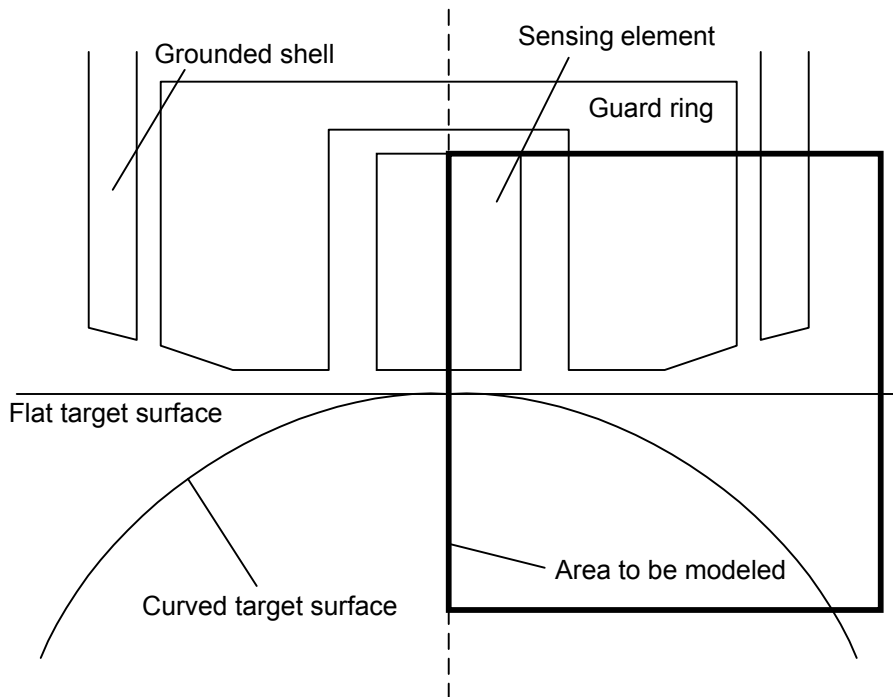
Figure 2-5. Cross-section of capacitance gage showing area to be modeled in Ansys.
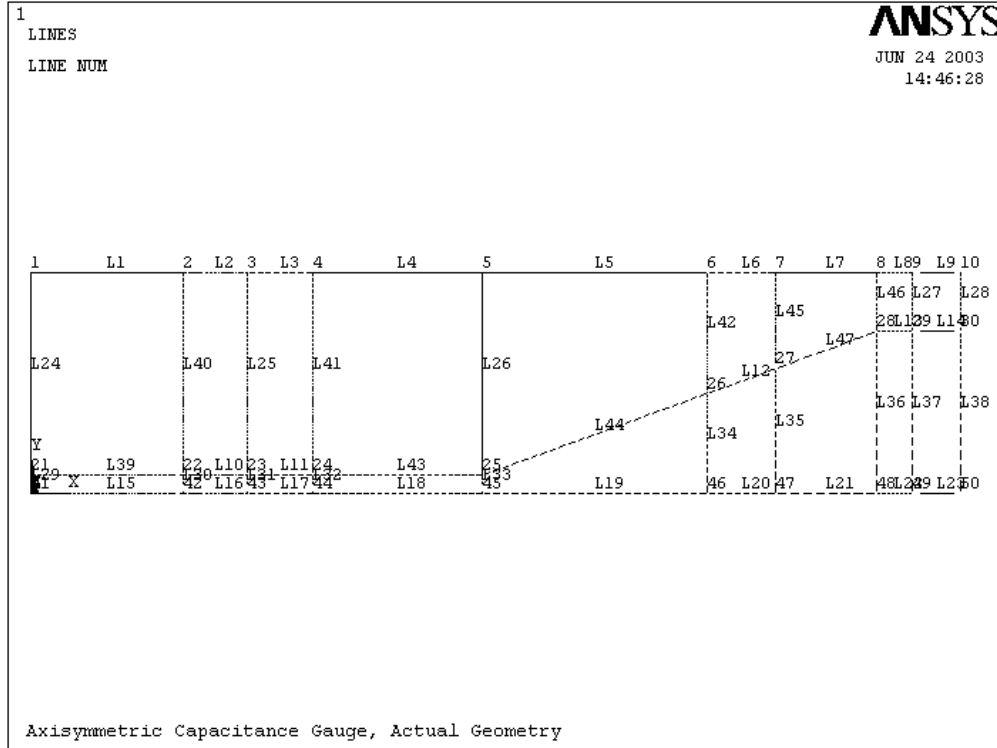
Figure 2-6. Lines defining electric field problem geometry in Ansys.
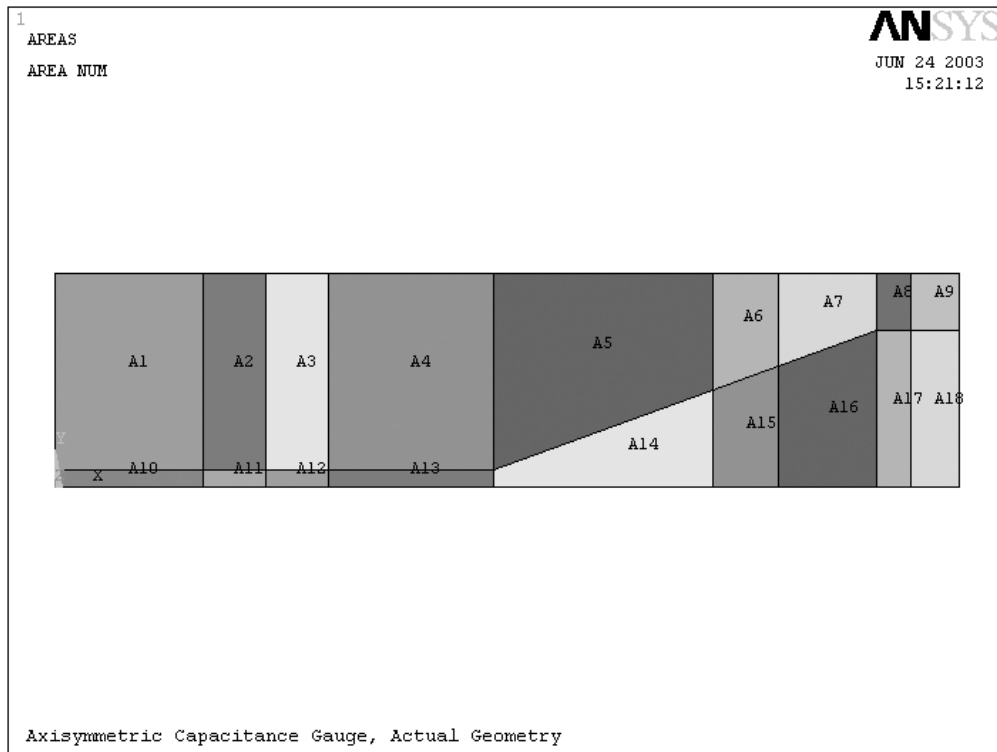
Figure 2-7. Areas defined in the 2D Ansys model for a flat, parallel target.

The lower lines in Figure 2-6 represent the conductive target, in this case a flat surface, and the upper row of rectangles and quadrilaterals represents the geometry of the capacitance gage. The numbered areas defined from these keypoints and lines are shown in Figure 2-7 for the case of a flat target surface, and in Figure 2-8 for a curved surface. Area 1 represents the central conductor, the sensing element of the capacitance gage. Because this represents a conductor it does not need to be meshed into elements and therefore it is not a requirement that it be defined as an area.

Areas 2 and 3 both represent the dielectric insulator that fills the gap between the sensing element and the guard ring. Two areas are defined only because the author originally speculated that such separation may have been needed to accurately calculate capacitance. This turned out not to be the case. These areas are both meshed with axisymmetric element 121.

Areas 4 and 5 represent the guard ring, a conductor held at approximately the same voltage as the sensing element but whose capacitance does not contribute to the output of the gage. This is divided into two quadrilateral areas since the face of the guard ring changes geometry at this point, and it was desirable to have quadrilateral sections throughout the model. Area 6 is another dielectric section meshed with element 121, surrounded by Area 7, the outer (grounded) shielding of the probe. Area 8 is the final air gap meshed with element 121, while area 9 is composed of one column of the specialized "infinite" element 110 that indicates mathematically the absence of any conductors external to those being modeled.

The second row of areas represents the air gap between the capacitance gage and the target surface. Once again, these are divided into multiple areas so that they can be meshed with quadrilateral elements. Areas 10 through 17 are meshed with element 121, while area 18, like area 9 above it is meshed with the "infinite" element 110.

The mesh of quadrilateral elements applied to all non-conductive areas is shown in Figure 2-9 for the case of the flat target, and Figure 2-10 for the case of the curved surface. Both the model for the flat target and the model for the curved target in their final form have exactly the same number of lines, areas, and elements. It is only the shapes of the elements that become deformed as the curvature of the target is changed. This allows the Ansys code to be nearly identical for the two cases.
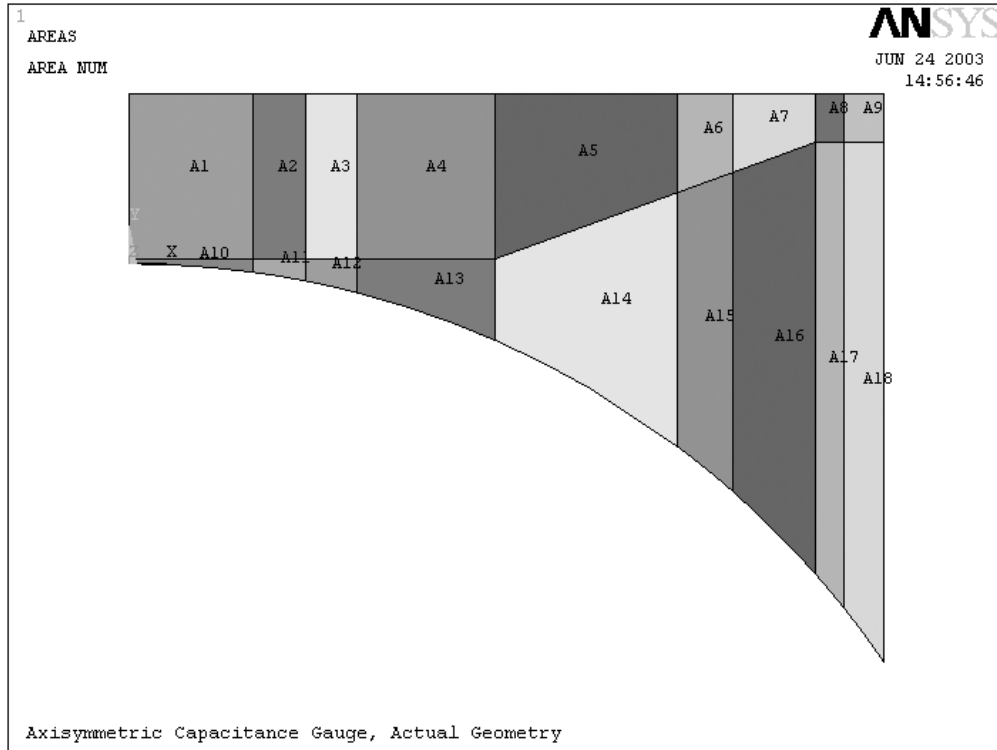
Figure 2-8. Areas defined in the 2D Ansys model for a curved (spherical) target.
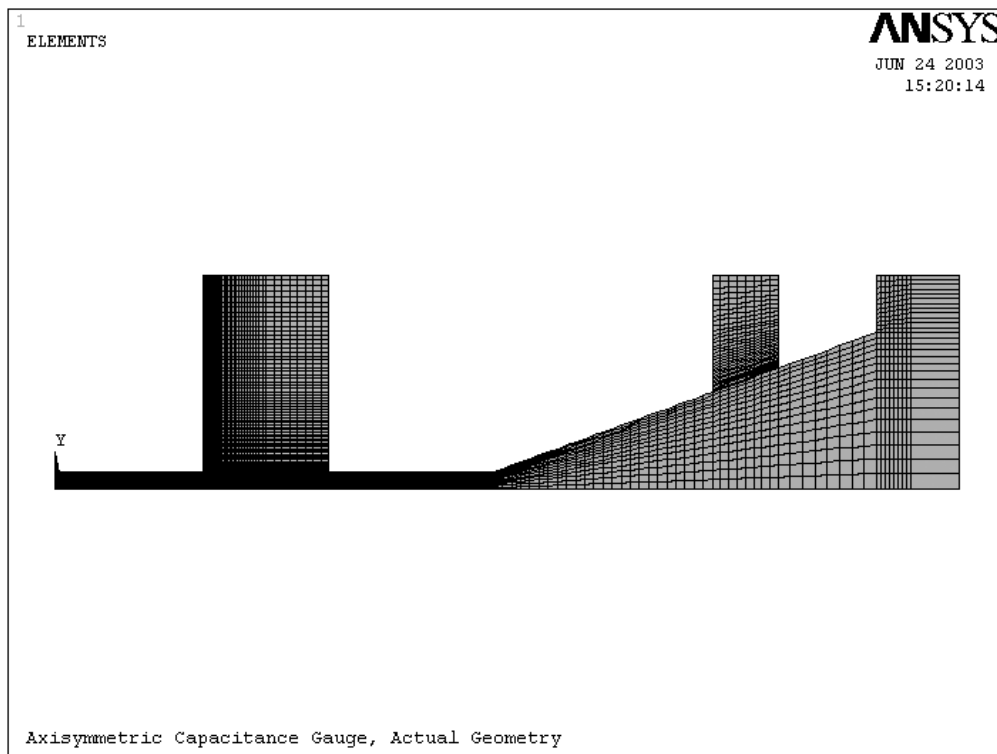
Figure 2-9. Complete meshed areas of Ansys model for a flat target. Note that only non-conductive areas are meshed (dielectric and air regions).
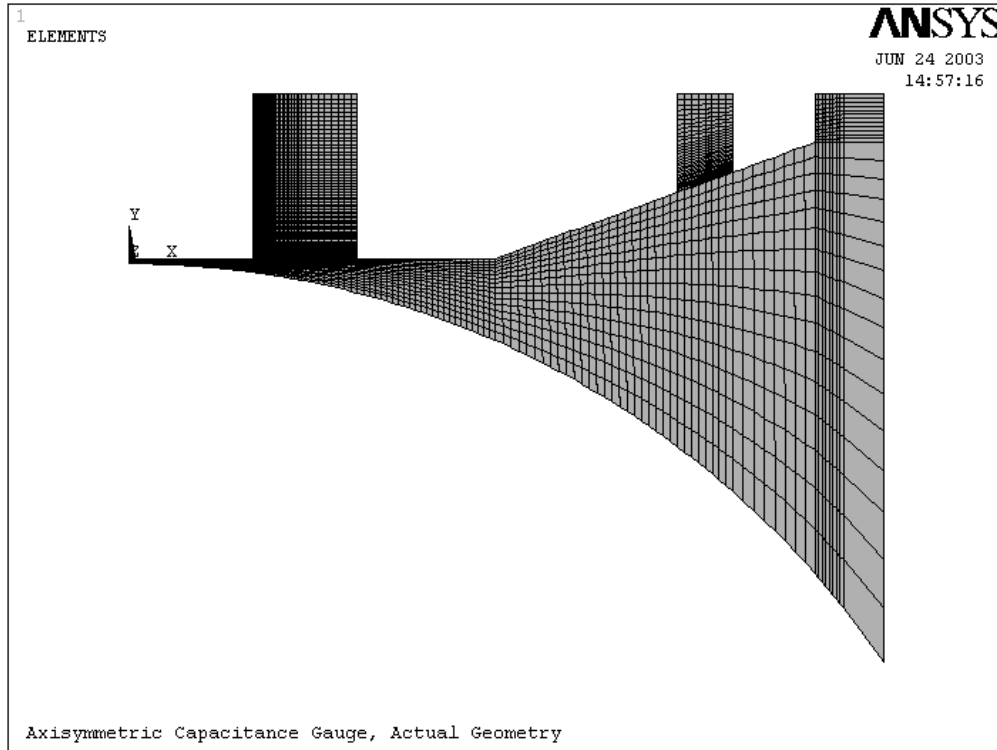
Figure 2-10. Complete meshed areas of Ansys model for spherical target.
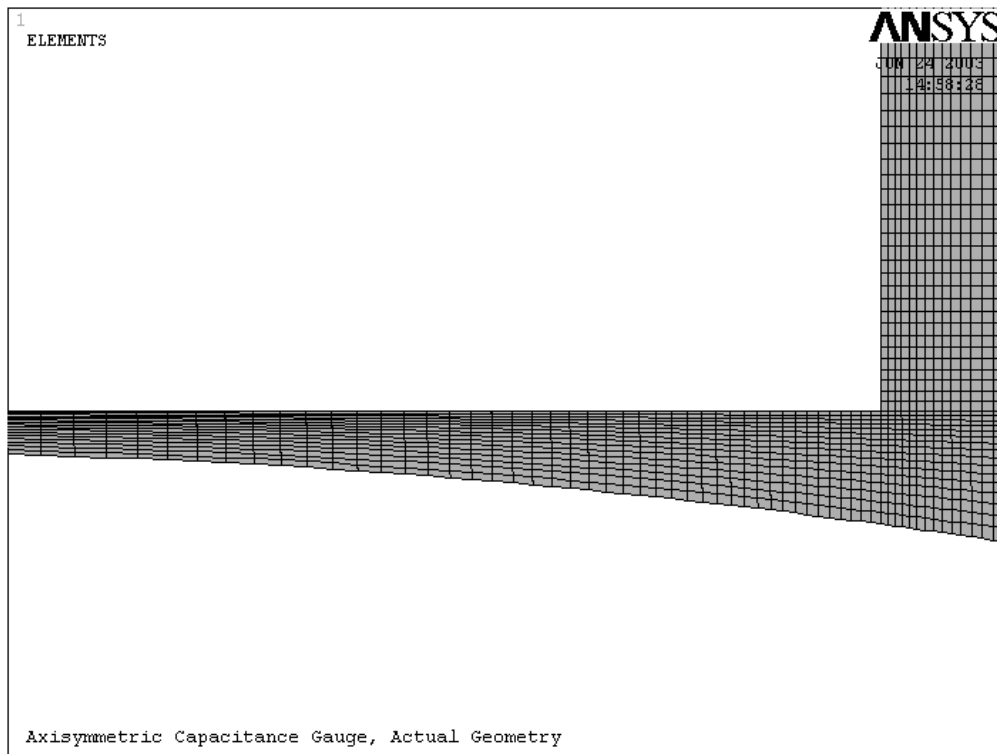
Figure 2-11. Detail of quadrilateral elements surrounding central conductor.

The mesh for this model is composed of quadrilateral elements of varying sizes, rectangles wherever possible, with the finest mesh placed at the areas where the electric field has the most drastic changes. From prior analyses the areas that show the highest gradient are at the corners of conductors, where the normal to the conductive surface changes suddenly. For this reason the mesh surrounding the corner of the central conductor, shown in detail in Figure 2-11, is some three times finer than other areas. Also note that the number of rows between the capacitance gage and the target surface is constant, even though in the case of the curved target the gap widens considerably. This is deemed acceptable since the most critical areas of the model occur in the air and dielectric material surrounding the central, sensing conductor. The exact mesh and even the geometry of the probe outside the guard ring have little impact with regard to the capacitance value of interest.

Once the mesh is complete the boundary conditions are applied to each of the conductors. Lines 39 and 40, which are the boundary of area 1, are grouped together as conductor 1. If the problem at hand was to calculate the electric field, these lines would be assigned a fixed voltage (potential). However, since the goal of this analysis is to determine capacitance, these voltages will be applied automatically to the numbered conductors as described in Section 2.6. In a similar fashion, lines 41-44 are grouped together to form conductor 2, lines 45-47 form conductor 3, and lines 15-23 form conductor 4.

2.6 Graphical Ansys Solution

Although the goal of this analysis is to produce comparative capacitance values for flat vs. curved target surfaces, it is illustrative to also apply a typical set of voltages to the conductors and perform a single analysis showing the electric field and the equipotential lines (lines of constant voltage).

2.6.1 Electric field lines

To calculate a finite element solution to the electric field, voltages must first be applied to all four conductors. As is the case with the actual capacitance gage, both the central conductor and the guard ring are set to the same potential (+5 V). The outer shell of the probe and the target surface are both set to ground (0 V). Figure 2-12 shows the resulting vector solution of the electric field for each element. Care must be taken in interpreting this display: the density of arrows does not represent the magnitude of the electric field, only the density of nodes in the

model (one arrow per node). It is actually the length and gray-level of the vector that represents the magnitude of the electric field. From left to right, as the gap increases, there is a corresponding decrease in electric field strength. Notice also the changing direction of the field vectors at the sharp corner of the central conductor. This is the "fringe effect" mentioned previously, where electric fields change direction suddenly. For this reason a finer mesh was used when modeling this area of the air gap.

Also notice the direction of the vectors in the gap between the central conductor and the guard ring. As you move horizontally from the central conductor to the right, initially the field lines point away from the central conductor and toward the target surface (downward and to the right). Later, the field lines switch, and now point downward and to the left. These latter lines originate from the guard ring and thus represent electric field caused by the interaction of the guard ring and the target surface. Since only the electric field from the central conductor is included when the capacitance is measured, the point where the electric field ceases to emanate from the central conductor has been termed by this author the "crossover point." This is after all the purpose of the guard ring: to limit the fringing or extension of the electric field as much as possible beyond the boundary of the central conductor. The closer the field lines are to parallel, the closer the system will be to perfectly linear.

2.6.2 Equipotentials

A second useful graphical presentation of a single Ansys solution shows the location of equipotential lines within the insulating spaces. One such display appears in Figure 2-13. It is important to note that, since the electric field lines are the gradient of the potential function, the equipotential lines are perpendicular to the electric field vectors shown in Figure 2-12. As can be seen in Figure 2-13, the line spacing is nearly parallel between the central conductor and the target surface, with a "hill" located between the central conductor and the guard ring. For a perfectly linear system this artifact would not exist, however the goal of the guard ring is to minimize this curvature. Looking at the potential lines at the outer edge of the guard ring, all lines curve upward to pass between the guard ring and the outer conductor of the capacitance gage, which is grounded. Without the guard ring, this effect would occur on the outer surface of the central conductor, where it would severely affect the linearity of the gage. A voltage of +9 V is applied to the central conductor and the guard ring in Figure 2-13.
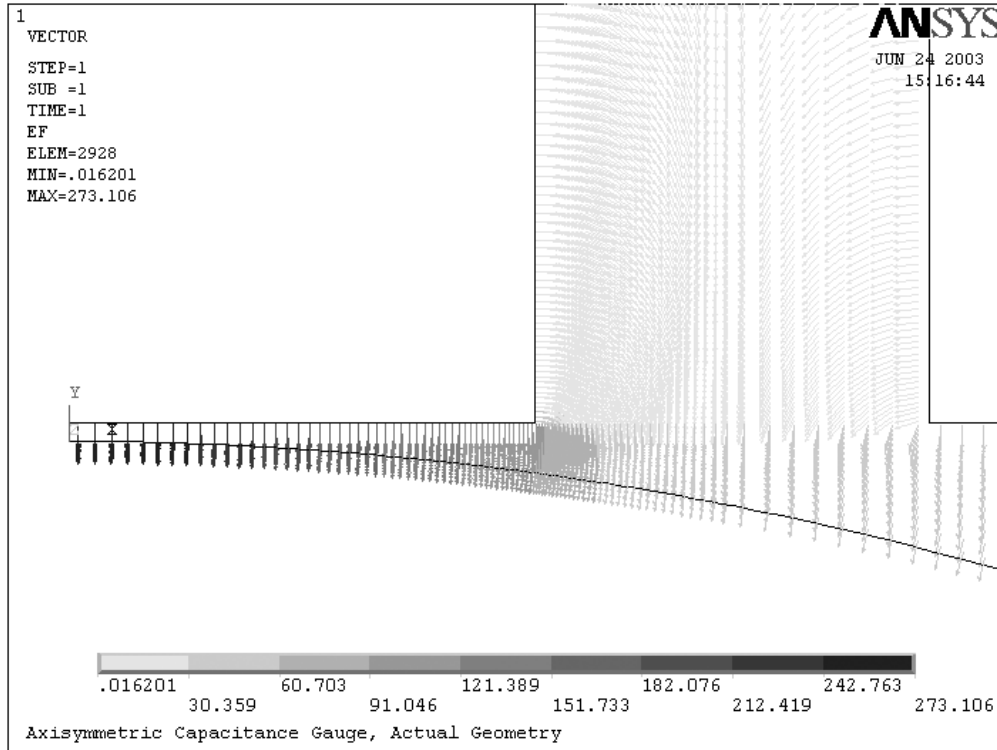
Figure 2-12. Electric field solution from Ansys.
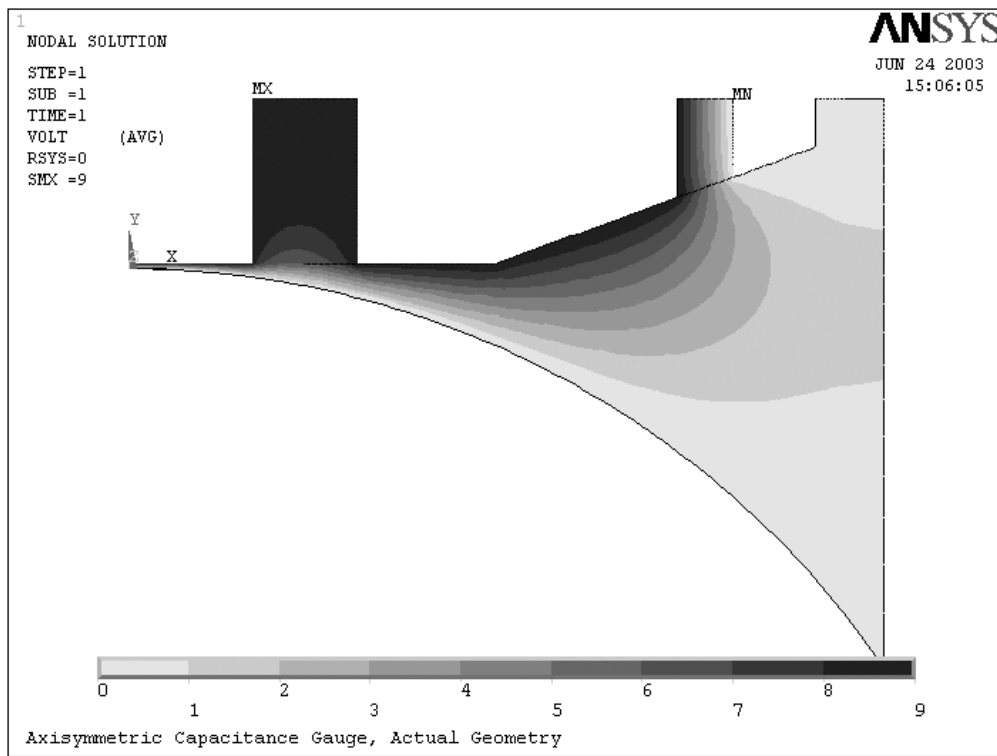
Figure 2-13. Equipotential lines of Ansys solution.

2.7 Capacitance Calculations

Once the geometry, the material properties, the boundary conditions, and the mesh have all been defined, there are two methods to calculating the capacitance values. In the preliminary analysis only two conductors existed in the model, so when a voltage difference is applied to the plates the resulting energy is all due to the two plates alone.

When more than two conductors are involved, the calculations to determine the capacitance become much more convoluted, and involve multiple finite element solutions to the same geometry. Fortunately, some of this linear algebra is automated by Ansys.

2.7.1 Self-lumped and mutual-lumped capacitances

For a model such as the commercial capacitance gage described in Section 2.5, where four conductors are involved, several different capacitances must be determined. In this model the conductors are numbered as shown in Figure 2-14. Each conductor has its own self-lumped capacitance, as well as mutual lumped capacitance between each of the other conductors. The mutual lumped values, C_{12}, C_{13}, C_{14}, etc., in Figure 2-14, are the values that represent what an external circuit is able to measure, and so must be determined for each geometric configuration.
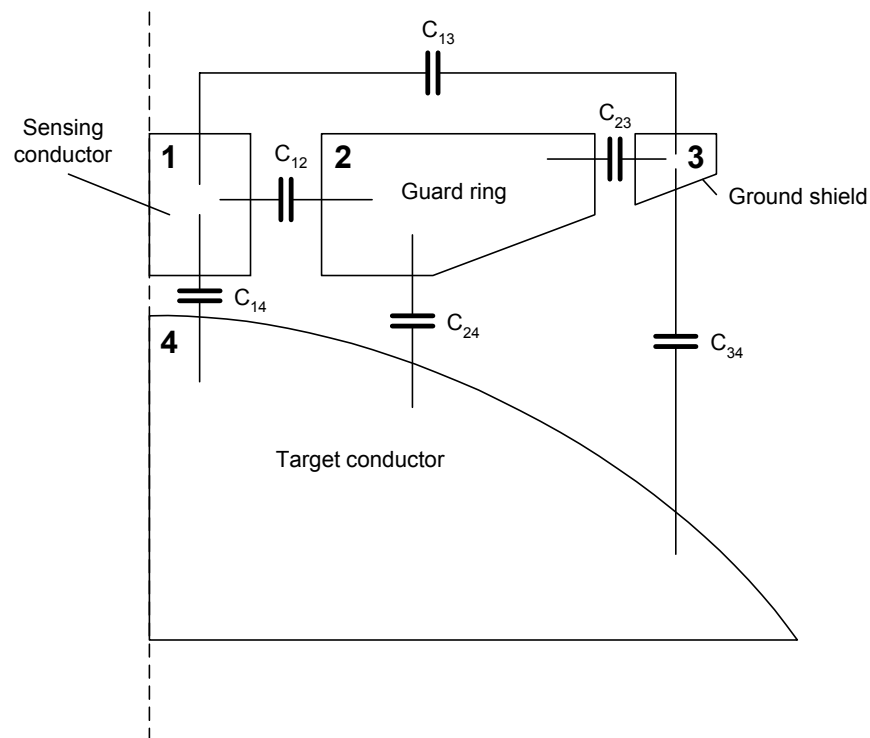
Figure 2-14. Numbering applied to the different conductors within Ansys. Conductor 4 is also considered ground.

The technique for determining the mutual lumped capacitance values when multiple conductors are present necessitates multiple analyses, but the steps to calculate these values have been automated by the Ansys software. For each geometrical configuration, several sets of voltages are applied to the conductors and the electric field determined. The resulting energy W stored throughout the model is calculated. For a four-conductor problem such as this the energy is given by Eq. (2-7).

$$W = \tfrac{1}{2} D_{11}V_1^2 + \tfrac{1}{2} D_{22}V_2^2 + \tfrac{1}{2} D_{33}V_3^2 + \tfrac{1}{2} D_{44}V_4^2 + \qquad\qquad (2\text{-}7)$$
$$D_{12}V_1V_2 + D_{13}V_1V_3 + D_{14}V_1V_4 + D_{23}V_2V_3 + D_{24}V_2V_4 + D_{34}V_3V_4$$

These D values are not the lumped capacitance values that we are seeking but are rather the ground capacitance values, their capacitance relative to an external ground conductor. The ground capacitance is the capability of any conductor isolated in space to hold a charge. Values in Eq. (2-7) such as D_{11} represent the self-ground capacitance of electrode 1, while D_{12} represents the mutual ground capacitance between conductors 1 and 2. The first step in calculating the lumped values C is to calculate the values of the ground capacitances D.

The Ansys macro CMATRIX automates much of this task. As mentioned in Section 2.3, within the Ansys script the four conductors are defined by their nodes and given the names "cond1," "cond2," etc. The macro CMATRIX first determines the D_{11}, D_{22}, etc. values by applying voltages to the conductors, one at a time, setting all other voltages to zero. Applying only V_1, for example, results in Eq. (2-7) reducing to Eq. (2-8). Since V_1 is known and W can be determined from the finite element solution, this equation can be solved for D_{11}. In a similar manner, voltages are applied to determine the D_{12}, D_{13}, etc. values from Eq. (2-7).

$$W = \tfrac{1}{2} D_{11}V_1^2 \qquad\qquad (2\text{-}8)$$

The total charge Q on a single conductor is given by the product of the self-ground capacitance D and the voltage V. For the case of more than one conductor, the charge Q on each conductor is determined from all four voltages and the appropriate ground capacitance values, as given in Eqs. (2-9) through (2-12).

$$Q_1 = D_{11}V_1 + D_{12}V_2 + D_{13}V_3 + D_{14}V_4 \qquad\qquad (2\text{-}9)$$

$$Q_2 = D_{12}V_1 + D_{22}V_2 + D_{23}V_3 + D_{24}V_4 \tag{2-10}$$

$$Q_3 = D_{13}V_1 + D_{23}V_2 + D_{33}V_3 + D_{34}V_4 \tag{2-11}$$

$$Q_4 = D_{14}V_1 + D_{24}V_2 + D_{34}V_3 + D_{44}V_4 \tag{2-12}$$

The lumped capacitance values C, which are the desired goal of the analysis, are calculated from these charges Q. These lumped capacitance values take into account the differences in the voltages across conductors, rather than the absolute voltage, and are obtained from Eqs. (2-13) through (2-16).

$$Q_1 = C_{11}V_1 + C_{12}(V_1 - V_2) + C_{13}(V_1 - V_3) + C_{14}(V_1 - V_4) \tag{2-13}$$

$$Q_2 = C_{22}V_2 + C_{12}(V_2 - V_1) + C_{23}(V_2 - V_3) + C_{24}(V_2 - V_4) \tag{2-14}$$

$$Q_3 = C_{33}V_3 + C_{13}(V_3 - V_1) + C_{23}(V_3 - V_2) + C_{34}(V_3 - V_4) \tag{2-15}$$
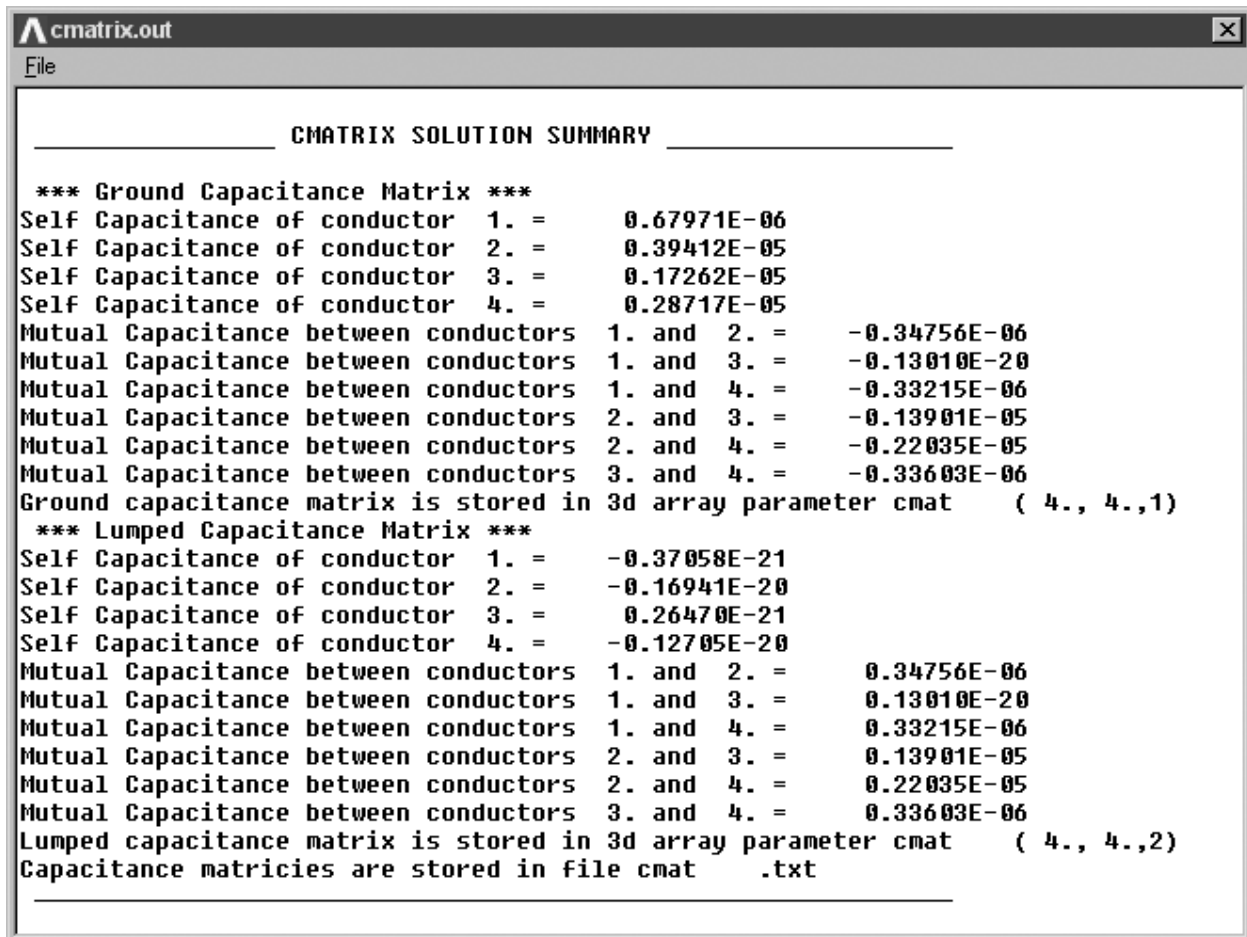
$$Q_4 = C_{44}V_4 + C_{14}(V_4 - V_1) + C_{24}(V_4 - V_2) + C_{34}(V_4 - V_3) \tag{2-16}$$

A slightly different configuration of voltage values is needed to complete the calculation of the lumped capacitance values C. For example, setting $V_1 = V_2 = V_3 = V_4$ and having already determined all of the values of D, the four Q values and the self lumped capacitance values C_{11}, C_{22}, C_{33}, and C_{44} can be determined. The six mutual lumped values C_{12}, C_{13}, etc. are determined by appropriate combinations of voltages as shown in Table 2-1.

Table 2-1. Order of determining lumped capacitances from FEA values.

Step	Variable solved	Equation	V_1	V_2	V_3	V_4
1.	D_{11}, Q_1	(2-7), (2-9)	1.0	0.0	0.0	0.0
2.	D_{22}, Q_2	(2-7), (2-10)	0.0	1.0	0.0	0.0
3.	D_{33}, Q_3	(2-7), (2-11)	0.0	0.0	1.0	0.0
4.	D_{44}, Q_4	(2-7), (2-12)	0.0	0.0	0.0	1.0
5.	$C_{11}, C_{22}, C_{33}, C_{44}$	(2-13) to (2-16)	1.0	1.0	1.0	1.0
6.	C_{14}, C_{24}, C_{34}	(2-13) to (2-15)	1.0	1.0	1.0	0.0
7.	C_{13}, C_{23}	(2-13) to (2-14)	1.0	1.0	0.0	1.0
8.	C_{12}	(2-13)	1.0	0.0	1.0	1.0

An example of the output from a single run of the CMATRIX macro is shown in Figure 2-15. Both the ground capacitance and the lumped capacitance values are presented. Because conductor 4 is also defined as ground (i.e. there is no ground external to this problem) the mutual ground capacitance values and the mutual lumped capacitance values only differ by a sign convention. Out of all these results, the capacitance pertinent to this study is the mutual lumped capacitance between conductor 1 (the sensing element) and conductor 4 (the target surface). This is the variable C_{14} from Figure 2-14.

```
Λ cmatrix.out                                                              ⊠
 File

 _____ CMATRIX SOLUTION SUMMARY _____

  *** Ground Capacitance Matrix ***
 Self Capacitance of conductor  1. =      0.67971E-06
 Self Capacitance of conductor  2. =      0.39412E-05
 Self Capacitance of conductor  3. =      0.17262E-05
 Self Capacitance of conductor  4. =      0.28717E-05
 Mutual Capacitance between conductors  1. and  2. =    -0.34756E-06
 Mutual Capacitance between conductors  1. and  3. =    -0.13010E-20
 Mutual Capacitance between conductors  1. and  4. =    -0.33215E-06
 Mutual Capacitance between conductors  2. and  3. =    -0.13901E-05
 Mutual Capacitance between conductors  2. and  4. =    -0.22035E-05
 Mutual Capacitance between conductors  3. and  4. =    -0.33603E-06
 Ground capacitance matrix is stored in 3d array parameter cmat    ( 4., 4.,1)
  *** Lumped Capacitance Matrix ***
 Self Capacitance of conductor  1. =     -0.37058E-21
 Self Capacitance of conductor  2. =     -0.16941E-20
 Self Capacitance of conductor  3. =      0.26470E-21
 Self Capacitance of conductor  4. =     -0.12705E-20
 Mutual Capacitance between conductors  1. and  2. =     0.34756E-06
 Mutual Capacitance between conductors  1. and  3. =     0.13010E-20
 Mutual Capacitance between conductors  1. and  4. =     0.33215E-06
 Mutual Capacitance between conductors  2. and  3. =     0.13901E-05
 Mutual Capacitance between conductors  2. and  4. =     0.22035E-05
 Mutual Capacitance between conductors  3. and  4. =     0.33603E-06
 Lumped capacitance matrix is stored in 3d array parameter cmat    ( 4., 4.,2)
 Capacitance matricies are stored in file cmat    .txt
```

Figure 2-15. Output of CMATRIX command for flat plate geometry.

2.7.2 Capacitance for flat target surface

For the purposes of this study it is not enough to determine a single capacitance value. For a given target surface the capacitance value C_{14} must be calculated several times to produce a table of capacitance values as a function of the distance between conductors d and the target shape. These values are to be compared against theoretical values and against each other.

The first target to be analyzed is a flat plane. Fifteen *d* values are used and for each spacing the geometry is built from scratch. The CMATRIX macro determines the capacitance between conductors 1 and 4. As mentioned in Section 2.3, because the CMATRIX values are overwritten each time the distance *d* is changed, it is necessary to pull out the capacitance value of interest and store it in a separate array. The array is output as a text file once the analysis of all geometries is complete. These data files are named to reflect the geometry of the target surface and the gain setting that the simulation is emulating. The capacitance results of the flat plane control study are shown in the third column of Table 2-2.

Table 2-2. Output of capacitance calculations for flat surface, as compared with theoretical values from Eq. (1-3), Eq. (1-7), and Eq. (1-8).

d, mm	*d*, minch	*C*, flat surf., pF	*C* from (1-3), pF	C_0 from (1-7), pF	*C* from (1-8), pF
0.066040	2.6	0.4817117	0.309526	0.6287	
0.071120	2.8	0.4521186	0.287417	0.5838	0.0155
0.076200	3.0	0.4261263	0.268255	0.5449	0.0498
0.081280	3.2	0.4030960	0.251489	0.5108	0.0757
0.086360	3.4	0.3825340	0.236696	0.4808	0.0954
0.091440	3.6	0.3640525	0.223546	0.4541	0.1103
0.096520	3.8	0.3473424	0.211781	0.4302	0.1216
0.101600	4.0	0.3321538	0.201191	0.4087	0.1302
0.106680	4.2	0.3182827	0.191611	0.3892	0.1366
0.111760	4.4	0.3055605	0.182901	0.3715	0.1414
0.116840	4.6	0.2938468	0.174949	0.3554	0.1448
0.121920	4.8	0.2830235	0.167659	0.3405	0.1472
0.127000	5.0	0.2729906	0.160953	0.3269	0.1487
0.132080	5.2	0.2636625	0.154763	0.3144	0.1496
0.137160	5.4	0.2549662	0.149031	0.3027	0.1499

The distance values *d* in Table 2-2 include the active range of the cap gage at its "fine" gain setting, namely 0.0762 to 0.127 mm (3.0 to 5.0 minch) at a gain of 394 Volts/mm (10 Volts/minch). Two additional distance values are included at the beginning and at the end of the data to ensure that the active range is modeled properly; this will be discussed further in Chapter 3.

2.7.3 Comparison of flat surface values to theory

Now that capacitance values have been calculated for a flat target surface from the finite element approximation, it is important to compare this to the two models discussed in Section 1.1.1. Columns 4, 5, and 6 of Table 2-2 present the capacitance values for the same geometry based on Eq. (1-3), Eq. (1-7), and Eq. (1-8). Equation (1-3), which neglects any fringing effects due to the thickness of the sensing conductor, produces values much smaller than those

determined by Ansys. Equation (1-7), which increases the sensing area to include half of the distance to the guard ring, overestimates the capacitance. Equation (1-8), which is designed to take into account the full nature of the guard ring geometry, should provide the best estimate. It is obvious from the data that this is not the case, and in fact this is the worst estimate of the three. This is due to the fact that the assumptions made during the development of the equation are not valid for this geometry. Clearly, all of these closed-loop approximations suffer from various limitations.

One reason that Eq. (1-3) is such an underestimate of the actual capacitance was described in Section 2.6.1. Graphically it was shown that the electric field lines extend beyond the diameter of the central conductor, partway to the guard ring. The "effective radius," or the location of the crossover point, can be back-calculated using the capacitance numbers as determined by Ansys. Returning to the simplest capacitance equation and plugging in the actual radius of the central conductor, $r = 0.8585$ mm (33.8 minch), the capacitance value C for a distance d of 0.0254 mm (1.0 minch) is calculated using Eq. (2-17) to be 0.8048 pF.

$$C = \frac{\varepsilon_0 A}{d} = \frac{\varepsilon_0 \pi r^2}{d} \qquad \textbf{(2-17)}$$

The capacitance as calculated by Ansys (1.0828 pF) is greater than this and that is to be expected, since the cylindrical walls of the central conductor are contributing to the total capacitance and cannot be neglected. Using an FEA-determined capacitance value C, Eq. (2-17) can be solved for the effective radius r_{eff}, as shown in Eq. (2-18).

$$r_{eff} = \sqrt{\frac{Cd}{\varepsilon_0 \pi}} \qquad \textbf{(2-18)}$$

Table 2-3 lists additional theoretical capacitances and the values as calculated by Ansys. As the gap distance increases, the effective radius also increases, indicating a spreading of the electric field. In all cases the effective radius is larger than the radius of the central conductor, 0.8585 mm (33.8 minch), and smaller than the inner radius of the ground ring, 1.585 mm (62.4 minch). The ground ring, therefore, is able to effectively contain the electric field well within its boundaries as expected, although less so as the gap increases.

Table 2-3. Effective values of the central conductor radius as a function of the distance *d*.

d, mm	*d*, minch	C_{theor}, pF	C_{calc}, pF	r_{eff}, mm	r_{eff}, minch
0.01829	0.7200	1.1177	1.4342	0.971055	38.2305
0.02540	1.0000	0.8048	1.0828	0.994367	39.1483
0.03251	1.2800	0.6287	0.8783	1.013209	39.8901
0.06604	2.6000	0.3095	0.4817	1.069416	42.1030
0.07620	3.0000	0.2683	0.4261	1.080409	42.5358
0.10160	4.0000	0.2012	0.3322	1.101545	43.3679
0.12700	5.0000	0.1610	0.2730	1.116447	43.9546
0.13716	5.4000	0.1490	0.2550	1.121344	44.1474

2.7.4 Capacitance for spherical targets

Once the Ansys capacitance values for a flat surface have been validated, the effects of a spherical target on the capacitance can be investigated. For some data sets the same distance values *d* were used to calculate the capacitance value C_{14}. One such set of results for a 12.7 mm (0.5 inch) target is shown in Table 2-4.

Table 2-4. Output of capacitance calculations for 12.7 mm (0.5 inch) diameter target, distance values identical to that of flat surface.

d, mm	d, minch	C, half inch., pF
0.066040	2.6	0.2659735
0.071120	2.8	0.2528921
0.076200	3.0	0.2411320
0.081280	3.2	0.2304947
0.086360	3.4	0.2208208
0.091440	3.6	0.2119804
0.096520	3.8	0.2038665
0.101600	4.0	0.1963899
0.106680	4.2	0.1894761
0.111760	4.4	0.1830617
0.116840	4.6	0.1770929
0.121920	4.8	0.1715234
0.127000	5.0	0.1663133
0.132080	5.2	0.1614278
0.137160	5.4	0.1568368

By comparing the capacitance values from Table 2-2 and Table 2-4 it is apparent that the curvature dramatically affects the capacitance value. Additionally, the same distance values applied to flat and curved surfaces produce capacitance values that, in this example, almost fail to overlap. The capacitance value in Table 2-4 resulting from a spacing of 0.06604 mm (2.6 minch) roughly corresponds to the flat spacing of 0.13208 mm (5.2 minch). If an actual experiment were performed using the capacitance gage electronics, the results would be as

follows: when the capacitance gage is positioned at any distance larger than 0.06604 mm (2.6 minch), the output will be off-scale! The active range of the sensor will be found in a displacement range of approximately 0.05 mm (2 minch) with a *maximum* distance d of 0.06604 mm (2.6 minch).

By running preliminary values of capacitance at each diameter sphere and comparing the results to the flat plane values of Table 2-2, an appropriate starting point is determined for each diameter sphere. These values are shown in Table 2-5 for both of the gain settings that were eventually used in the calculations.

Table 2-5. Starting and ending points for each target sphere and gain setting in minch.

Sphere diameter	Start, 394V/mm gain	End, 394V/mm gain	Start, 1969V/mm gain	End, 1969V/mm gain
6.350 mm (0.250 in)	0.0102 mm (0.4 minch)	0.0813 mm (3.2 minch)	0.0005 mm (0.02 minch)	0.0147 mm (0.58 minch)
9.525 mm (0.375 in)	0.0229 mm (0.9 minch)	0.0940 mm (3.7 minch)	0.0005 mm (0.02 minch)	0.0147 mm (0.58 minch)
12.70 mm (0.500 in)	0.0330 mm (1.3 minch)	0.1041 mm (4.1 minch)	0.0005 mm (0.02 minch)	0.0147 mm (0.58 minch)
15.88 mm (0.625 in)	0.0381 mm (1.5 minch)	0.1092 mm (4.3 minch)	0.0020 mm (0.08 minch)	0.0132 mm (0.52 minch)
19.05 mm (0.750 in)	0.0457 mm (1.8 minch)	0.1168 mm (4.6 minch)	0.0025 mm (0.10 minch)	0.0137 mm (0.54 minch)
22.23 mm (0.875 in)	0.0432 mm (1.7 minch)	0.1143 mm (4.5 minch)	0.0046 mm (0.18 minch)	0.0157 mm (0.62 minch)
25.40 mm (1.000 in)	0.0457 mm (1.8 minch)	0.1168 mm (4.6 minch)	0.0061 mm (0.24 minch)	0.0173 mm (0.68 minch)

With these final distances the capacitance values for all 7 sphere diameters can be calculated for the two different gain settings. Although these gain values do not enter into any of the calculations in Ansys, it is necessary to recalculate the values because the nominal distance (distance that produces a 0 V output from the capacitance gage electronics) is different for the different gain settings. As described previously the gain setting of 394 V/mm (10 V/minch) has a total active range of 0.0762 to 0.1270 mm (3.0 to 5.0 minch), which corresponds to a nominal offset of 0.1016 mm (4.0 minch). The highest gain setting of 1969 V/mm (50 V/minch) has a nominal offset of 0.0254 mm (1.0 minch) with a total range of 0.02032 to 0.03048 mm (0.8 to 1.2 minch). The complete capacitance results are shown in Table 2-6 and Table 2-7. These are the values that will be analyzed in great detail in the next chapter.

2.8 Conclusions

Finite element modeling software such as Ansys can be used to solve electrostatic problems. In the simplified case of two parallel plates, the results closely match available closed form solutions. When a complete model is built of a commercially available capacitance gage and the target surface is a flat plane, once again the results fall in the expected range.

Capacitance values are next calculated for cases where the capacitance gage is placed in close proximity to spherical surfaces. The data shows that the more extreme curvature deviates a greater amount from the flat (reference) data. Furthermore, many of these data points fall outside the active range of the capacitance gage, so new active ranges are defined for each diameter sphere. The spherical data is analyzed in detail in Chapter 3.

Table 2-6. Capacitance values calculated for the gain setting 394 V/mm.

Dia (mm)	6.35	9.53	12.70	15.88	19.05	22.23	25.40	flat
Dia (in)	0.250	0.375	0.500	0.625	0.750	0.875	1.000	flat
d_{start} (mm)	0.01016	0.02286	0.03302	0.0381	0.04572	0.04318	0.04572	0.06604
d_{start} (minch)	0.4	0.9	1.3	1.5	1.8	1.7	1.8	2.6
d_{inc} (mm)	0.0051	0.0051	0.0051	0.0051	0.0051	0.0051	0.0051	0.0051
d_{inc} (minch)	0.2	0.2	0.2	0.2	0.2	0.2	0.2	0.2
C (pF)	0.5260	0.4937	0.4723	0.4752	0.4515	0.4891	0.4878	0.4817
	0.4595	0.4507	0.4373	0.4415	0.4223	0.4551	0.4545	0.4521
	0.4136	0.4161	0.4079	0.4129	0.3970	0.4260	0.4259	0.4261
	0.3789	0.3875	0.3828	0.3882	0.3749	0.4007	0.4010	0.4031
	0.3513	0.3633	0.3610	0.3666	0.3553	0.3786	0.3791	0.3825
	0.3285	0.3425	0.3418	0.3475	0.3379	0.3589	0.3596	0.3641
	0.3093	0.3242	0.3248	0.3305	0.3222	0.3413	0.3422	0.3473
	0.2926	0.3081	0.3096	0.3152	0.3080	0.3256	0.3264	0.3322
	0.2781	0.2938	0.2959	0.3014	0.2951	0.3113	0.3122	0.3183
	0.2652	0.2809	0.2835	0.2888	0.2833	0.2982	0.2992	0.3056
	0.2537	0.2692	0.2721	0.2774	0.2725	0.2863	0.2874	0.2938
	0.2433	0.2586	0.2618	0.2669	0.2626	0.2754	0.2765	0.2830
	0.2339	0.2488	0.2522	0.2572	0.2533	0.2653	0.2664	0.2730
	0.2253	0.2399	0.2434	0.2482	0.2448	0.2560	0.2571	0.2637
	0.2174	0.2316	0.2352	0.2399	0.2368	0.2474	0.2484	0.2550

Table 2-7. Capacitance values calculated for the gain setting 1969 V/mm.

Dia (mm)	9.53	12.70	15.88	19.05	22.23	25.40	flat
Dia (inch)	0.375	0.500	0.625	0.750	0.875	1.000	flat
d_{start} (mm)	0.000508	0.000508	0.002032	0.002540	0.004572	0.006096	0.018288
d_{start} (minch)	0.02	0.02	0.08	0.10	0.18	0.24	0.72
d_{inc} (mm)	0.001016	0.001016	0.001016	0.001016	0.001016	0.001016	0.001016
d_{inc} (minch)	0.04	0.04	0.04	0.04	0.04	0.04	0.04
C (pF)	1.4507	1.8216	1.5661	1.6609	1.5009	1.4432	1.4342
	1.1623	1.4384	1.3946	1.4934	1.3909	1.3519	1.3691
	1.0296	1.2627	1.2749	1.3708	1.3014	1.2746	1.3101
	0.9430	1.1485	1.1836	1.2749	1.2263	1.2080	1.2565
	0.8790	1.0644	1.1102	1.1964	1.1619	1.1498	1.2075
	0.8283	0.9980	1.0491	1.1305	1.1059	1.0982	1.1625
	0.7865	0.9435	0.9969	1.0739	1.0565	1.0521	1.1211
	0.7511	0.8973	0.9516	1.0244	1.0125	1.0106	1.0828
	0.7203	0.8574	0.9117	0.9807	0.9728	0.9729	1.0473
	0.6932	0.8224	0.8761	0.9416	0.9369	0.9385	1.0143
	0.6691	0.7913	0.8440	0.9064	0.9041	0.9069	0.9835
	0.6473	0.7633	0.8149	0.8743	0.8741	0.8778	0.9546
	0.6275	0.7379					0.9276
	0.6094	0.7148					0.9022
	0.5928	0.6935					0.8783

3:
Compensation of Errors
from Spherical Target Surfaces

3.1 Introduction

In the previous chapter, an Ansys finite element model was used to calculate capacitance values for a capacitance gage placed in close proximity to a target surface. Several different target surfaces were modeled, including a flat plane and spheres ranging in diameter from 6.35 mm (0.250 inches) to 25.4 mm (1.000 inches). The flat plane serves as a reference, from which the capacitance value of the probe that is expected by the electronics can be determined for a given gap distance.

When the same probe is placed in proximity to a curved surface, the capacitance of the system is now quite different. Since the electronics are unchanged, they will respond to the capacitance of the system only, therefore giving a false reading of distance.

In this chapter the capacitance values from Table 2-6 and Table 2-7 are exhaustively analyzed to determine a modified gain for each spherical diameter, as well as the expected deviations from linear. These gain and nonlinearity values are compared with unpublished experimental results from another laboratory, and a lookup table is created to correct the capacitance gage output. With this correction, the erroneous output of the capacitance gage electronics can be modified to account for the shape of the target surface.

3.2 Linearized Flat Target Results

Now that capacitance values have been determined for different distance values d, it is necessary to analyze the mathematics of the linearized output. As described in Chapter 1, the electronics associated with the capacitance gage are designed to linearize the output as a function of the inverse of the capacitance. This in turn is linear with respect to the distance. Rearranging Eq. (1-3), we have Eq. (3-1).

$$d = (\varepsilon_0 A) \cdot \left(\frac{1}{C}\right) \tag{3-1}$$

We know that the voltage output is proportional to the displacement Δd from a nominal or reference distance, which we will call d_r. Incorporating this gain G, the result is shown in Eq. (3-2).

$$V = G \cdot \Delta d = G(d - d_r) \tag{3-2}$$

Next, we substitute the right side of Eq. (3-1) into (3-6), using C_r for the capacitance associated with the reference distance d_r. The results are shown in Eq. (3-3).

$$V = G \cdot \varepsilon_0 A \left(\frac{1}{C} - \frac{1}{C_r}\right) \tag{3-3}$$

Finally, the $\varepsilon_0 A$ constant has been assigned the variable S throughout this discussion. Substituting into Eq. (3-3), we are left with Eq. (3-7).

$$V = G \cdot S \left(\frac{1}{C} - \frac{1}{C_r}\right) \tag{3-4}$$

3.2.1 Slope values for linear fit

Once the capacitance values for the flat target are tabulated, the first test of the data is to plot the gap distance d as a function of the inverse of the capacitance, $1/C$. This plot is shown in Figure 3-1 for both the "fine" gain setting of 394 V/mm (10 V/minch) and the "ultrafine" gain setting of 1969 V/mm (50 V/minch). These two ranges are named for the gain settings provided by Lion Precision in their electronics box. The lines plotted on the same graph represent the linear best fit for each range, showing that the data is highly linear as expected. Units for these plots throughout this chapter are mm for distance and pF^{-1} for inverse capacitance values. The slopes of these lines as calculated by Matlab and converted to metric units are shown in Eq. (3-5) and Eq. (3-6).

$$S_f = 38.6 \cdot 10^{-3} \, pF \cdot mm \tag{3-5}$$

$$S_{uf} = 32.3 \cdot 10^{-3} \, \text{pF} \cdot \text{mm} \tag{3-6}$$

The subscript on each S indicates the gain setting (fine or ultrafine). Reconfiguring the simplest form of the capacitance equation to fit to this plot, the slope should be the coefficient to the inverse capacitance in Eq. (3-1). Plugging in the known values for A and ε_0, the calculated value of the slope is as shown in Eq. (3-7).

$$S = \varepsilon_0 A = 20.4 \cdot 10^{-3} \, \text{pF} \cdot \text{mm} \tag{3-7}$$

As discussed in the previous chapter, the actual active area of the central conductor is somewhat greater than the flat area parallel to the target surface. Taking as the active area the central values for each range from Table 2-3, the theoretical slopes for the two different voltage ranges are calculated to be as shown in Eq. (3-8) and Eq. (3-9).

$$S_f = 33.8 \cdot 10^{-3} \, \text{pF} \cdot \text{mm} \tag{3-8}$$

$$S_{uf} = 27.5 \cdot 10^{-3} \, \text{pF} \cdot \text{mm} \tag{3-9}$$

These values are much closer to those taken from the plots. Since these values are taken from the same data this result is hardly surprising, nevertheless it is a good check of the consistency of the results and of the assumptions made in the analysis.

3.2.2 Nonlinear residuals

As the data points are so close to the best-fit line, it is helpful to display the results of the analysis in a way that elucidates the small deviations from linear. This is achieved by subtracting the linear approximation from the actual data, leaving only the nonlinear component of the data. The zero line therefore represents the linear fit, with the data points above it shown above the best-fit line. For all of these "residual" plots the units chosen for ease of understanding and consistency are μm and pF^{-1}. Figure 3-2 shows that the data points are slightly higher than the linear best-fit line at the extremes of the range, while in the middle of the range the data points fall slightly below the line. The total error over the valid data points is 0.241 μm (9.5 $\mu inch$).
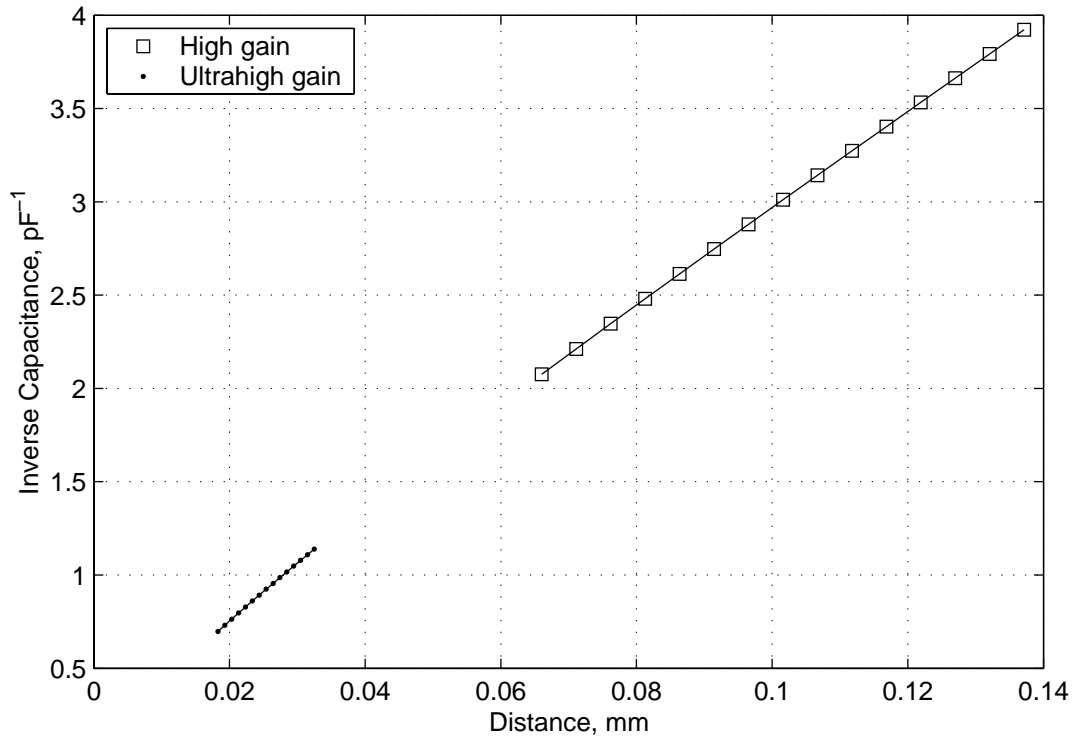
Figure 3-1. Linear relationship of *d* to *1/C* for a flat target surface for both fine and ultrafine gain settings.
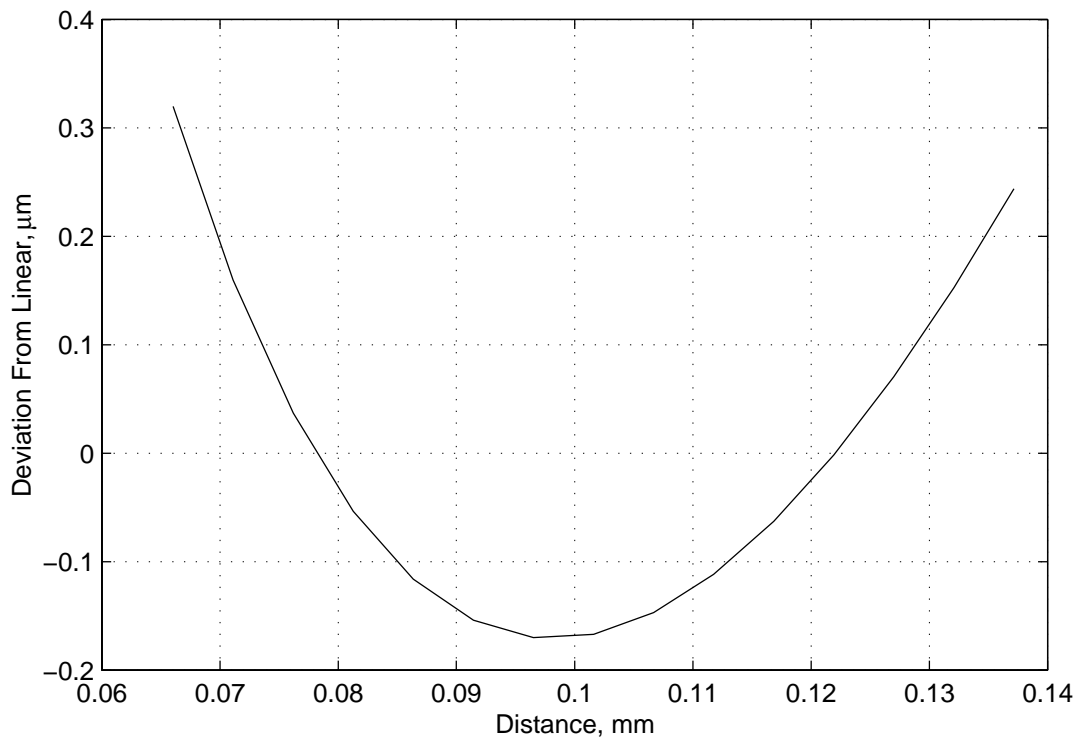
Figure 3-2. Nonlinear residual portion of flat target capacitance results for the fine gain setting.

An additional step in evaluating these results is to convert the distances *d* to displacements Δd, then convert the displacements to the units of the output of the capacitance electronics, which is in volts (V). This will allow comparison of the flat target results to calibration data from the capacitance gage manufacturer. Restating Eq. (3-2) and solving for *d*, we have Eq. (3-10).

$$d = \frac{V}{G} + d_r \qquad \textbf{(3-10)}$$

Once again, here *G* is the gain in V/mm and d_r is the nominal offset in mm. For the fine gain setting *G* = 394 and d_r = 0.1016. For the ultrafine setting *G* = 1969 and d_r = 0.0254. In either case, the voltage output ranges from −10 to +10 volts, which limits the active ranges for the fine and ultrafine gain settings to 0.0762-0.127 and 0.02032-0.03048 mm, respectively. Figure 3-3 shows a plot of the fine gain setting output voltage as a function of the inverse capacitance. It is important to note that the data calculated exceeds the active range of the capacitance gage. The output voltage is expected to "flatten out" or saturate outside of its valid range. The purpose of calculating capacitance values outside this range is to ensure that the data at the extreme ends of the valid range do not suffer from end effects when fitting curves to the graphs.

A final analysis of the flat target data is to calculate the nonlinear residual values from Figure 3-2 as a function of output voltage *V*. The resulting values are that the maximum deviations from linear are +126 mV and −67 mV.

It is now time to compare these results with calibration data from the manufacturer of the capacitance gage, Lion Precision. Data from a typical calibration curve is shown in Table 3-1 [24]. This table shows a total deviation from linear in the valid voltage range of only 0.08 μm (3 μinch) or 47 mV. Comparing this to Figure 3-2, it is clear that the performance of the capacitance gage is much better than the analysis would indicate.
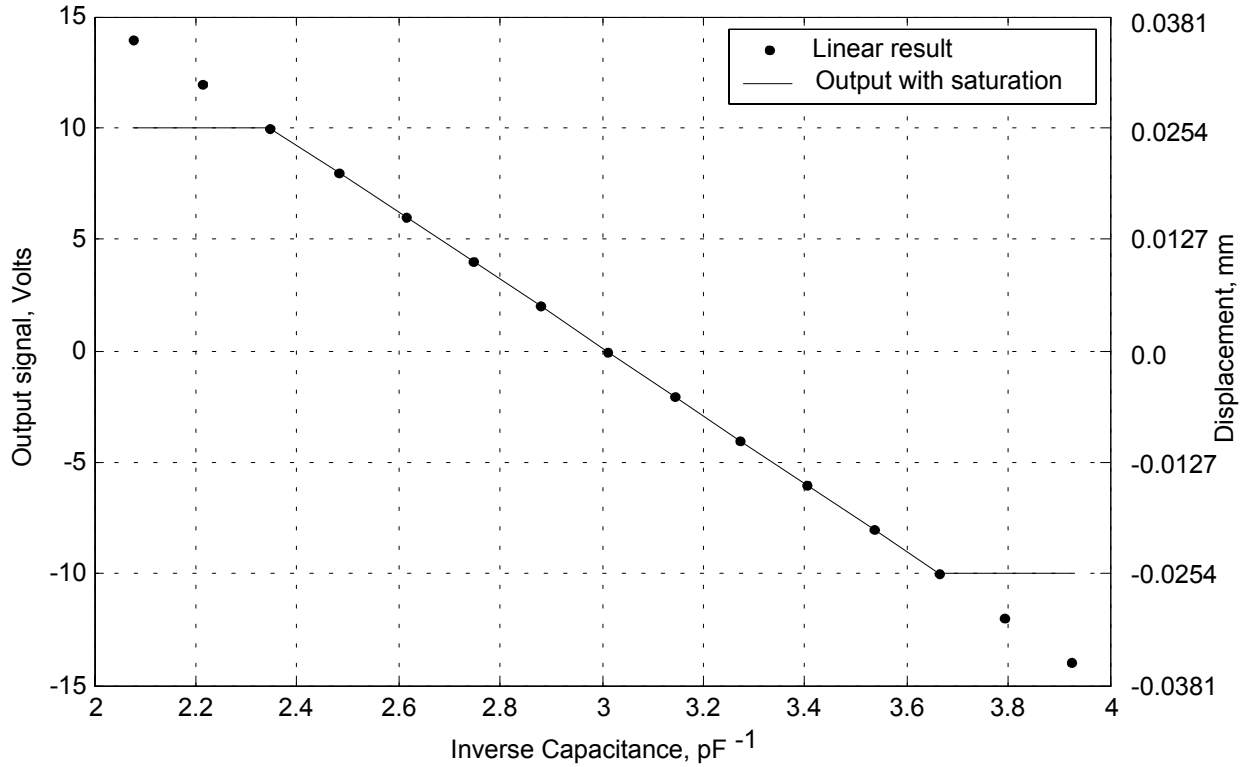
Figure 3-3. Plot of output voltage as a function of capacitance for the fine gain setting.

Table 3-1. Calibration data from a Lion Precision capacitance gage with fine gain setting.

Gap	Output	Output converted to	Error
milliinches	Volts	milliinches	milliinches
3.000	10.041	2.996	-0.004
3.125	8.778	3.122	-0.003
3.250	7.518	3.248	-0.002
3.375	6.260	3.374	-0.001
3.500	5.006	3.499	-0.001
3.625	3.753	3.625	0.000
3.750	2.503	3.750	0.000
3.875	1.253	3.875	0.000
4.000	0.000	4.000	0.000
4.125	-1.249	4.125	0.000
4.250	-2.500	4.250	0.000
4.375	-3.752	4.375	0.000
4.500	-5.001	4.500	0.000
4.625	-6.251	4.625	0.000
4.750	-7.499	4.750	0.000
4.875	-8.747	4.875	0.000
5.000	-9.994	4.999	-0.001
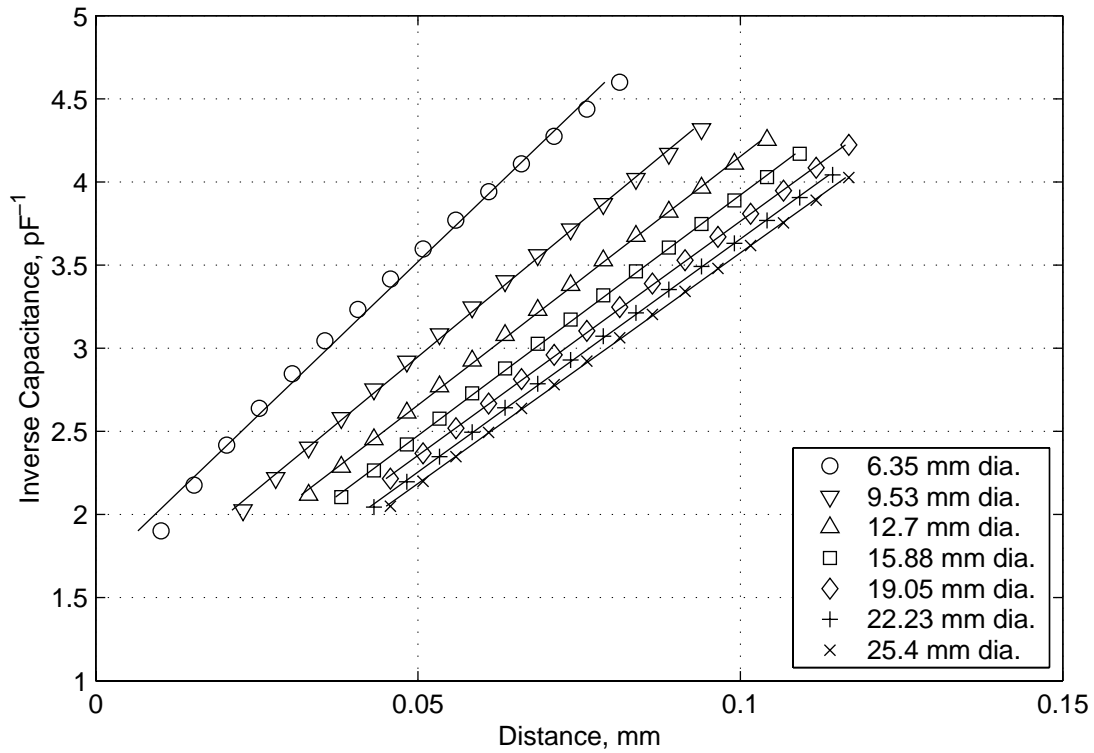
Figure 3-4. Linear approximations of *d* to *1/C* for spherical target surfaces and fine gain setting.
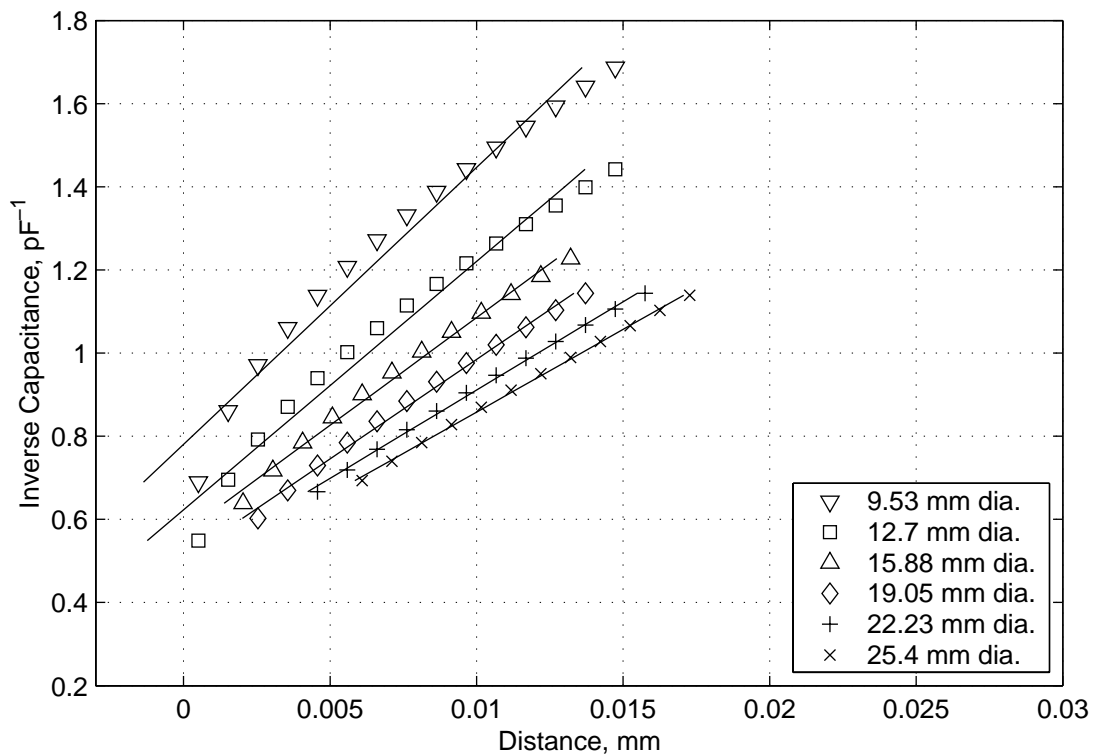
Figure 3-5. Linear approximations for spherical targets and ultrafine gain setting.

This discrepancy was solved by contacting the engineering staff at Lion Precision, the capacitance gage manufacturer. It is typical for an uncalibrated capacitance gage to show nonlinear errors of 0.508 μm (20 μinch) or more, in good agreement with the deviations shown in Figure 3-2. Fortunately, the electronics of the capacitance gage have the capability to correct for this deviation, and adjustment of the electronics to compensate for this linearity is part of the standard calibration procedure. It is critical during this analysis to remember that this correction exists in the electronics and should be included, if possible, in the analysis. The reader may wonder how this correction can be accomplished without opening the "black box" that represents the capacitance gage electronics. This will be described as the spherical results are analyzed.

3.3 Spherical Target Results

The data relating $1/C$ to the displacements for the spherical targets is less linear than the data from the flat targets, nevertheless it is illuminating to fit a straight line to the data as before. Seven different diameters were analyzed for the fine gain setting and six for the ultrafine setting. The data points and the corresponding fitted lines are plotted in Figure 3-4 for the fine gain setting and Figure 3-5 for the ultrafine gain setting.

The next step in the analysis of the spherical data is to correlate the displacements from the spherical surfaces to the displacements from the flat target surface. The capacitance gage of course has no way to "know" what kind of surface it is detecting, since the only value it is able to measure is the capacitance. Regardless of the shape of the surface, the capacitance gage electronics will sense the capacitance and output a voltage based on the flat surface calibration.

As an example, assume that the capacitance gage is in close proximity to a surface such that it senses a capacitance of 0.4 pF. A capacitance of 0.4 pF corresponds to an inverse value of 2.5 pF $^{-1}$. Looking at the curve in Figure 3-3, the output voltage corresponding to this capacitance is approximately –7.5 V, which from the voltage-displacement conversion equation corresponds to a distance of 0.0826 mm (3.25 minch). The displacement could have also been determined directly from Figure 3-1, but it is helpful to remember all the steps and conversions involved. Once again, the input that the system senses has nothing whatsoever to do with the shape of the surface, but only with the capacitance that it senses between the central conductor and the surface.

In an ideal world, then, the capacitance values listed in Table 2-6 and Table 2-7 for spherical surfaces would have resulted in capacitance values that corresponded precisely with different displacements from the flat surface. As an example, some data is reproduced, with complete displacement values, in Table 3-2.

Table 3-2. Sample displacement and capacitance values.

6.35 mm (0.250 in) diameter target					Flat target			
d, mm	d, minch	C, pF	$1/C$, pF^{-1}		d, mm	d, minch	C, pF	$1/C$, pF^{-1}
0.02032	0.8	0.4136	2.4178		0.0762	3.0	0.4261	2.3469
0.0254	1.0	0.3789	2.6392		0.08128	3.2	0.4031	2.4808
0.03048	1.2	0.3513	2.8466		0.08636	3.4	0.3825	2.6144
0.03556	1.4	0.3285	3.0441		0.09144	3.6	0.3641	2.7465
0.04064	1.6	0.3093	3.2331		0.09652	3.8	0.3473	2.8794
0.04572	1.8	0.2926	3.4176		0.1016	4.0	0.3322	3.0102
0.0508	2.0	0.2781	3.5958		0.10668	4.2	0.3183	3.1417
0.05588	2.2	0.2652	3.7707		0.11176	4.4	0.3056	3.2723
0.06096	2.4	0.2537	3.9417		0.11684	4.6	0.2938	3.4037
0.06604	2.6	0.2433	4.1102		0.12192	4.8	0.2830	3.5336
0.07112	2.8	0.2339	4.2753		0.127	5.0	0.2730	3.6630

From Table 3-2 the capacitance value for the 6.35 mm (0.250 inch) sphere at a distance of 0.04064 mm (1.6 minch) is 0.3093 pF, approximately equal to the capacitance value from the flat surface at a distance of 0.11176 mm (4.4 minch). Thus when the capacitance gage is 0.04064 mm from the sphere, it will sense a capacitance approximately equal to a distance of 0.11176 mm from a flat surface, and will output the voltage appropriate to that gap (+4 V). The final goal of the analysis is to correlate these displacements.

3.3.1 Linear fit solutions

There are two possible methods of calculating distances from one set of capacitance values to the other. The linear fit described in Section 3.2.1 is the most straightforward solution, since it uses the idealized approximation of a parallel plate capacitor. This method also has the advantage that capacitance values outside the analyzed range can nevertheless be correlated to displacement values. It will be shown that higher order polynomial fits do not allow extrapolation.

The first analysis of the data is achieved by using to the best-fit lines from Figure 3-1, plugging in the inverse capacitance values from a spherical measurement, and determining distance values d. As a graphical example, the inverse capacitance values from the third column of Table 3-2 are plotted along with the curve from Figure 3-1 in Figure 3-6 below. The horizontal lines show how the new displacements are determined from the plotted points.
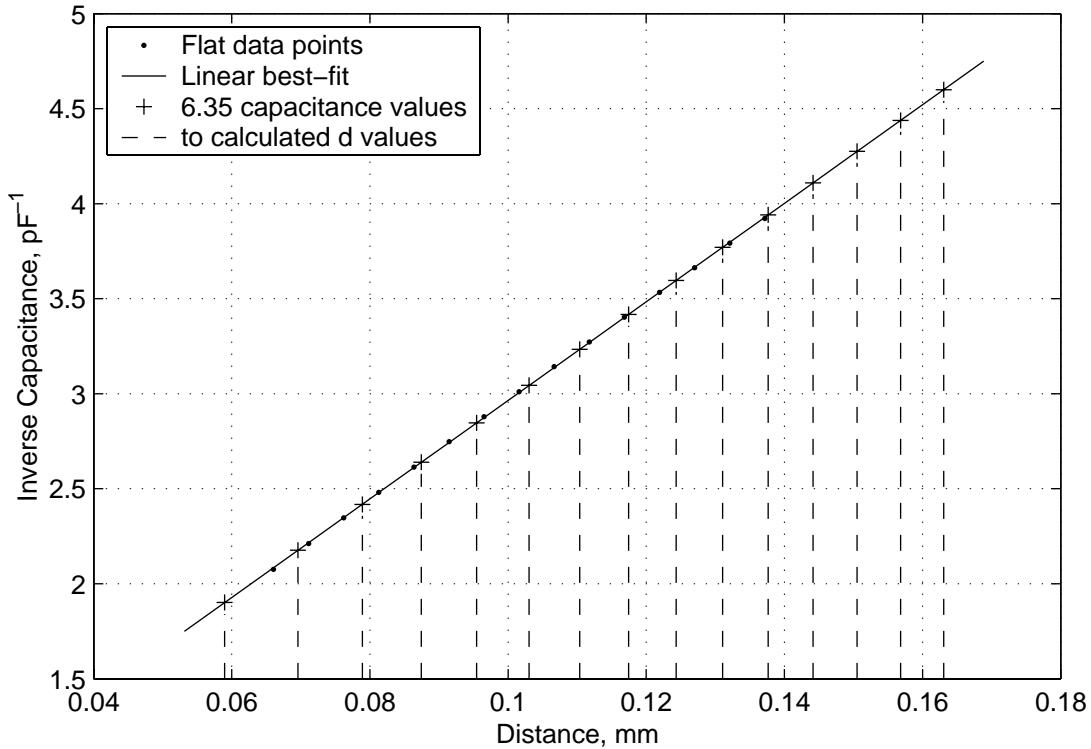
Figure 3-6. Correlating capacitance values to measured displacements.

Algebraically, the best-fit line takes the form of two coefficients P_1 and P_0, which are then used in combination with the capacitance values from the curved 6.35 mm (0.250 inch) surface, C_{0250}, as shown in Eq. (3-11).

$$d_{meas} = P_1 \cdot C_{0250}^{-1} + P_0$$ **(3-11)**

The coefficients are determined to be $P_1 = 1.5183$ and $P_0 = -0.5644$. It is important to distinguish between the distances that are used in the Ansys analysis and the distances that result from the above calculations. Since the distances in the Ansys analysis are the true distances to the surface, these are denoted as the "real" distances or d_{real}. The distances determined by the capacitance gage based on the flat surface are the distances that the system measures, hence the name d_{meas}. Finally, these distances can be converted to displacements Δd by subtracting the distance that produces zero voltage output. This terminology is used throughout the Matlab code that produced these results. As a flow chart, this process is as shown in Figure 3-7.
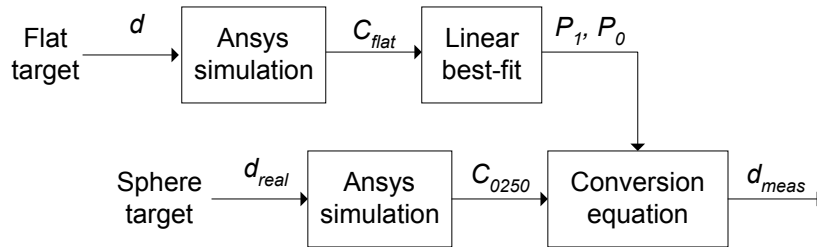
Figure 3-7. Block diagram of data conversion process.

Once the measured distance values d_{meas} are calculated, the results of the analysis can be plotted as a function of the actual distance d_{real}. Such plots are shown in Figure 3-8 for the fine gain setting and Figure 3-9 for the ultrafine gain setting. These plots can be considered as a lookup table relating one distance measurement to the other. The vertical scale can trivially be converted to voltage and the axes switched if the preferred format of this graph is to plot actual distance as a function of output voltage. In either case, a best-fit line can be determined with the slope representing the actual gain of the capacitance gage for a particular spherical target in V/mm.

There are of course other methods that can be used to analyze this same data. The plot of inverse capacitance for the flat target was converted to a voltage scale for Figure 3-3, centered at 0 V. The capacitance scale could also be centered on zero by subtracting the central value, but this results in a central value of 0 pF^{-1}, a relative term with no physical meaning. This should not affect the slope values but only the intercept. Capacitance data could also be converted to voltage before comparison, but again this results in additional conversions that may add to the overall error. By leaving voltage out of the conversion diagram of Figure 3-7, the method presented has the fewest steps.

There are, however, two problems with the described method that have only been alluded to thus far. The first problem has to do with the linear fit of the distance data d to $1/C$ for the flat target case. We have already seen that the residual error from this linear approximation has a total range of 0.241 μm (9.5 μinch). It is known that the electronics of the capacitance gage take into account the majority of this error, so that the actual error of the calibrated device is 0.0762 μm (3 μinch). It is therefore clear that by using only a linear fit we are not achieving quite the same conversion from capacitance to displacement that is produced by the electronics. A higher order fit must be carefully applied to the data to produce the most accurate conversion.
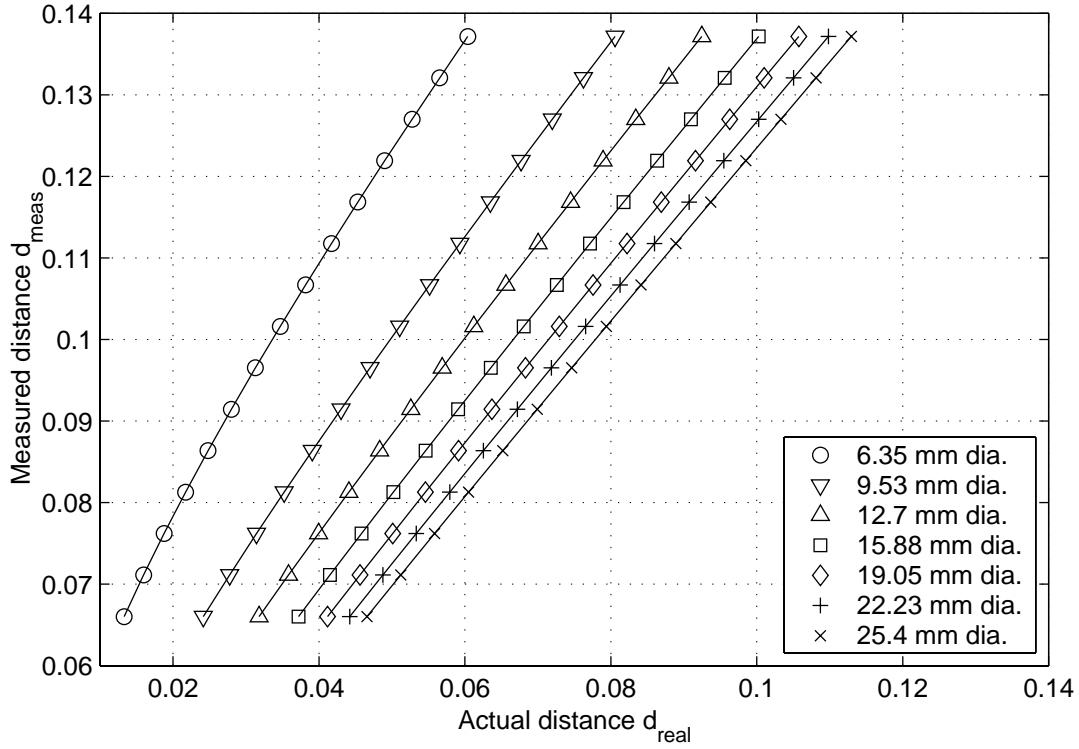
Figure 3-8. Plot of displacement measured as a function of actual displacement for different diameter spheres and fine gain setting.
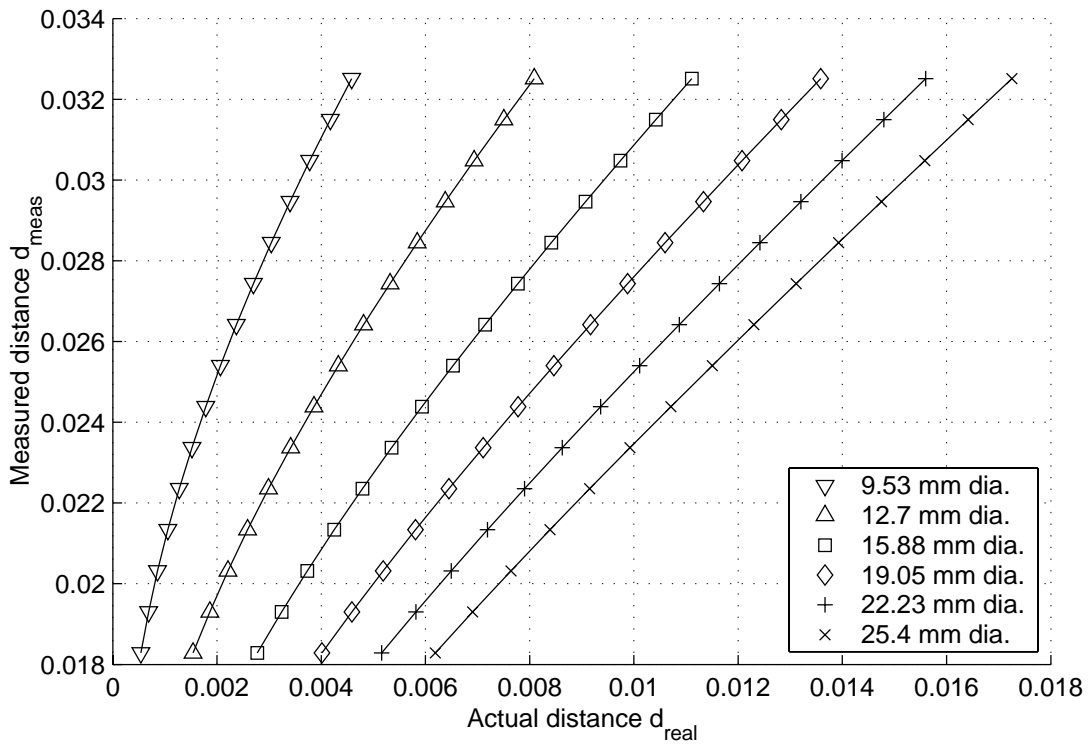
Figure 3-9. Plot of measured and actual displacement for ultrafine gain setting.

54

The second problem with the described method is with the ranges of capacitance values from the various Ansys simulations. As can be seen from Table 2-6 and Table 2-7, the exact ranges of capacitance do not match from the spherical targets to the flat targets. Generally speaking, the spherical target range exceeds that of the flat target range, since the gain of the spherical targets is greater than the nominal gain from a flat target surface. When the capacitance of the spherical distance d_{real} is converted to an equivalent distance d_{meas} on the flat scale, the range of displacements does not perfectly match the active range of the capacitance gage. For ultrafine gain settings and small diameters the plot of d versus $1/C$ is highly curved, so any deviation from the full range of the device will result in a significant skewing of the resulting slope. Since the 12-15 data points resulting from the Ansys simulation cannot precisely mimic the full range of the flat capacitance values, a slightly different technique must be employed.

3.3.2 Higher-order polynomial solutions

The technique using higher-order polynomial fits requires two changes to the previous, linear method. First, a higher order polynomial fit is employed to the data. Second, the spherical data, rather than the flat data, is fit to a polynomial, and real distance values are calculated from that. A block diagram of this improved method is shown in Figure 3-10, which can be compared and contrasted with Figure 3-7. The equation associated with this higher order fit is shown in Eq. (3-12). When this technique is employed, the range of real values that are output precisely match the output range of the capacitance gage electronics. When theoretical results are compared with empirical tests, the same data range is now used in each.
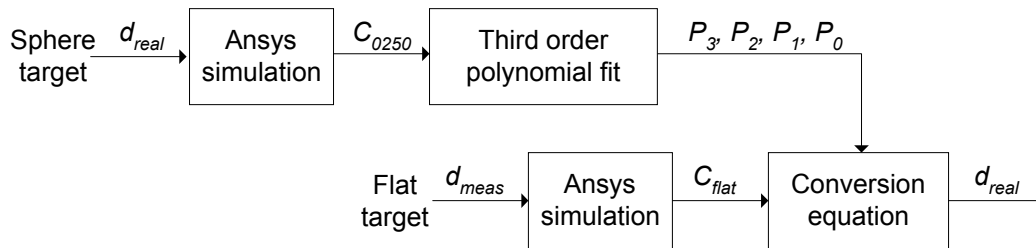
Figure 3-10. Block diagram of improved data conversion process.

$$d_{real} = P_3 \cdot C_{flat}^{-3} + P_2 \cdot C_{flat}^{-2} + P_1 \cdot C_{flat}^{-1} + P_0 \tag{3-12}$$

The first problem with the original method, that of not correcting for the nonlinearity of the electronics, has now also been taken care of. To determine the order of polynomial necessary

to achieve a good fit to the simulated data, several different orders of polynomial were applied to the same data, as shown in Figure 3-11. Although the coefficients differ significantly, all of these functions are able to interpolate between data points to almost exactly the same curve. The problems occur when any of the functions are asked to extrapolate beyond the data plotted. These extrapolations are also shown in Figure 3-11.

Obviously a higher order polynomial fit is an extremely poor way to extrapolate beyond the existing data. Care has been taken, then, to ensure that the data ranges of capacitance on the curved surfaces is always *greater* than the data range for the flat target surface. When the capacitance values from the flat target simulation are applied to a curve such as the one shown in Figure 3-11, the displacement values are always interpolated between existing capacitance values. This results in a minimum error from the conversion process. It also means that coefficients must be calculated for every spherical target and gain setting, rather than using a common set of coefficients. In the interest of completeness, these coefficients are presented in Table 3-3. It is important to note that there is no *physical* significance to the values of these coefficients, they are only for the purposes of interpolating the existing data. If in the future a closed-form solution or approximation is made of this problem, then a different form of equation may be fit to the data points, one that is better able to extrapolate the data values.

Once the curve fitting scheme of Figure 3-10 has been applied to the data, the plots in Figure 3-8 and Figure 3-9 are produced. Each curve of these plots contains 15 data points, corresponding to the capacitance values of the 15 data points of the flat target surface. These flat target values include the full travel range of the capacitance gage, plus two additional data points at each end of the data. The central 11 data points thus represent the active range of the capacitance gage, and it is these 11 points that will be used in the next step of the analysis.
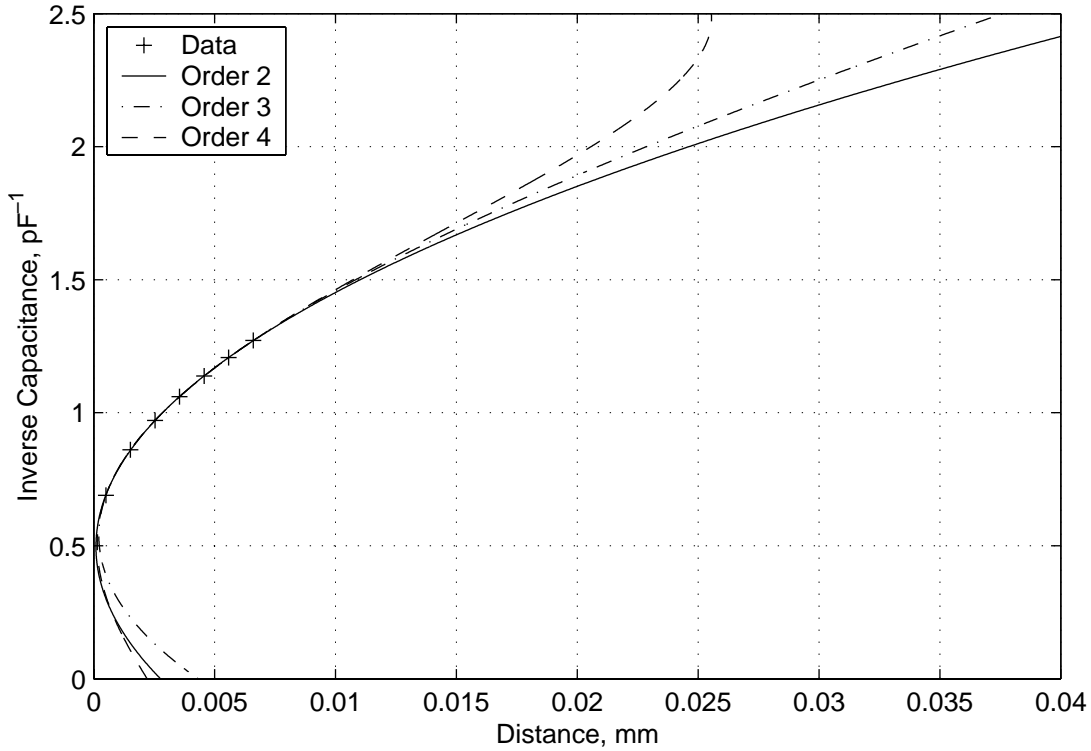
Figure 3-11. Different order polynomial fits to the same empirical data.

Table 3-3. Table of polynomial coefficients for different diameter spheres and gain settings.

Diameter	Fine Gain Setting					Ultrafine Gain Setting				
	P_4	P_3	P_2	P_1	P_0	P_4	P_3	P_2	P_1	P_0
6.350 mm (0.250 in)	0.0009	-0.0221	0.2163	-0.2343	0.0162					
9.525 mm (0.375 in)	0.0007	-0.0155	0.1448	0.2109	-0.3353	0.0230	-0.1685	0.6146	-0.5252	0.1375
12.70 mm (0.500 in)	0.0004	-0.0098	0.0939	0.4683	-0.4482	0.0454	-0.2990	0.8648	-0.5446	0.1038
15.88 mm (0.625 in)	0.0003	-0.0072	0.0694	0.6003	-0.4534	0.0816	-0.4623	1.0980	-0.5387	0.0784
19.05 mm (0.750 in)	0.0002	-0.0047	0.0489	0.6969	-0.4476	0.0974	-0.5133	1.1153	-0.3974	0.0313
22.23 mm (0.875 in)	0.0002	-0.0048	0.0460	0.7323	-0.4003	0.0902	-0.4667	0.9866	-0.1916	-0.0204
25.40 mm (1.000 in)	0.0002	-0.0039	0.0385	0.7727	-0.3737	0.0785	-0.4024	0.8398	-0.0015	-0.0616

3.3.3 Justification for relative permeability approximation

Now that higher order polynomial fits have been applied to the mapping of the capacitance values, it is appropriate to discuss the reasons why the exact relative permeability of

air ε_R is of little consequence to this analysis. Table 3-4 shows some capacitance calculations

performed both without and with the relative permeability of air (ε_R = 1.0008) included.

Table 3-4. Table comparing capacitance values
before and after including relative permeability.

d, mm	*d*, minch	C_{flat}	C_{flat}, including ε_R	Ratio 1 + Δ
0.018288	0.72	1.4342330	1.4352240	1.000691
0.021336	0.84	1.2564640	1.2573270	1.000687
0.024384	0.96	1.1211030	1.1218700	1.000684
0.027432	1.08	1.0142710	1.0149630	1.000682
0.030480	1.20	0.9275919	0.9282233	1.000681

The final column of this table calculates the ratio of the capacitance with the relative

permeability to the value without this term. We expect this value to be 1.0008, but in fact these

are very close to 1.0007. The reason behind this discrepancy is in the fact that there are two

materials present in the analysis, air and an epoxy, and we have changed the relative

permeability of only one of them. Therefore the effect on the total capacitance is slightly less

than the size of the multiplier. Since this ratio is not precisely the value of ε_R, it is given the

moniker 1 + Δ.

Returning to the coefficients derived from a best fit polynomial, P_3, P_2, P_1, and P_0, we

want to see how the addition of the 1 + Δ term will affect these coefficients. This is identical to a

change of variables, with * representing the new values as shown in Eq. (3-13). Substituting in

for the value of *C* produces the line fitting formula in Eq. (3-14). The new multipliers can be

lumped together with the coefficients, to produce new *P* values such as the example shown in Eq.

(3-15).

$$C^* = (1+\Delta)C \tag{3-13}$$

$$d_{real} = P_3\left(\frac{(1+\Delta)^3}{C_{sph}^{*3}}\right) + P_2\left(\frac{(1+\Delta)^2}{C_{sph}^{*2}}\right) + P_1\left(\frac{(1+\Delta)}{C_{sph}^{*}}\right) + P_0 \tag{3-14}$$

$$P_3^* = P_3 \cdot (1+\Delta)^3 \tag{3-15}$$

The next step in this evaluation is to use these new coefficients together with new

capacitance values to determine what effect they will have on the output of the final curve fitting.

Equation (3-12) is rewritten with the new coefficients and new capacitance values as shown in Eq. (3-16). But, if we now substitute in values for P from Eq. (3-15) and values for C from Eq. (3-13), we end up with Eq. (3-17), which is identical to Eq. (3-12). In as much as the Δ term is constant, the inclusion or omission makes no difference to the distance calculations!

$$d_{real} = P_3^*\left(\frac{1}{C_{flat}^{*3}}\right) + P_2^*\left(\frac{1}{C_{flat}^{*2}}\right) + P_1^*\left(\frac{1}{C_{flat}^*}\right) + P_0 \tag{3-16}$$

$$d_{real} = P_3\left(\frac{1}{C_{flat}^3}\right) + P_2\left(\frac{1}{C_{flat}^2}\right) + P_1\left(\frac{1}{C_{flat}}\right) + P_0 \tag{3-17}$$

The ratios calculated in Table 3-4 showed that over the active range of the capacitance gage the Δ term varied slightly, a factor of about 1 in 100,000. Therefore we expect that the omission of the ε_R term will affect the accuracy of the final results at the 0.001% level. In evaluating this error, it should be noted that the relative permeability used for the epoxy material, 3.8, is only given to two significant figures. It has been indicated that it is the interplay between these two relative permeabilities that causes the variation in the ratios in Table 3-4. Of much greater importance to increasing the accuracy of the capacitance calculations, then, is a determination of the value of ε_R for the epoxy to a greater number of significant figures.

3.4 Applying the Correction

There are several ways to apply these correction curves once they have been accurately calculated. The simplest method is to use a linear approximation to the curves in Figure 3-8 and Figure 3-9, calculating from this a new slope and a new nominal offset position. Both of these values should be determined not from the full 15 data points, but from the central 11, which represent the active travel range of the capacitance gage.

There are two possible offset values that can be determined from each data curve. The graph in Figure 3-12 shows the most nonlinear data curve, that of the 9.525 mm (0.375 inch) sphere and the ultrafine gain setting. Also shown is the best-fit line through the central 11 data points. This line deviates from the data in the center and at the edges, as expected from a least-squares linear fit. The central data point, which corresponds to the flat surface offset displacement of 0.0254 mm (1.0 minch), is therefore not the same as the location where this line

crosses the flat surface offset. If the central data point were used as the offset value, the entire line would be shifted to the right, resulting in an increase in the overall error of the fit. The correct nominal offset value must be derived from the crossing point of the best-fit line.

It is important to note that this analysis assumes that all or most of the active range of the capacitance gage is to be used in a specific application. The best-fit line approximation is equally weighted across the full output range, therefore error is minimized as long as the data collected from a particular experiment are also equally distributed. If this is not the case, more accurate curve fitting can be achieved for a particular range of data. This will be discussed in more detail as part of the discussion of corrections to the Donaldson Reversal technique.
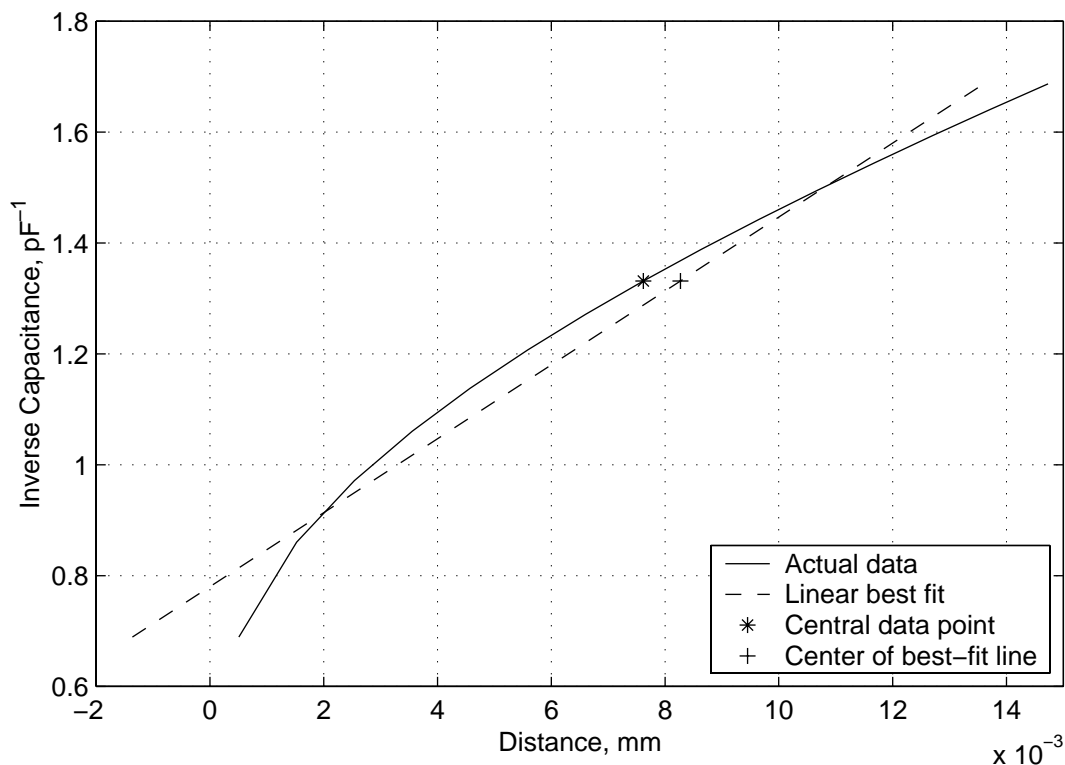
Figure 3-12. Plot of linear fit to 9.525 mm diameter sphere ultrafine gain curve, showing two possible values for the nominal offset.

For clarity it is necessary to show the algebra needed to convert one displacement into another. Until now, we have converted capacitance values to displacement values and vice-versa. Now we are converting displacement values to displacement values, probably a more confusing prospect. As discussed before, the actual displacement from the gage to the curved surface is termed d_{real}. The displacement that the capacitance gage electronics "believe" that it is from the surface, based on the erroneous assumption that the surface is flat, is termed d_{meas}, and it is the

conversion between these two distances that we must describe algebraically. Calculating from the slope and offset values, we write Eq. (3-18).

$$\frac{G_{fit}}{G_{flat}}\left(d_{meas} - d_r\right) = d_{real} - d_{r0} \qquad\qquad \textbf{(3-18)}$$

In this equation G_{fit} is the calculated slope of the best-fit line, G_{flat} is the gain for a flat surface (394 V/mm or 10 V/minch for the fine gain setting, 1969 V/mm or 50 V/minch for the ultrafine gain setting), d_r is the nominal offset for the measured value (0.1016 mm or 4.0 minch for the fine gain setting, 0.0254 mm or 1.0 minch for the ultrafine gain setting) and d_{r0} is the calculated nominal offset value. Values of G_{fit} and d_{r0} appear in Table 3-5.

Table 3-5. Slope and offset values for linear best-fit curves to displacement measurements.

Diameter, mm	Fine Gain Setting		Ultrafine Gain Setting	
	Slope, V/mm	Offset, mm	Slope, V/mm	Offset, mm
flat	393.7	0.1016	1968.5	0.02540
6.350	586.2	0.047244		
9.525	492.8	0.059248	6766.0	0.00827
12.700	459.4	0.069139	4208.5	0.00823
15.875	442.6	0.074117	3315.0	0.00934
19.050	432.6	0.081643	2895.9	0.00982
22.225	426.0	0.079111	2661.6	0.01181
25.400	421.2	0.081618	2515.3	0.01331

For applications where this first-order approximation is insufficiently accurate, it is necessary to include either an error map or a higher order approximation. Error maps for the fine and ultrafine gain settings are presented in Figure 3-13 and Figure 3-14, respectively. Although this data can be presented in terms of output voltage, in most cases an experimentalist will have already converted the voltage output of the capacitance gage to a distance or displacement value. Application of the error map values becomes the final step in the postprocessing of the data. For this reason the complete nonlinear residues R are shown as a function of the measured distance d_{meas}. To apply this residue to measured data the slope and offset must first be corrected as before, then the residue function added to the end result. This is the previous equation rearranged slightly and with an additional term, as shown in Eq. (3-19).
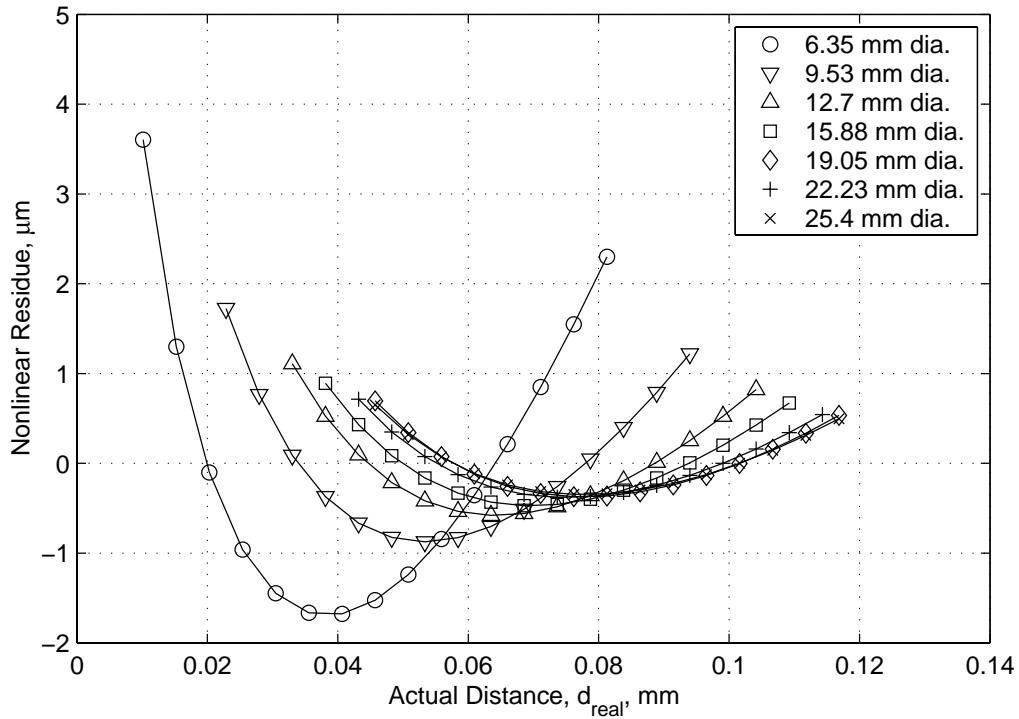
Figure 3-13. Nonlinear residue (error map) curves for fine gain setting.
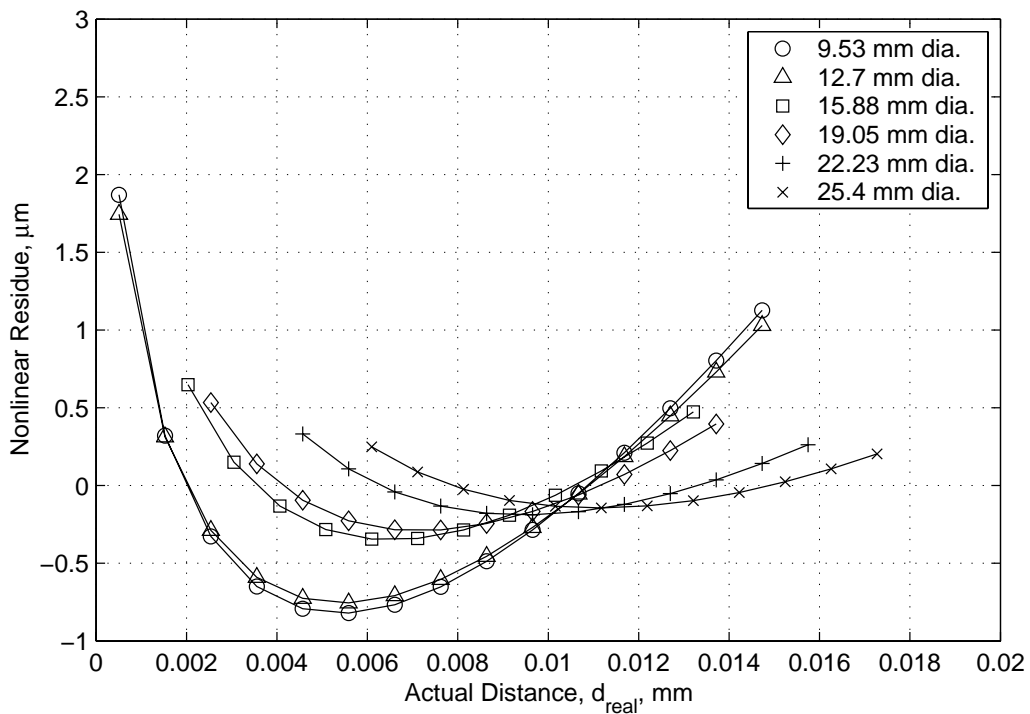
Figure 3-14. Nonlinear residue (error map) curves for ultrafine gain setting.

$$\frac{G_{fit}}{G_{flat}}\left(d_{meas} - d_r\right) + d_{r0} + R\left(d_{meas}\right) = d_{real} \tag{3-19}$$

The higher order approximation of the "lookup table" can be accomplished any number of ways, using any one of several different formats of the function. No attempt has been made to find a function that is a good extrapolation of the data. Care was taken throughout the Ansys simulations to ensure that the active range of the capacitance gage was covered when simulating the curved surfaces, so that higher order curves are only used to fit interpolated values.

Rather than try and invert or analyze the previous curve fitting algorithms, the best approach to a higher order approximation is to simply begin with the 15 data points for each curved surface and derive a third-order polynomial from this data. We choose to use the measured data values as the abscissa, since it is anticipated that most conversions will be from measured displacements to real displacements. All 15 data points are used since this will undoubtedly improve the curve fitting at the ends of the active range, with little or no loss in accuracy at the center values of the curve. As with the previous curve fitting, it was found that third, fourth, or fifth order polynomials all showed excellent ability to fit a smooth curve, therefore for simplicity the third order polynomial was used. The form of this solution is then as shown in Eq. (3-20).

$$d_{real} = P_A \cdot d_{meas}^3 + P_B \cdot d_{meas}^2 + P_C \cdot d_{meas} + P_D \tag{3-20}$$

These new coefficients P_A through P_D have no relationship to the previous curve-fitting coefficients. Code for calculating all of these coefficients is included in Appendix C.

3.5 Application to Donaldson Reversal

For application such as Donaldson Reversal, either of the two correction methods can be applied to previously collected data. The first-order (linear) correction can be applied by multiplying existing data by the increase in gain from its nominal value; namely, the unitless term in Eq. (3-21).

$$\frac{G_{fit}}{G_{flat}} \tag{3-21}$$

Notice that this multiplier will increase all of the measured values in an experiment, including out-of-roundness (OOR) and other errors. Since all of the measurements for Donaldson Reversal are of relative displacement, there is no need to add or subtract the nominal offset distances.

If a new experiment is planned, three precautionary steps can ensure that the linear fit achieves the best results. The first step is to center both the "normal" and "reverse" measurements on the active scale. Although this makes no difference whatsoever when a linear model of a capacitance gage is assumed, it makes a great deal of difference when the actual curves are analyzed. Looking again at the worst-case scenario in Figure 3-12, the curve gets gradually steeper from left to right. Fitting a line to the leftmost 5 points results in a slope of 10787 V/mm (274 V/minch) whereas fitting a line to the rightmost 5 points results in a slope of 5157 V/mm (131 V/minch), a difference of over 50 %. A subset of 5 data points centered on the middle of the active range of the capacitance gage results in a slope of 6772 V/mm (172 V/minch), which is quite comparable to the slope of the entire line as given in Table 3-5. If the normal and reverse measurements have significantly different slopes, then the equations used to separate the surface errors from the spindle errors are no longer valid. Worse still, the information of absolute position is lost once these values are combined, so postprocessing corrections can only be applied to the raw data.

The second suggested step to achieving the maximum linearity for a Donaldson Reversal experiment is somewhat counterintuitive: use a lower gain setting. This at first seems nonsensical, since of course the maximum resolution is achieved at the highest gain setting. But given the analysis of the nonlinearity to this point, such an assumption should be examined closely. The resolution δd of a capacitance gage measurement is given by the number of A/D bits N, the gain G, and Eq. (3-22).

$$\delta d = \frac{20}{G \cdot 2^N} \tag{3-22}$$

For a 16-bit A/D and the nominal ultrafine gain setting of 1969 V/mm (50 V/minch), this resolution is 0.15 nm (0.006 μinch). Looking back at the error map for the ultrafine gain setting as presented in Figure 3-14, it is clear that the accuracy is some 4 orders of magnitude less than this. The highest gain setting, therefore, only imbues a false sense of increased accuracy.

At first comparison, it appears as though the overall error of the fine gain setting as shown in Figure 3-13 is much larger than the overall error of the ultrafine gain setting shown in Figure 3-14. Consider, though, that the active range of the capacitance gage in the fine gain setting is five times greater. To make a fair comparison, the central 0.01 μm (0.4 μinch) of travel for the fine gain setting should be compared with the total travel at the ultrafine gain setting. When this comparison is made for the case of the 12.7 mm (0.5 inch) sphere, the error range is 1.2 μm (47 μinch) for the ultrafine gain setting, and only 0.08 μm (3 μinch) for the fine gain setting.

The reason that the ultrafine gain setting is more nonlinear than the fine gain setting is a straightforward one. For the fine gain setting the nominal distance from a flat surface is 0.1 mm (4.0 minch). When the 12.7 mm (0.5 inch) sphere is moved to a position that produces the equivalent capacitance, this distance is 0.0612 mm (2.41 minch), some 40 % closer. For the ultrafine gain setting, the nominal offset is 0.0254 mm (1.0 minch), which is simulated when the gage is positioned at a distance of only 0.00432 mm (0.17 minch), some 83 % closer. It is the fact that the surface position required to achieve the equivalent capacitance is off by such a great degree that causes the nonlinearity to be heightened at the ultrafine gain setting. Put another way, when the curved surface is closer, there is a larger difference between the closest and furthest areas. When the curved surface is further away, the discrepancy is a smaller percentage of the overall distance.

The final suggested step should be obvious from comparing the results of the various sphere diameters. This suggestion is as follows: use the largest sphere conveniently available. As the sphere diameter increases the area comparable to the central conductor of the capacitance gage becomes flatter and the corresponding data more linear. Although not simulated in this work, it is postulated that a cylindrical surface of equivalent radius will have less than half of the nonlinear error associated with the spherical surface.

3.6 Experimental Verification

All of the Ansys simulations presented in this paper were designed to allow experimental confirmation. The geometry of the capacitance gage represents the model C1-C manufactured by Lion Precision, and the sphere diameters modeled are also readily available. The electronic

control circuitry that has been discussed previously also represents the actual electronics in use in the Precision Systems Laboratory at the University of Kentucky.

Several experiments with spherical targets have been performed in parallel with this finite element simulation. Prof. Eric Marsh of the Machine Dynamics Research Laboratory at the Pennsylvania State University [25] has utilized two capacitance gages to directly compare the output of a capacitance gage against a flat surface with the output of a capacitance gage against a spherical surface. A photograph of the experimental setup appears in Figure 3-15. A diagram of this same experimental setup is provided in Figure 3-16.

In this experiment, the capacitance gage on the left is held parallel and in close proximity to a flat, machined surface. On the right, a second cap gage targets a spherical surface. Both target surfaces are supported by a large gage block from below, while the capacitance gages are supported from above. Structural support and relative movement are provided by a Moore machine base, also pictured in Figure 3-15.
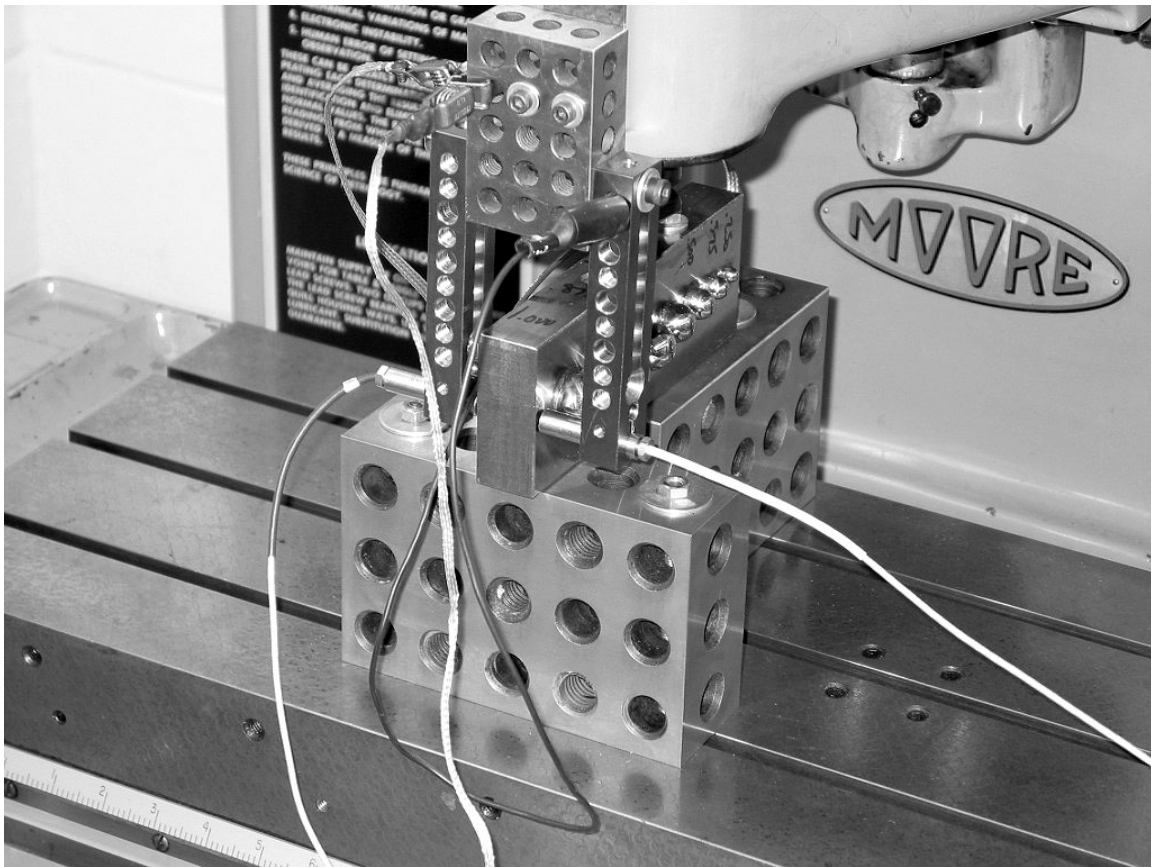
Figure 3-15. Photo of experimental setup for verification of nonlinearity data.

66
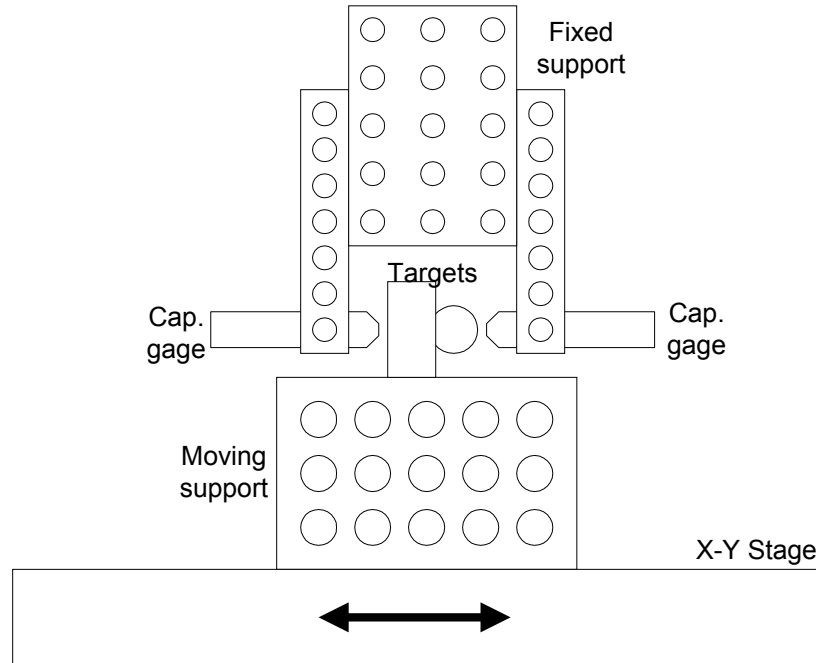
Figure 3-16. Diagram of experimental setup showing moving and fixed components.

As the worktable supporting the target surfaces is moved back and forth in the x direction, the capacitance gages sense the changing gaps on either side of the moving target. The output of the capacitance gage electronics is sent to a data acquisition card in a PC, where the analog voltage output is digitized. This data acquisition card collects a large number of data points alternately from each capacitance gage, but this collection can be assumed to be simultaneous when the sampling time is much less than the travel speed of the worktable. Although one sphere is shown in the diagram, all seven spheres are mounted to the central gage block. To change to a different diameter sphere, the table is moved in the y direction and the capacitance gage repositioned.

If we consider for a moment the case where both gages are positioned in close proximity to a flat surface and perfectly calibrated, it would be expected that the sum of the gap on the left and the gap on the right would be a constant value. This can also be written as shown in Eq. (3-23).

$$R(t) = K - F(t) \qquad\qquad \textbf{(3-23)}$$

In this equation R is the right measurement, F is the left, and K a constant. Since the value K is not expected to change, this type of setup is sometimes referred to as a "null"

67

experiment. Although temperature changes would of course cause the structural blocks to expand or contract, affecting the gaps, the experiment is completed on such a short time scale (less than a minute) that temperature changes are deemed negligible.

When the capacitance gage on the right is positioned over a sphere, the resulting data reveals the differences between the flat measurement F and the round surface measurement R. We can consider this flat measurement as the actual or "real" distance, and the round measurement the measured distance. Using the nomenclature used to analyze the theoretical results and dropping the constant for convenience, the experimental results become Eqs. (3-24) and (3-25).

$$d_{real} = -F(t) \qquad \text{(3-24)}$$

$$d_{meas} = R(t) \qquad \text{(3-25)}$$

An example of the raw experimental data is shown in Figure 3-17. As expected, the flat and round data are in opposing directions. Also note that at the extreme end of each pass one or both capacitance gages exceed the calibrated scale (from –10 V to +10 V). As these data points are not considered to be calibrated, they will be discarded. Finally note that there are positions where the motion of the stage pauses briefly. This is due to backlash in the lead screw of the Moore machine and has little impact on the analysis of the data.

Using the above equations, experimental lookup tables can be produced and plotted that have the same appearance and function as Figure 3-8 and Figure 3-9. A better graphical representation is achieved by first calculating the best-fit line, then plotting the residual error. These new plots appear in Figure 3-18 and Figure 3-19, these can be compared to the theoretical results in Figure 3-13 and Figure 3-14. Table 3-6 compares the theoretical slopes of the best-fit line to the calculated slopes from the empirical data [26].

The form of the nonlinear residue curves is quite comparable, showing the same nonlinear trends and the increase in nonlinearity as the diameter is decreased. In terms of absolute value, a comparison of these shows that in all cases the theoretical error map is actually slightly larger than the empirical error map. It is hypothesized that one possible reason for this discrepancy may be the presence of additional conductors in the circuit that add small amounts

of capacitance to the value calculated in Ansys. The presence of an additional capacitance term may reduce the magnitude of the correction, but further work would be required to prove this.
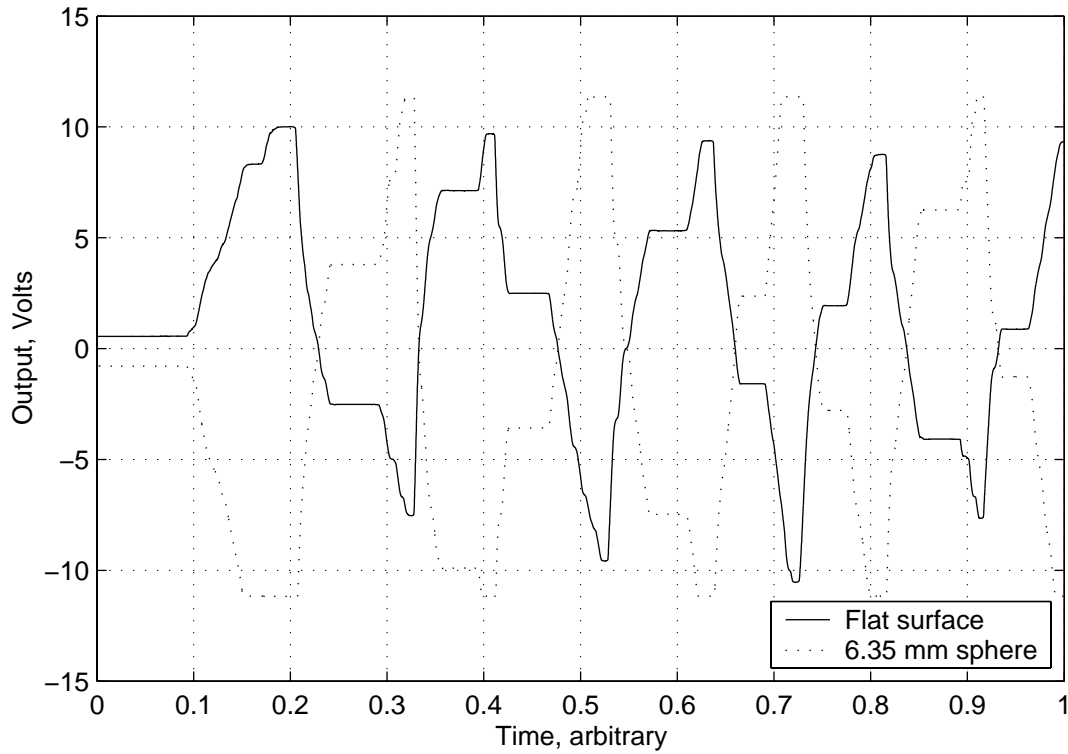
Figure 3-17. Raw traces of flat and round surface measurements.

Table 3-6. Comparison of best-fit slopes between theoretical calculations and experimental results.

Diameter	Fine Gain Setting		Ultrafine Gain Setting	
	Slope, From Ansys	Slope, Experimental	Slope, From Ansys	Slope, Experimental
Flat	393.7 V/mm (10.0000 V/minch)	-	1968.5 V/mm (50.0000 V/minch)	-
6.35 mm (0.250 in)	586.1929 V/mm (14.8893 V/minch)	570.9 V/mm (14.5 V/minch)	-	-
9.525 mm (0.375 in)	492.752 V/mm (12.5159 V/minch)	488.2 V/mm (12.4 V/minch)	6765.98 V/mm (171.8559 V/minch)	-
12.7 mm (0.500 in)	459.3976 V/mm (11.6687 V/minch)	452.8 V/mm (11.5 V/minch)	4208.457 V/mm (106.8948 V/minch)	4535.4 V/mm (115.2 V/minch)
15.875 mm (0.625 in)	442.6299 V/mm (11.2428 V/minch)	437.0 V/mm (11.1 V/minch)	3315.008 V/mm (84.2012 V/minch)	3464.6 V/mm (88.0 V/minch)
19.05 mm (0.750 in)	432.6142 V/mm (10.9884 V/minch)	429.1 /mm (10.9 V/minch)	2895.937 V/mm (73.5568 V/minch)	2763.8 V/mm (70.2 V/minch)
22.225 mm (0.875 in)	425.9646 V/mm (10.8195 V/minch)	425.2 V/mm (10.8 V/minch)	2661.583 V/mm (67.6042 V/minch)	2578.7 V/mm (65.5 V/minch)
25.4 mm (1.000 in)	421.2402 V/mm (10.6995 V/minch)	417.3 V/mm (10.6 V/minch)	2515.264 V/mm (63.8877 V/minch)	2460.6 V/mm (62.5 V/minch)
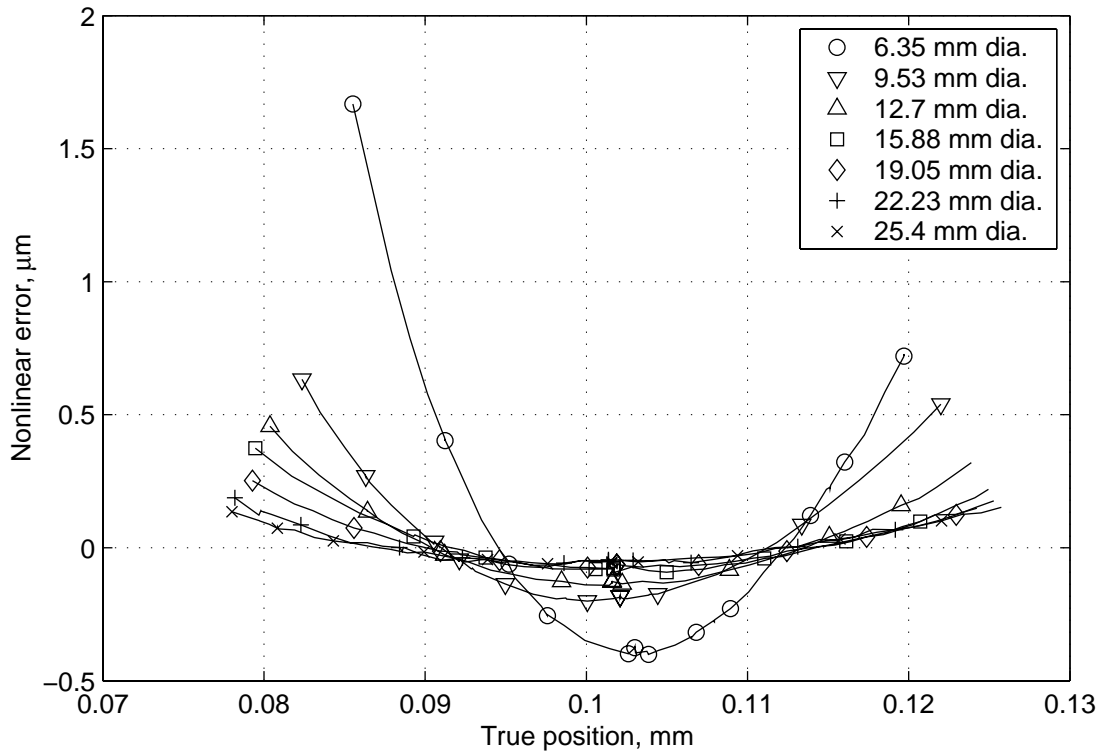
Figure 3-18. Nonlinear residue for experimental data from the fine gain setting.
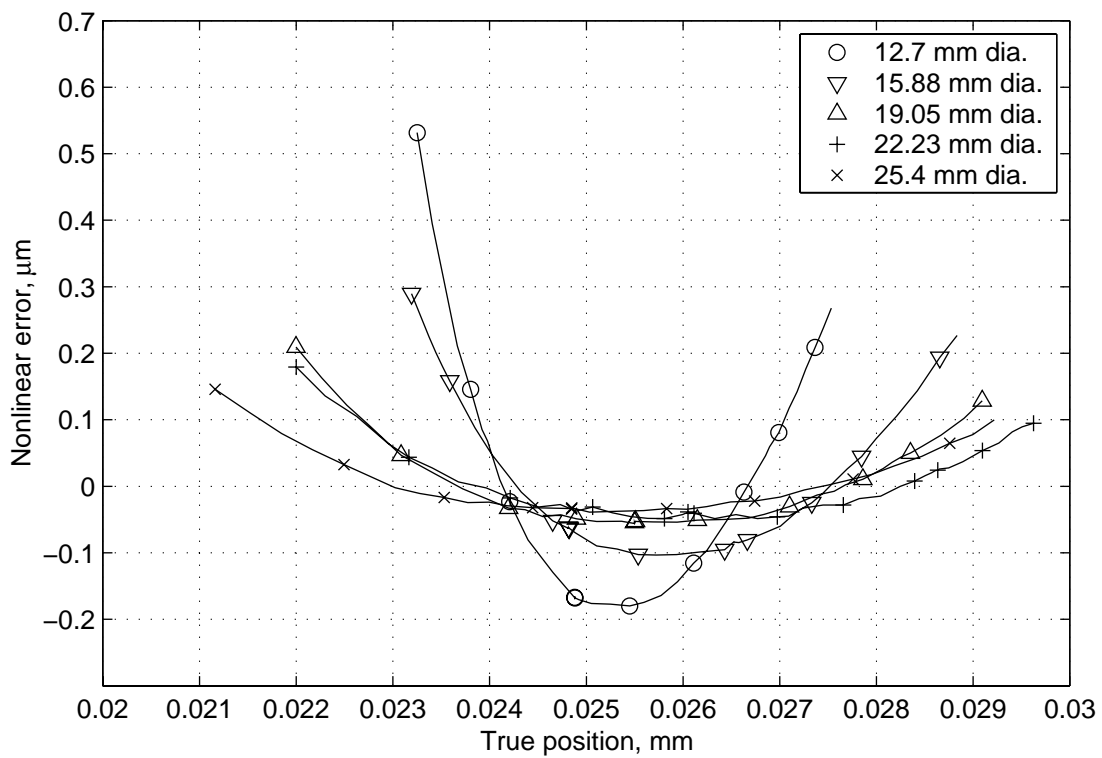
Figure 3-19. Nonlinear residue for experimental data from the ultrafine gain setting.

The final litmus test of the theoretical calculations is to apply the nonlinear third order curve to correct a set of measurements and compare them to a reference measurement. Fortunately, such a data set has been provided by Lion Precision [27]. The first four columns of Table 3-7 list the data from the Lion Precision calibration report, which is typically presented in English units. Since this data is calibrated with a 12.7 mm (0.5 inch) sphere as a reference surface, the calculated error is much larger than the values shown in Table 3-1, which is from a flat reference surface. The total range of these error values over the active range of the device is 6.86 μm (270 μinch). Column 5 of Table 3-7 presents corrected distance values based on the output voltage from column 2 and the theoretical lookup table graphically presented in Figure 3-13. This corrected data shows an error range of 0.386 μm (15.2 μinch), a 94 % improvement in linearity. Subtracting this error and plotting the nonlinearity before and after this correction, we arrive at Figure 3-20. Complete values before and after correction are listed in Table 3-8.
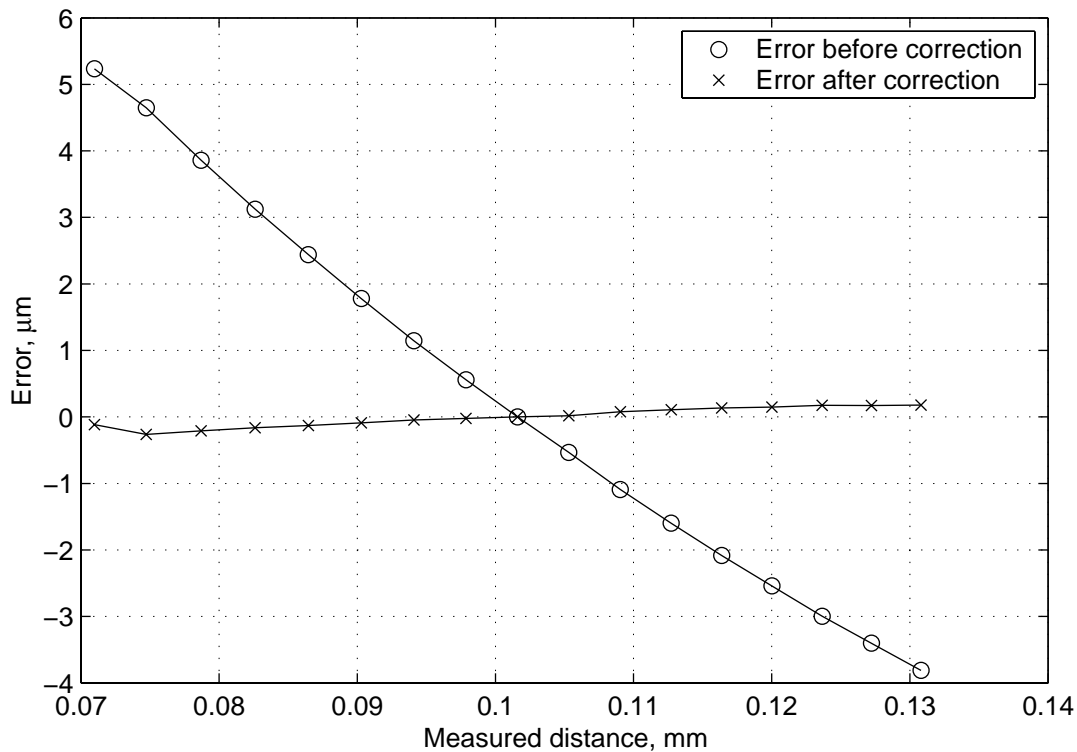
Figure 3-20. Empirical nonlinearity before and after theoretical corrections are applied.

Table 3-7. Calibration report data from Lion Precision plus corrected distances.

Gap	Output	Output converted to	Error	Corrected Value
milliinches	Volts	milliinches	milliinches	milliinches
1.465	12.061	1.259	-0.206	1.4604
1.590	10.582	1.407	-0.183	1.5796
1.715	9.019	1.563	-0.152	1.7067
1.840	7.478	1.717	-0.123	1.8335
1.965	5.958	1.869	-0.096	1.9599
2.090	4.452	2.020	-0.070	2.0864
2.215	2.954	2.170	-0.045	2.2132
2.340	1.470	2.318	-0.022	2.3391
2.465	0.000	2.465	0.000	2.4650
2.590	-1.465	2.611	0.021	2.5908
2.715	-2.926	2.758	0.043	2.7181
2.840	-4.376	2.903	0.063	2.8443
2.965	-5.818	3.047	0.082	2.9703
3.090	-7.252	3.190	0.100	3.0958
3.215	-8.675	3.333	0.118	3.2219
3.340	-10.091	3.474	0.134	3.3467
3.465	-11.496	3.615	0.150	3.4720

Table 3-8. Total error ranges before and after correction equation is applied.

Diameter	Gain, V/minch	Raw error	Average offset	Corrected error
12.7 mm (0.500 in)	394 V/mm (10.0 V/minch)	6.858 μm (270.0 μinch)	-1.382 μm (-54.4 μinch)	0.386 μm (15.2 μinch)
12.7 mm (0.500 in)	1969 V/mm (50.0 V/minch)	4.343 μm (171.0 μinch)	-1.501 μm (-59.1 μinch)	0.2997 μm (11.8 μinch)
25.4 mm (1.000 in)	394 V/mm (10.0 V/minch)	4.064 μm (160.0 μinch)	3.045 μm (119.9 μinch)	0.871 μm (34.3 μinch)
25.4 mm (1.000 in)	1969 V/mm (50.0 V/minch)	2.565 μm (101.0 μinch)	0.5004 μm (19.7 μinch)	0.6121 μm (24.1 μinch)

3.7 Conclusions

A thorough analysis of both the theoretical and experimental data has shown the importance of correcting capacitance gage measurements whenever the gage is applied to a curved surface. Otherwise the accuracy of the data, in terms of absolute distance, linearity, and gain, is called into question. As expected the problem is most severe with the smallest target spheres, approaching the flat surface values as the diameter increases.

Eventually it may be possible to develop a set of general, nondimensionalized equations or curves that represent the changes in slope as a function of gap, capacitance gage diameter, and surface curvature. In the interim, empirical measurements such as a "null" experiment of a particular surface can be used to create a lookup table of correction values.

4:
Overcoming the Limits on the
Sensing Range of a Capacitance Gage

4.1 Introduction

Although capacitive displacement sensors offer several advantageous properties, these do not come without a penalty. Their high sensitivity translates into a very small active range of sensing. For many applications where non-contact sensing is either desirable or required, the full range of the capacitive sensor, even at the lowest gain setting, may be insufficient.

One such application for the capacitive displacement sensor is in the area of large format optics. Surface measurements are taken by moving either the displacement sensor or the optic. Although it is expected that an optical surface should be good to within a fraction of the wavelength of light, it is important to remember that the ideal optical form is in most cases not spherical. A large optic will deviate significantly from a true sphere over its entire surface. Since the capacitance gage is only able to measure relative position changes, the entire surface of interest must be within the active range of the sensor. Such an application will be discussed in detail in Chapter 5.

To allow the use of capacitive displacement sensors in an application that requires long travel displacements (0.5 mm or more), the capacitive sensor must be mounted to a stage that will provide the necessary travel. Once this additional degree of freedom is added, displacement measurements become the sum of the displacement sensed by the capacitive gage and the displacement of the supporting stage. Measurement of the displacement of the supporting stage should be comparable in resolution to that of the capacitance gage, and can be accomplished using an interferometer arrangement. Light from the laser is reflected from a retroreflector attached to the moving stage, and this light interferes with light from a reference channel. Once again this is a displacement measurement (no absolute position is possible) but the travel can easily be several cm or more. This application of an interferometer is also discussed in Chapter 5.

Although it would seem that the interferometer could make an accurate measurement of the surface without need for the capacitance gage, the capacitance gage adds robustness to the system in two ways. First, the interferometer requires a highly polished, parallel mirror surface to accurately display an interference pattern. A less-than-perfect surface becomes problematic for the interferometer, and it is precisely this type of surface that needs to be evaluated. Also, since the interferometer is a displacement sensor only, if the laser signal is lost during the measurement then the reference distance is also lost. Finally, the capacitance gage provides averaging over a small surface area, automatically removing smaller surface features so that form errors can be analyzed. A similar measurement using an interferometer would require thousands of times more data points that would then be averaged in postprocessing to produce the same results.

This chapter describes an experimentally verified control scheme between a linear air bearing stage and a capacitive displacement sensor. A linear air bearing stage was chosen because of its low friction and the near-absence of parasitic motions. The linear stage is moved by a voicecoil, which allows for complete electronic control without the resolution limits inherent in a stepper motor. The entire open loop system can therefore be modeled completely in the analog domain.
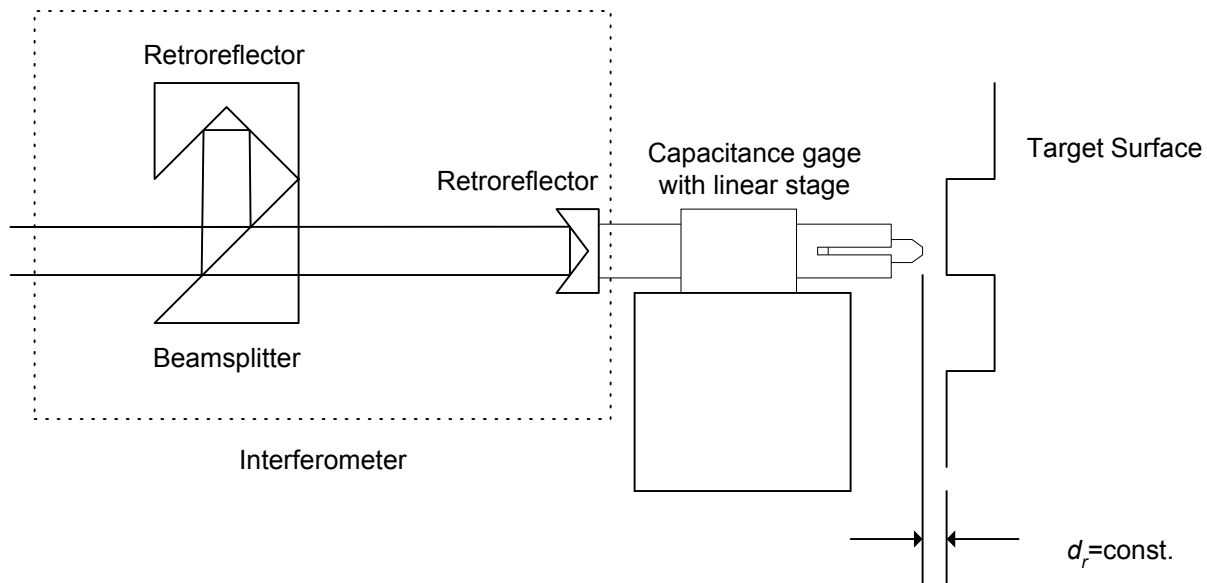
**Figure 4-1. Complete measurement configuration,
including interferometer and capacitance gage.**

The system is designed to maintain a constant distance between the capacitance gage and the mirror surface, which is preferable for two reasons. First, by maintaining a constant distance from the surface, the output of the capacitance gage need not be added to the output of the interferometer. As long as the capacitance gage distance remains constant, the displacement output of the interferometer is all that is needed to determine the form of the surface. The second reason for maintaining a constant distance has been illustrated already in Chapter 3. Specifically, for different curvatures of surface both the nominal distance (distance that produces 0 V) and the gain are affected. By positioning the capacitance gage at the nominal distance, the gain factor is removed from consideration. This system arrangement is presented in Figure 4-1.

4.2 Open Loop Transfer Function

For the purposes of experimentally testing the viability of a control scheme, an open-loop electromechanical system was assembled from available components in the Precision Systems Laboratory of the University of Kentucky. A frequency domain model of the system is then built by two methods: first by measuring the gains of the individual components of the system, then by analyzing the frequency response of the entire open-loop system and constructing a Bode plot.

4.2.1 System overview

The open loop control system consists of a linear air bearing stage and voicecoil (Systems Magnetic Company model ADE231581), a capacitance sensor (Lion Precision model C1-C), a power amplifier (Kepco Trans-Conductance Amplifier), and a moveable aluminum target. A line drawing showing the mechanical connections appears in Figure 4-2, including the voicecoil, linear air bearing, capacitance gage, and moveable target. The electrical connections, including the amplifier, voicecoil, and capacitance gage, are shown in Figure 4-3. The equipment as assembled on the optical table in the laboratory is pictured in Figure 4-4.

Additional equipment required by the system includes a source of pressurized dry air and an electronics box for the capacitance sensor (Lion Precision model DMT22, not shown in photograph). Measurements are made using a DMM, a signal analyzer (Agilent Dynamic Signal Analyzer model 35670A), and a PC with A/D capabilities. The latter allows multiple voltage sources to be recorded simultaneously for postprocessing.

The system begins with the input at the left of the system and with subsequent signals moving to the right. The input signal, a voltage, is applied to the front panel of the power

amplifier. This power amplifier is configured to provide an output current that is linear with the input voltage. The output of the amplifier is wired directly to the cylindrical voicecoil. The voicecoil is designed to provide a force on its ferromagnetic "rotor" that is linear with the input current. The rotor of the voicecoil is attached to the "rotor" or moving element of the linear air bearing, which is composed of hardened aluminum with a square cross section. Dry air at 30 psi is applied to the bearing, producing an almost frictionless, floating mass. With the exception of the cable for the capacitance gage, the moving components of the system are entirely supported by the pressurized air of the air bearing.
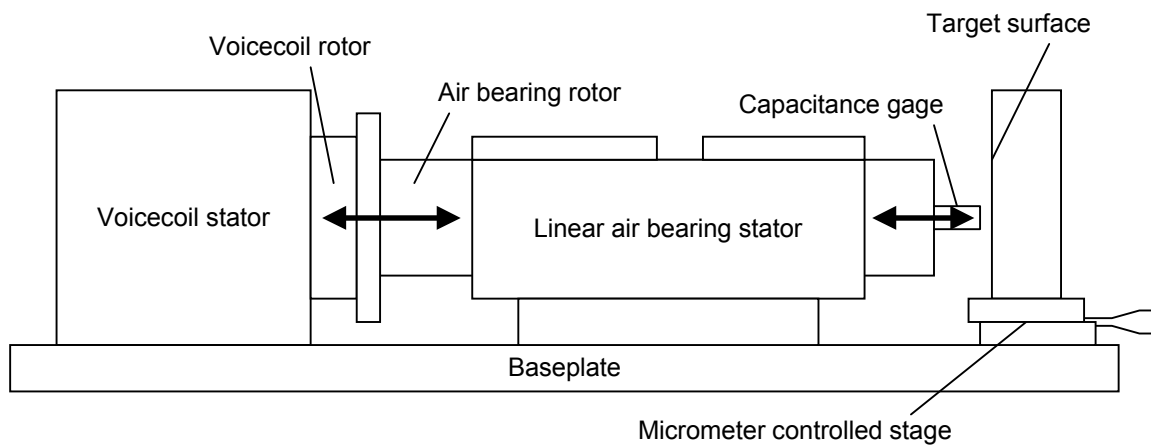
Figure 4-2. Drawing of mechanical components of test system.
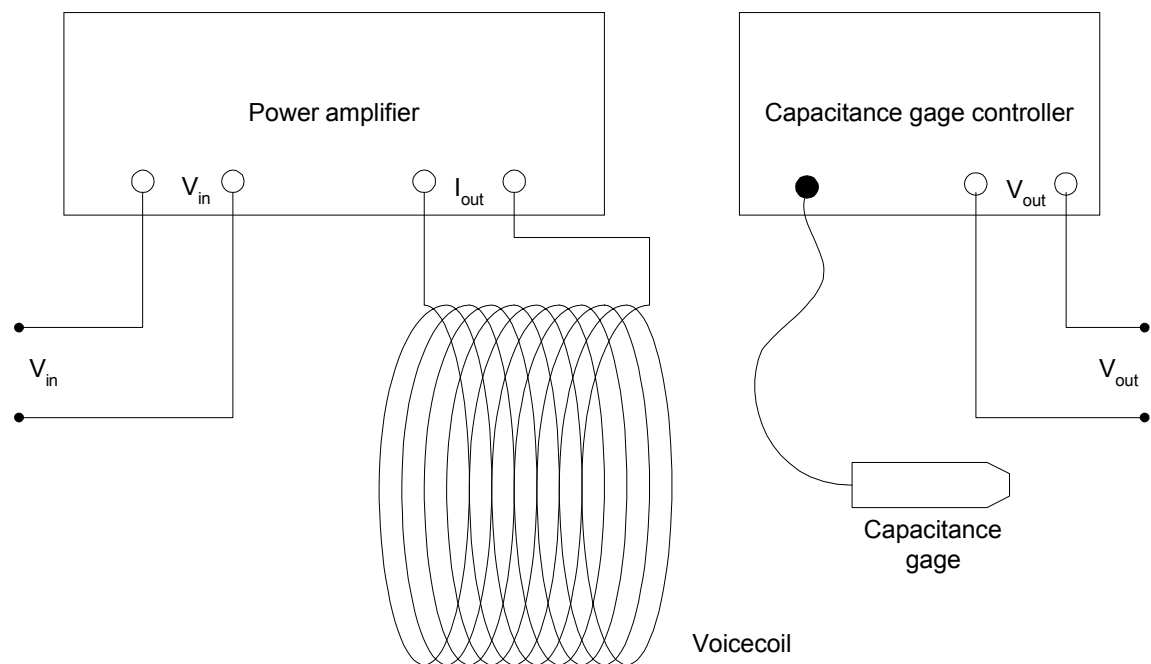
Figure 4-3. Drawing of electrical connections in open-loop test system.

Attached to the rightmost end of the linear air bearing rotor is a small, 9.5 mm (0.375 inch) diameter capacitance displacement sensor. A target surface is mounted to the fixed table by means of a micrometer-controlled stage. The target surface can therefore be moved in controlled increments as needed, with the capacitance gage sensing displacements. The electronics box converts the capacitance into a voltage from –10 V to +10 V that is linear with displacement. The calibrated gain of this capacitance gage is 78.7 V/mm (2 V/minch) at the lowest gain setting, with a nominal offset of 0.254 mm. Having both the input and output of the system in the common units of Volts allows both for ease in measuring and comparing these two signals, as well as for closing the control loop.
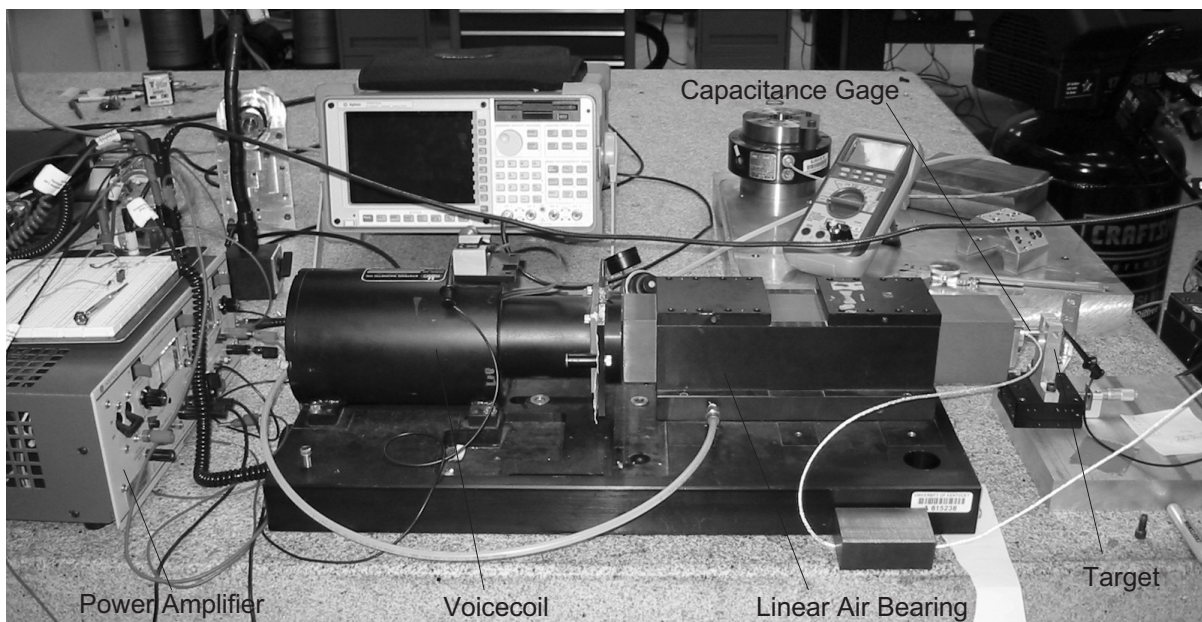
Figure 4-4. Complete test control system with key components labeled.

To measure the input and output voltages of this system an acquisition card (DAQ) in a Pentium computer is capable of digitizing, displaying, and recording both signals. Although this DAQ is not able to provide an analog output of the form that will eventually be needed to close the feedback loop, it is useful for testing and recording experimental data.

4.2.2 Component model and measurements

One technique for building a model of the entire system is to start with a model of each individual component, then determine how they are interconnected. A diagram of the individual components and their connections appears in Figure 4-5. The *G* variables indicate the gains of

the power amplifier, voicecoil, and capacitance displacement sensor. The *m* variable is the mass of the entire moving section, including voicecoil rotor and air bearing rotor. The *s* variable is for frequency, and the *c* constant is a term to represent the small damping inherent in the bearing.
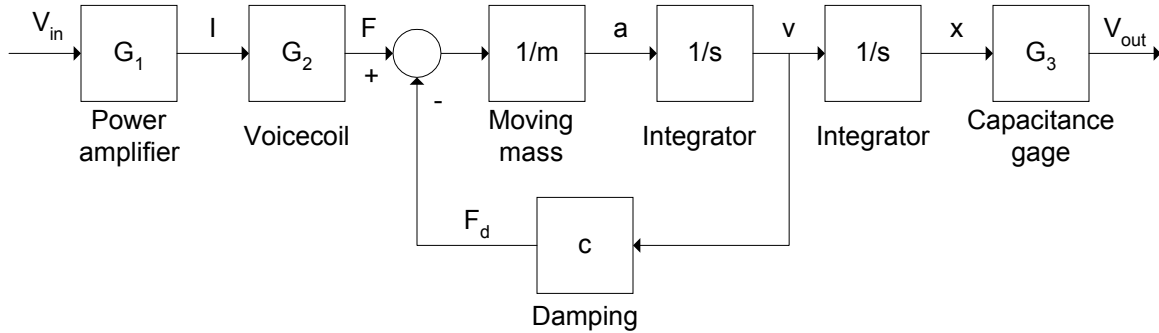
Figure 4-5. Block diagram of the complete analog system.

Per the specifications of the power supply, voicecoil, and capacitance gage, all of these gains are constants, independent of frequency. From this "bottoms up" piecewise approach, the model of the entire system is represented by Eq. (4-1).

$$G(s) = G_1 G_2 \frac{1}{m} \frac{1}{s} \frac{1}{(s + c/m)} G_3 \qquad \textbf{(4-1)}$$

Most of these individual gain terms can be readily determined by simple experimentation. The gain G_1 of the trans-conductance amplifier is determined by measuring the voltage drop across a known resistor as a function of input voltage, as shown in Figure 4-6. The resistor is several orders of magnitude lower than the DMM pictured so the DMM resistance can be ignored. Several points are measured and averaged, with a resulting value for G_1 of 0.6066 A/V.

When this gain is applied to the input voltage V_{in}, the resulting output is in units of mA as expected. The next two terms in Eq. (4-1), G_2 and *m*, are determined as follows. First, the mass of the moving components is measured using a laboratory scale. Then the linear air bearing is positioned at a known angle using gage blocks. Sufficient current is applied to the voicecoil to prevent the rotors from moving due to gravity. The solution to the force provided by the voicecoil is given by Eq. (4-2). The experimental setup is presented in Figure 4-7.

$$F = mg \sin\left(\arctan\frac{h}{l}\right) \qquad \textbf{(4-2)}$$
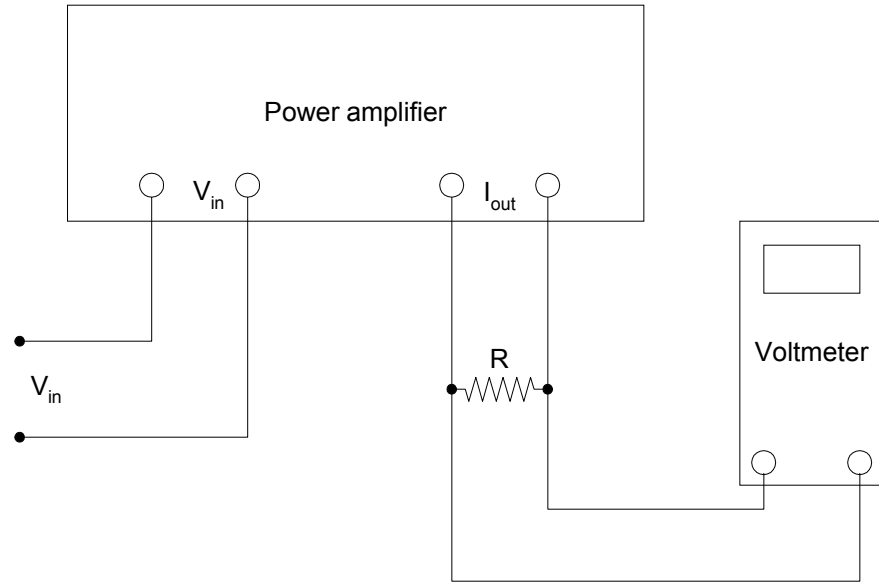
Figure 4-6. Experimental setup to determine gain of power amplifier.

The mass m is measured to be 4.3 kg, and current and geometry measurements produce a gain G_2 of 28.076 N/A. An input value in amps results in an output value of Newtons.

An additional force term occurs due to friction in the air bearing, and it is modeled as being proportional to the velocity of the air bearing rotor. Thus after dividing by mass and applying one integration, the velocity feedback is summed together with the force provided by the voicecoil. An additional integration to the velocity term produces displacement x.
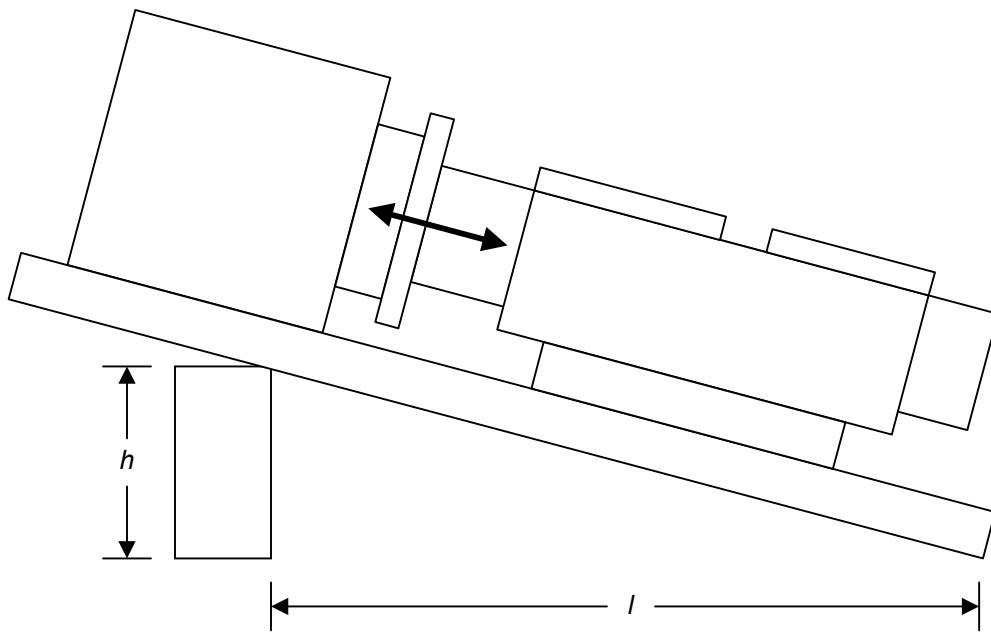
Figure 4-7. Experimental setup to determine force provided by the voicecoil.

Moving to the final gain G_3, this is recognized as the calibrated gain of the capacitance displacement sensor, which has already been given as 78.74 V/mm. Since the target surface in this experiment is flat and parallel, no additional corrections to this gain are necessary.

At the end of these static measurements, the only remaining unknown in the system is the damping term c. Since coulomb damping by its nature requires a dynamic experiment, no determination of this term is possible statically. An experiment with calibrated springs and an accelerometer could have been used to determine this last unknown, but an even more straightforward, "top-down" approach was applied instead as described in detail in Section 4.3. Combining the known terms from the static experiment, the system model to this point is as shown in Eq. (4-3).

$$G(s) = \frac{310,000}{s(s + c/m)} \qquad \textbf{(4-3)}$$

4.2.3 Frequency analysis of open-loop system

A second approach to modeling the system is a "top down" approach, considering the functioning of the system as a whole, rather than separating out individual components for scrutiny. Looking at the form of Eq. (4-1), it is apparent that this is a model of a second order, damped oscillator.

The assumption that a system is of second order (or at least can be approximated by one) implies that there are two dominant poles near the $j\omega$ axis, much closer than any other poles or zeros. A pure second order damped system is a Type 1 system, meaning that a step input can be tracked with zero error, and that a ramp input can be tracked with finite error. In the Bode diagram of such a system the phase approaches but never crosses -180 degrees so the gain margin is infinite. On the root locus the two lines depart at an angle of 90 degrees from the location $-\zeta\omega_n$ on the real axis, and never cross the $j\omega$ axis.

Before the open-loop system is analyzed, it is clear from the component modeling and early testing that the system has an extremely large gain. Prior to frequency tests, an analog voltage divider of value K was added to the input of the system, as shown in the modified block diagram of Figure 4-8. This resistor bridge can be considered as a filter of constant gain, with an

initial value based on voltage ratios of K_I=0.01068. The modified transfer function is shown in Eq. (4-4).
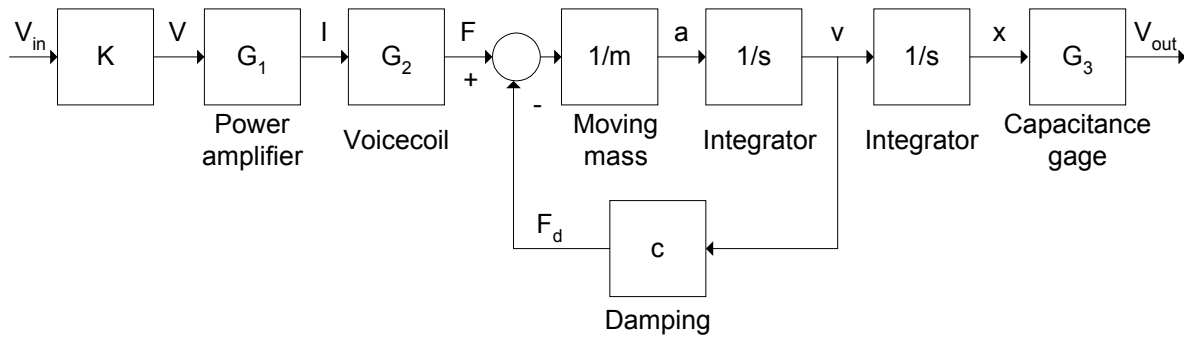
Figure 4-8. Modified block diagram of the complete analog system, including attenuator.

$$G(s) = KG_1G_2 \frac{1}{m} \frac{1}{s} \frac{1}{(s + c/m)} G_3 \qquad \textbf{(4-4)}$$

The next step in determining the system response is to employ a signal analyzer to measure both amplitude and phase response of the open loop system. The Agilent Model 35670A Dynamic Signal Analyzer had the necessary flexibility to test the system. Experiment parameters required by the signal analyzer include the start and stop frequency (in Hz), output amplitude (in mV), and the form of the frequency input (swept sine wave). Selection of the appropriate start and stop frequencies requires some knowledge of the approximate gain at the starting or stopping frequency. Throughout the testing the system must be monitored to prevent the output from exceeding the input limits of the signal analyzer (-5 to +5 V).

To connect the signal analyzer to the system the voltage output of the signal analyzer is connected to V_{in} of the system, and the output of the system V_{out} is connected to the voltage input of the signal analyzer. For each experiment, only one decade of response could be measured at a time, before it became necessary to modify the output amplitude. Also, due to the long settling time for low frequencies (many seconds), the system must be monitored to prevent the stator from drifting out of range of the capacitance gage. This unwanted motion occurs because the damping of the system is extremely low. Small forces on the cabling or any slight tilt of the air bearing can both cause the rotor to drift left or right. Since the active travel range of the capacitance gage is limited, even the smallest movements may result in off-scale voltages.
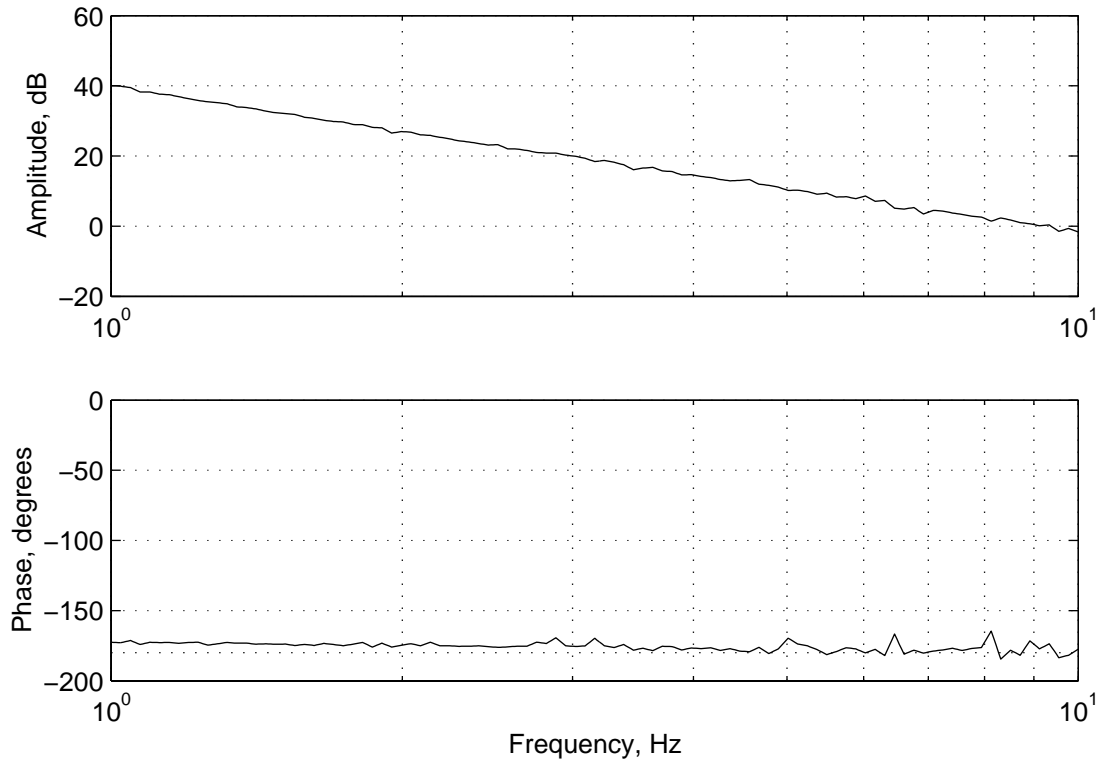
Figure 4-9. Amplitude and phase response from 1 Hz to 10 Hz.

One decade of data is shown in the Bode plot of Figure 4-9. In this figure, the first complete decade of data collected, the phase has approached approximately –180 degrees, and the amplitude is clearly and precisely falling at 40 dB per decade. This would confirm that the system is second order, validating our use of the damped oscillator model in Eq. (4-5). This decrease in response indicates that both break points occur long before this frequency range. For this system, 1 Hz is considered a "high frequency."

Several difficulties arose while attempting lower frequency tests. Sweeping of the sine wave from highest frequency to lowest frequency helped stabilize the system through part of a decade. Determining an appropriate starting amplitude became quite difficult, since the gain of the system was ever-increasing. Ultimately, the drifting of the air bearing at the lowest frequencies prevented the collection and analysis of additional Bode plots.

4.3 Closed Loop Response Testing

The first closed-loop test of the system was to simply close the loop with a wire, inverting the output of the capacitance gage (V_{out}) and applying it to the input of the power supply (V_{in}). The results were quite dramatic and somewhat destructive: the motion of the stage

was so great that the capacitance gage immediately exceeded its linear output range (-10 V to +10 V). This high voltage provided such a large force to the voicecoil that the capacitance gage was driven into the target flat plane, knocking it to the floor. Subsequent tests with added damping indicated that the closed-loop system was either unstable or marginally stable.

Since the large forces involved are clearly the result of an exceedingly large gain, it was decided to include a potentiometer in the voltage divider circuit, by which means the gain K in Eq. (4-4) could be varied easily. Two attenuator circuits applied at different times are sketched in Figure 4-10.

As discussed in Section 4.2.3, the system described by Eq. (4-4) is a second order, damped oscillator. The more familiar form of the damped oscillator equation is to write it in terms of two variables, a natural frequency ω_n and a damping coefficient ζ. The open loop formulation is shown in Eq. (4-5), and the closed loop formulation in Eq. (4-6). The task at hand is to determine the two unknowns ω_n and ζ.

$$G(s) = \frac{\omega_n^2}{s(s + 2\zeta\omega_n)} \tag{4-5}$$

$$\frac{G(s)}{1 + G(s)} = \frac{\omega_n^2}{s^2 + 2\zeta\omega_n s + \omega_n^2} \tag{4-6}$$

This variable attenuation, K_v, becomes a method by which a series of measurements of the closed loop system can be made. For each attenuation value K_v a different natural frequency and damping coefficient are determined, but from these a common value for the numerator and the c/m term in Eq. (4-3) can be derived.
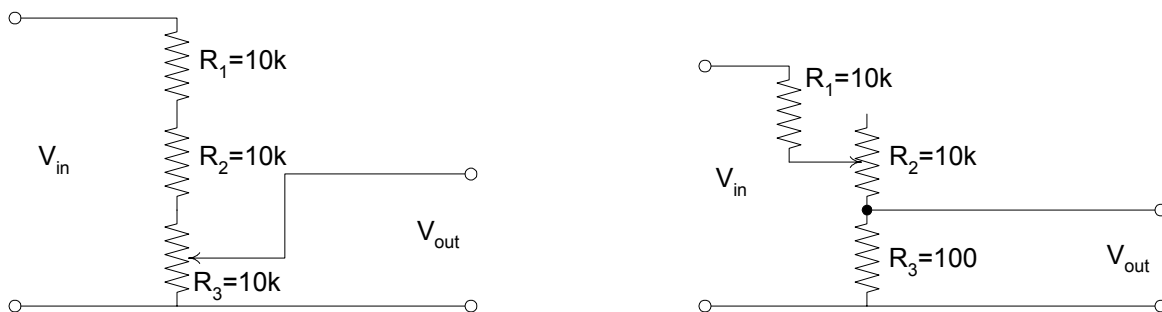
Figure 4-10. Two attenuator circuits applied to the input of the system.

Once a gain is applied and the loop closed, the damped, oscillatory response of the system can be recorded and analyzed. One such plot of oscillatory response is shown in Figure 4-11. From these plots it is possible to determine the frequency of the damped oscillations ω_d and an attenuation factor δ.
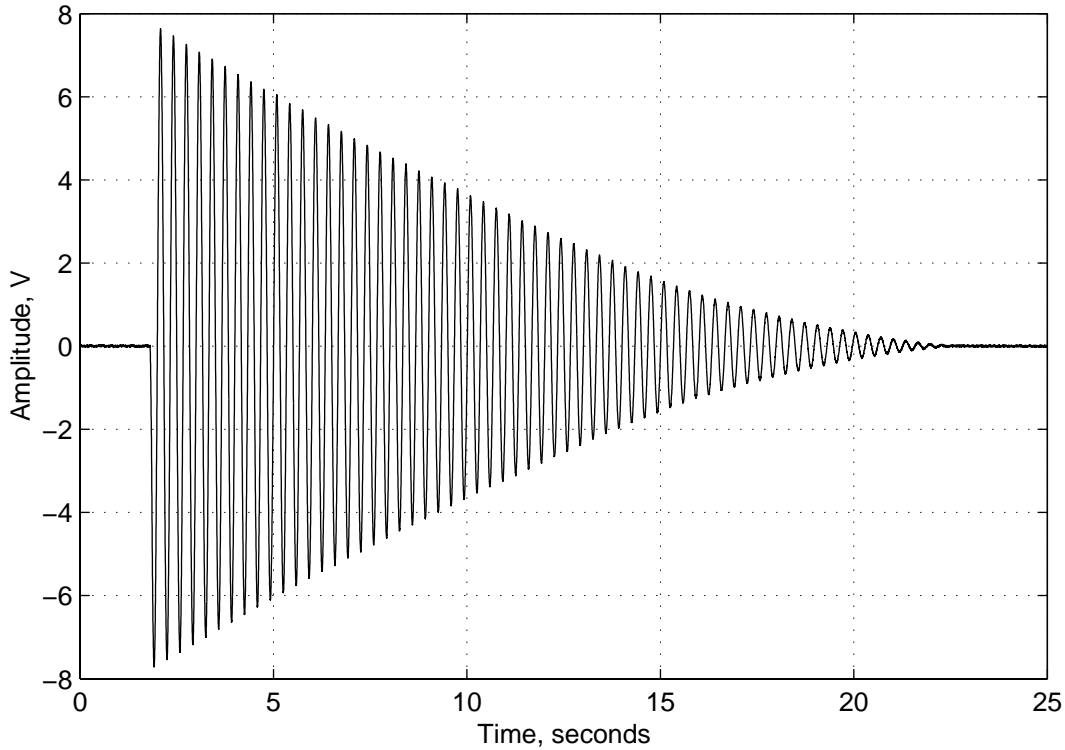
Figure 4-11. Oscillatory response of closed loop system with simple attenuator K.

Values of ω_d and δ were collected for three different gain settings of the variable gain K_v. To determine values of the desired variables ω_n and ζ an approximation must first be made for the natural frequency, namely that for lightly damped systems $\omega_n \approx \omega_d$. With this in place, the damping coefficient can be determined from Eq. (4-7) [28]. This equation compares the amplitude of the oscillations at an initial point (x_0) to the magnitude after n oscillations (x_n) where n is arbitrary.

$$\delta = \frac{1}{n} \ln \frac{x_0}{x_n} \approx 2\pi\zeta \qquad \textbf{(4-7)}$$

84

Although the values of ω_n and ζ are different each time, it is possible to factor out the attenuation K_v and determine the numerator and c/m term for the system model $G(s)$, which should remain constant. Table 4-1 shows the values obtained by these three measurements.

Table 4-1. Closed loop values obtained from varying analog gain.

K_v	ζ	ω_n	c/m	numerator
5.99e-4	1.58e-2	13.607	0.431	3.09e5
1.164e-3	7.4e-3	18.84	0.278	3.05e5
5.06e-3	1.288e-3	38.73	0.09977	2.96e5

The results in Table 4-1 show consistency in the numerator of the open-loop system, but some discrepancies in the location of the pole in the left hand plane (column 4). This would indicate that the system under study is not entirely a true second order system, but rather there are one or more additional poles somewhere in the left hand plane. Since the Bode plot in Figure 4-9 shows the amplitude decreasing at 40 dB/decade, any additional poles to the system must lie far in the left-hand plane (at much higher frequencies). For this reason, the model can still be considered a second order system, although the presence of an additional pole must be considered when analyzing the data in Table 4-1.

The clearest way to analyze this data is by plotting the closed loop points on a root locus diagram. The data points are shown in Figure 4-12, along with points that extrapolate the open loop poles on the real axis. Given a smaller and smaller gain, the root locus should intersect at the real axis and approach the open loop poles. The apparent bending of the root locus toward the $j\omega$ axis as the gain is increased is consistent with a pole in the far left hand plane, and this is also consistent with the fact that the closed loop system with no gain reduction was either unstable or marginally stable. From this diagram an intersection point with the real axis is approximated to be at $s = -0.275$, indicating that the open loop poles based on the second order system model are at 0 and -0.55 rad/s. With this and the average value of the numerator from Table 4-1, the system model can now be fully described as shown in Eq. (4-8).

$$G(s) = \frac{303,000}{s(s+0.55)} \qquad \textbf{(4-8)}$$

Since this is an incredibly large gain, it is likely that a digital feedback system might have difficulty providing small enough voltages without quantization errors. One bit on a 16 bit A/D

that is capable of a −10 V to +10 V range is 0.3 mV, but this system might require input voltages comparable to this size. To reduce the gain of the system to a reasonable level, a 1000:1 analog voltage divider K was applied to the input of the system, with the result that the final system model became as shown in Eq. (4-9). This is the system model used for development of both the digital and analog controllers.

$$KG(s) = \frac{303}{s(s + 0.55)}$$ **(4-9)**
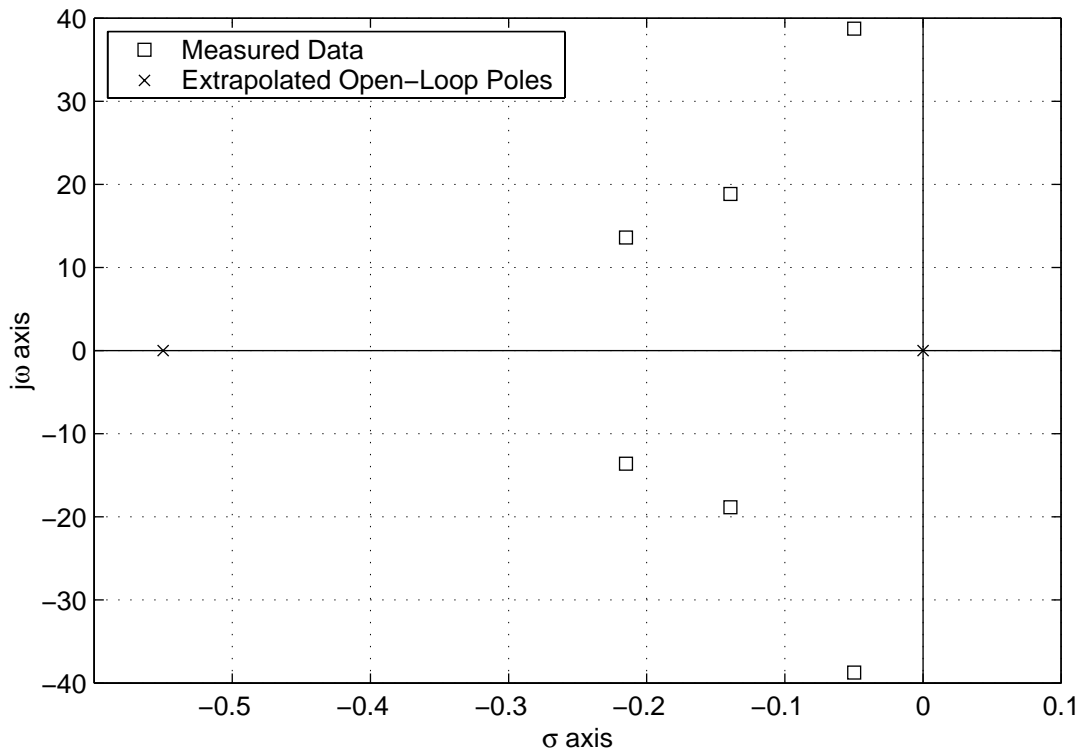
Figure 4-12. Closed loop points plotted on a root locus diagram. This includes both data from Table 1 and extrapolated values.

4.4 Closed Loop Control

Once the system model in Eq. (4-9) has been determined, the controller can be designed. The purpose of this controller is to maintain a constant distance from the target surface, therefore the system can be considered to be tracking a voltage of 0 V. As the target surface moves past the capacitance gage, it is important to determine how quickly the capacitance gage can follow the surface, a function of the settling time.

For simplicity of application and ease of modification, a digital controller was temporarily applied to control the system. Once the design of the digital controller is finalized and its performance confirmed, for cost reasons an analog circuit with equivalent performance is to be applied in its place. For this reason the design process occurs in the *s* domain before being converted to the *z* domain.

4.4.1 Digital filter designs

The first step in the design of a digital controller for the air bearing system is to determine the sampling rate of the digital controller. The digital control system utilized for this testing is an Allen-Bradley Small Logic Controller (SLC). The rack-based controller consists of a processor, power supply, and a single analog input-output card. This card has the ability to process two analog inputs and two analog outputs with 16 bit digitization over the range from −10 V to +10 V.

The sampling time T_s of the digital controller is 10 msec. The analysis of the second order system model has shown that this sampling time is well beyond the Nyquist limit for the natural frequencies of the final attenuated system modeled in Eq. (4-9), which has an $\omega_n = 17.4$ rad/s. The zero-order-hold term for this sampling time, which must be applied to the system model, is shown in Eq. (4-10). The complete system model to be compensated is shown in Eq. (4-11). The digital compensator is designed for this system.

$$G_{ZOH}(s) = \frac{1}{(.005s + 1)} \tag{4-10}$$

$$KG_{ZOH}G(s) = \frac{303}{s(s + 0.55)(0.005s + 1)} \tag{4-11}$$

The first design of the compensator used as a design parameter desired dominant poles at −2+2*j* and −2−2*j*. This point was selected because it was thought that the large mass of the test system could be moved by a step function with a settling time of 2 seconds. The angle of 45 degrees in the complex plane was selected so that the root locus could be bent using a standard lead compensator design. This approach was favored since it is a robust and straightforward design.

The analog lead compensator $G_c(s)$ was calculated using Matlab code listed in Appendix C, with the results shown in Eq. (4-12). The bilinear transformation is applied to this to convert to the z domain, with the results shown in Eq. (4-13).

$$G_C(s) = \frac{0.5453(s + 2.2134)}{(s + 50)} \qquad \textbf{(4-12)}$$

$$G_C(z) = \frac{(0.02434z + 0.02391)}{(z + 0.9992)} \qquad \textbf{(4-13)}$$

This first compensator design is programmed into the digital controller to measure the actual performance of the complete system. To produce oscillations, the system is disturbed from equilibrium either by moving the target surface or by positioning the rotor away from equilibrium. Two plots of such measurements appear in Figure 4-13. The plot shows output voltage over time, which can be converted to position by dividing by the G_3 gain factor of the capacitance gage.
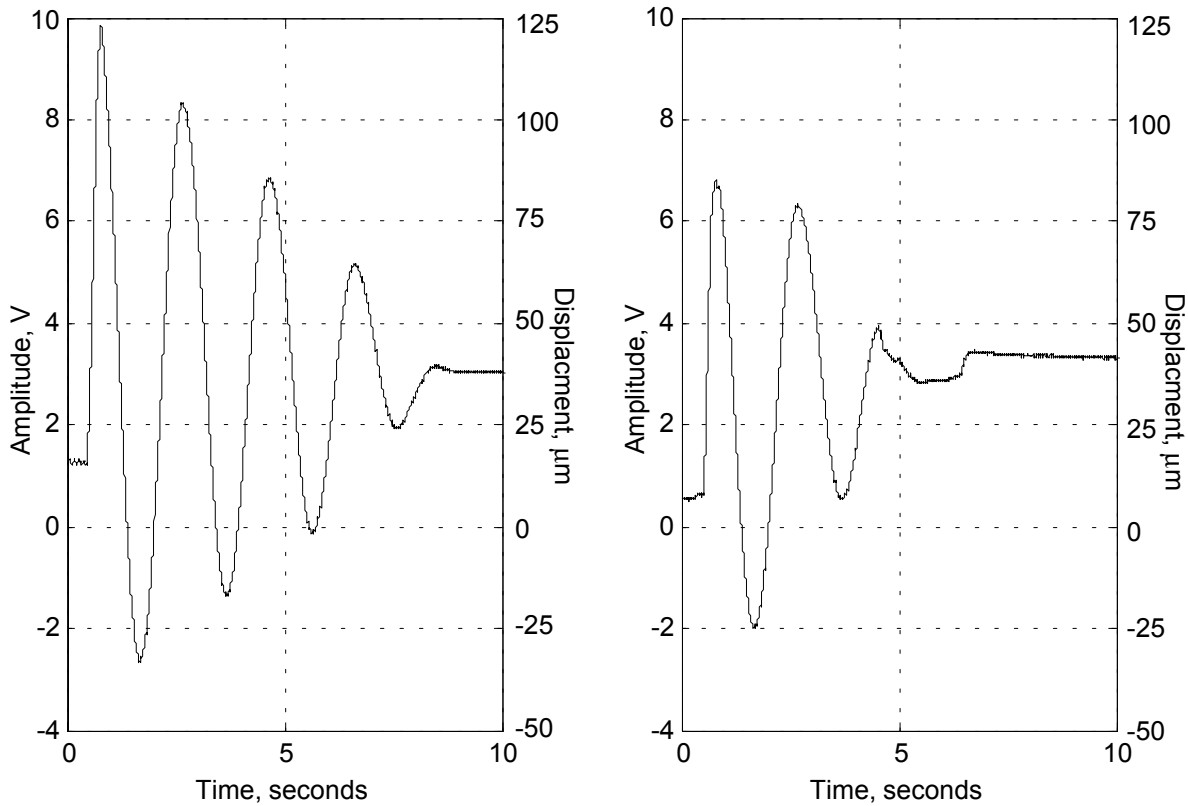
Figure 4-13. Results of the first compensator design.

88

There are several problems with this first design that must be addressed before the design is acceptable. The settling time of Figure 4-13, about 9 seconds, is much larger than the settling time of 2 seconds that is to be expected from the dominant poles of the first design. Also, as can be seen from the figure, several oscillations occur before steady state is reached. A final concern is that the system does not settle precisely to zero volts as expected, but instead reaches 3 volts in the steady state.

Both the settling time and the oscillations can be explained by considering the effect of the lead compensator design. A lead compensator is designed to "bend" the root locus such that is passes through two desired poles. The angle of deficiency is the amount of angle that is required to be added by the compensator, in this case 83.9 degrees. Such a large angle is difficult to achieve with this kind of compensator, in effect we are expecting too much for this system. It is decided, then, to pick new dominant poles and attempt a new compensator design.

The two new poles are chosen to be located at $-1+j$ and $-1-j$, which will require less "bending" of the root locus. The settling time for these points is 4 seconds, with minimal overshoot. Once again, Matlab is used to solve for the compensator in both the s (analog) and z (digital) domains. These solutions appear in Eqs. (4-14) and (4-15).

$$G_C(s) = \frac{0.2355(s+1.3504)}{(s+50)} \qquad \textbf{(4-14)}$$

$$G_C(z) = \frac{(0.00645z+0.00626)}{(z+0.9992)} \qquad \textbf{(4-15)}$$

The angle of deficiency in this case is 70.7 degrees, less than the previous solution and much more reasonable for a lead compensator to achieve. This new design is programmed into the digital controller and the system is once again disturbed from equilibrium while recording the system output voltage V_{out}. Two plots of the output appear in Figure 4-14. In both traces, the system starts out at rest but displaced from equilibrium. After one oscillation the system settles to an equilibrium position. As before, the equilibrium position is stable but zero in one instance, 3 V in the other. The settling time is less than the 4 seconds stipulated by the design, and the overshoot is minimal.

One possible cause of this nonzero steady-state is due to some slight tilt in the air bearing stage. With essentially no static friction an air bearing stage is affected by any tilt in the position

of the stage, no matter how slight. A constant force is required to maintain equilibrium, which translates into a constant but non-zero input voltage. Cabling to the capacitance gage also applies a force that must be compensated, and may vary from experiment to experiment depending on the exact starting position of the stage. Although 3 V seems like a large value, the final analog gain *K* present in the system will reduce that signal to 3 mV. The power supply may also exhibit a slight offset affecting the location of its "zero" point.
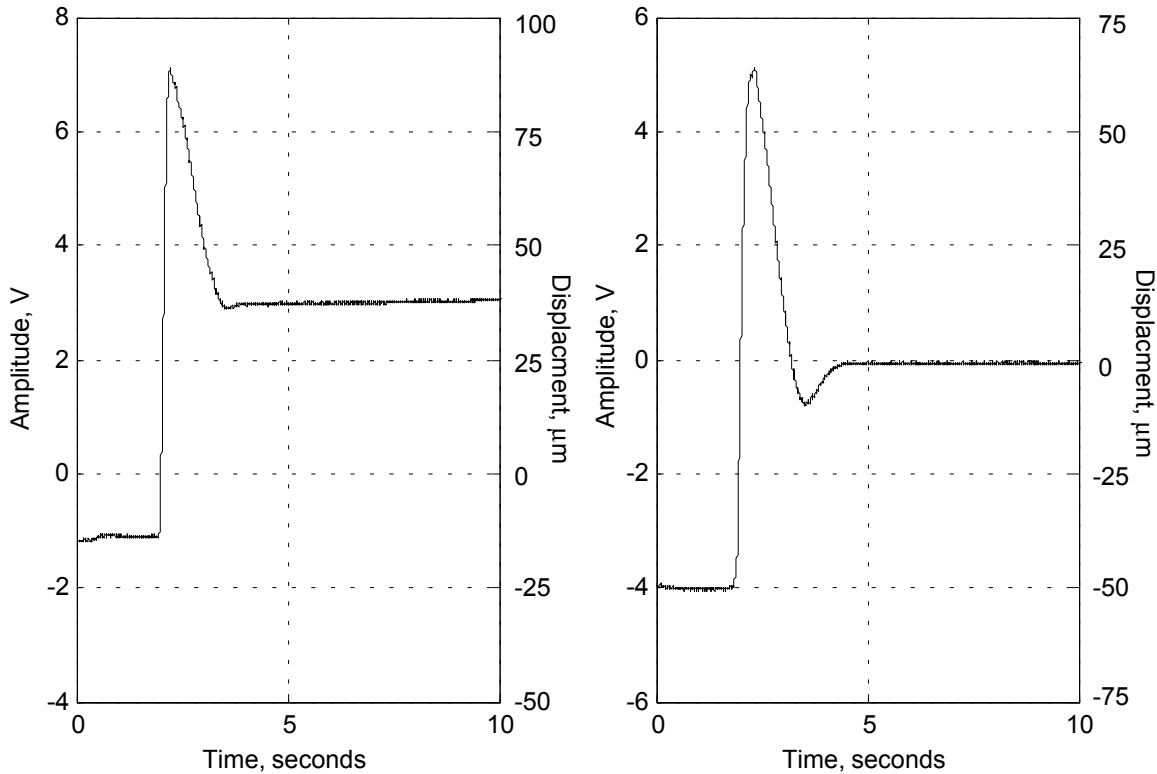
Figure 4-14. Output signal after implementation of second controller design.

4.4.2 Analog filter equivalent

After a satisfactory digital design has produced good results from the system, the next step is to build an inexpensive, analog version of this controller on a circuit board. This not only frees up the expensive digital controller for other experiments, but also makes the design both portable and easily reproducible.

In the analog domain the zero-order-hold does not exist, so the system to be modeled is simply that shown in Eq. (4-9). Choosing once again our successful design poles of $-1+j$ and $-1-j$, we utilize Matlab once again to produce the lead compensator of Eq. (4-16). This is nearly identical to the *s* domain design of the compensator shown in Eq. (4-14), indicating that the zero-

order-hold has little effect in this case. Equation (4-16) is rewritten in Eq. (4-17) to facilitate the analog design process.

$$G_C(s) = \frac{0.2363(s+1.3561)}{(s+50)} \tag{4-16}$$

$$G_C(s) = \frac{0.3205(0.7374s+1)}{50(0.02s+1)} \tag{4-17}$$

Implementing this design in the format of Eq. (4-17) with operational amplifiers is quite straightforward, involving four resistors and two capacitors as shown in Figure 4-15. Choosing straightforward values of capacitance, 3 equations and 4 unknowns allow for some flexibility in the design. The equation for determining the compensator from this diagram is as shown in Eq. (4-18).

$$G_C(s) = \frac{R_4 R_2 (R_1 C_1 s + 1)}{R_3 R_1 (R_2 C_2 s + 1)} \tag{4-18}$$
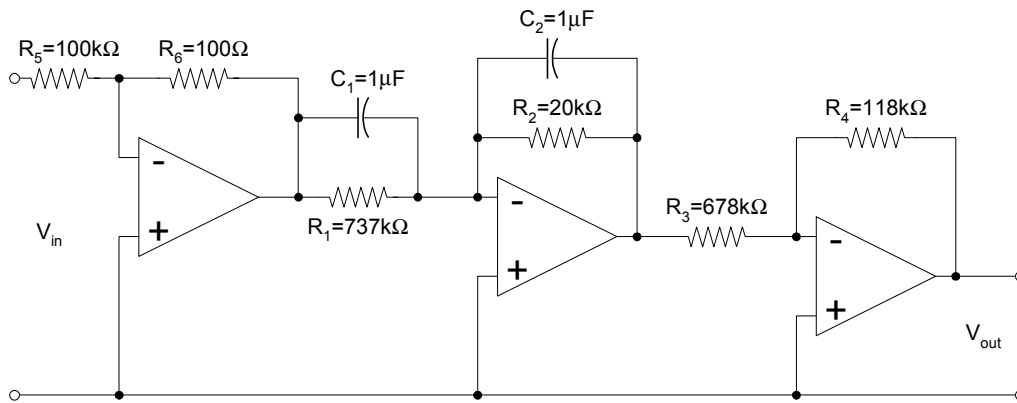
Figure 4-15. Lead compensator analog design, including 1000:1 gain reducer.

4.5 Conclusions

A capacitance sensor, while offering high sensitivity, has drawbacks in terms of active range. This limitation can be overcome by coupling the sensor with a linear stage, whose motion is measured with a displacement measuring interferometer. The signal from the capacitance gage is used in a feedback loop to maintain a constant distance from the target surface. The control circuit can be digital or analog. Such a system has been designed and tested to prove viability in the application.

91

5:
A Measurement Machine for Large Mirrors

5.1 Introduction

To this point, this thesis has studied the effects of applying capacitance sensors to various surfaces. A single application, that of making non-contact spindle measurements, has been used as justification for the detailed analysis of Chapter 2 and Chapter 3. An application that would require the extended operating range of the system described in Chapter 4 has not yet been described. This chapter will present such an application, as well as a machine that incorporates the linear air bearing system of Chapter 4.

Lightweight, large format mirrors are planned for future generations of space-based telescopes to collect the maximum amount of light from faint sources. These thin film "gossamer" mirrors are formed from a sheet of polymer and coated with aluminum or gold for maximum reflectivity. In some configurations, multiple reflectors are arranged on a frame structure that allows for dynamic focusing of the optics.

A second, less-demanding application for these mirrors is for the collection of solar radiation for powering onboard systems. In either case, accurate measurements of the form of the surface must be achieved. If the wavelength of light is in the visible region, then measurements of the surface should have an error on the order of 50 nm or less to be a useful indication of the quality of the optic.

These surface measurements can be placed into three major categories. The smallest-scale measurements (microns) are of surface roughness, while waviness measurements are of features up to approximately 1 mm in size. The largest features are categorized as form, or how closely the entire surface conforms to a desired shape. For roughness and waviness measurements, a small area of the mirror can be removed and examined using traditional techniques such as surface profilometry. For form measurements a machine must be able to achieve displacement measurements across the entire surface without damaging or deforming the flexible surface of the mirror.

In this chapter two machine designs are compared and contrasted to determine which machine offers the maximum accuracy, while allowing sufficient flexibility for measuring a variety of mirror surfaces and curvatures. Both proposed machines would use a capacitive sensor in combination with a linear air bearing and a laser interferometer to serially measure as many surface points as needed. The mirror is supported along its entire circumference by a "nest" structure to minimize deformations due to induced strains. The design details of these two "mirror metrology machines" are compared and contrasted.

The first instrument design considered for this measurement uses a "pendulum" geometry, with a radial arm pivoted at the nominal center of the mirror. The mirror nest is supported by a spindle that allows rotation around a vertical axis. The pendulum pivots on a second, horizontal axis to sweep across the surface of the mirror. The light path for the interferometer travels along the horizontal axis of the upper spindle, then is reflected downward to the back side of the capacitance sensor. For a perfectly spherical mirror with the upper axis of rotation intersecting the center of the mirror, the variation in radius and the tilt of the surface are both zero.

The second design considered for this machine uses a "swingarm" to traverse the surface of the mirror. As in the first machine, the mirror nest is mounted horizontally on a rotating spindle. For optimal operation of the machine the angle of the tilted axis of the swingarm is set such that the vertical axis of the mirror intersects the tilted axis of the swingarm at the nominal center of the mirror. Once again, for a spherical mirror properly aligned the variation in radius is zero. Central to this design is its ability to measure a wide variety of curvatures, including very large radii (many meters in length).

5.2 Mirror Dimensions

For gossamer optics the mirror dimension is usually limited by one of two factors. The first is the constraints placed upon the optics by the size of the optical structure at launch. For this reason it is often desirable for the optic to be rolled or folded during launch, to be unfurled along with the supporting structure once the spacecraft is in orbit. The second size constraint placed on the optic is due to the availability and quality of formed polymer sheets. Larger size sheets typically have more variability in thickness, which may translate into form errors once the mirror has been shaped.

The target mirror dimensions for this application are shown in Figure 5-1. The surface has a radius of curvature of 100 cm and a diameter (circumference/pi) of 80 cm. A flat edge of 2.5 cm is desired for mounting purposes. Also as part of the mount, precision holes may be positioned at regular intervals along this edge.
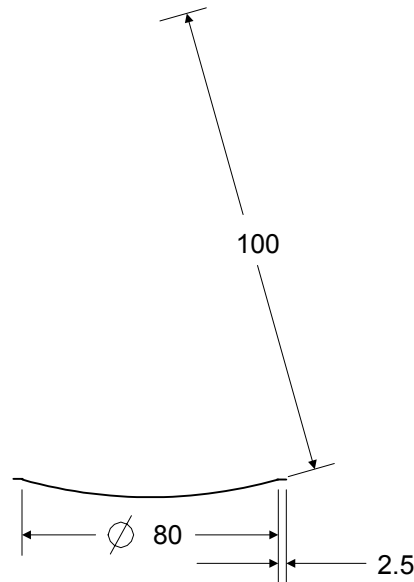
Figure 5-1. Initial target values for mirror dimensions, in mm

5.3 Overview of Prior Measurement Techniques

At least three categories of measurement techniques have been applied to large format mirrors in past applications. These include 2D profilometry, phase shift interferometry, and non-contact laser profiling. All three of these methods have been rejected as possibilities due to their limitations when applied to gossamer optics.

5.3.1 2D profilometry methods

One method of surface evaluation is to use contact profilometry to measure multiple points on an arc [29]. A pivoting arm is designed to trace a circular arc, and a gage measures deviation in radius from sphericity. To access all points on the surface, a second rotational axis is required, either to rotate the measurement structure over the mirror surface, or to rotate the mirror surface under the measurement structure.

This method is one of the simplest, and is often used as a rough guide for a surface. If the surface is assumed to have cylindrical symmetry (if for example, the surface has been diamond turned), then this method is useful for indicating high spots that need additional machining.

Contact profilometry will not work for gossamer mirrors as any pressure on the surface results in large deformations. In addition, for polymer forms cylindrical symmetry cannot be assumed.

5.3.2 Phase shift interferometry – areal 3D measurement

The traditional method of measuring the form of large optics is using an interferometric method [30]. Optics divert a plane wave to the idealized shape of the optic, then the fringe pattern on the surface is checked for areas that need further work. In many cases, a CCD camera captures the image of the fringe pattern for analysis.

Although phase-measuring interferometry is possible on a large optic such as this mirror, it can only make a limited number of measurements over a given surface area. Typically low-resolution CCD cameras, e.g., 640 x 480 pixels, are used to determine the surface features, and this assumes that the difference in depth from one pixel to the next is only a fraction of the wavelength of visible light. If a phase-measuring interferometer is used to image the entire surface of a mirror (~0.2 m^2 for some test surfaces) each pixel images ~1 mm^2. From one pixel to the next, the distance to the surface will change by many wavelengths, so it is not possible for this type of interferometer to measure such a large and imperfect surface in its entirety.

Even in cases where the surface is nearly perfect, each form requires its own custom reference optic or holographic grating. Often for this reason the interferometer method is used only at the final evaluation step. For the machine design proposed here, it is desirable to have a device that can measure the form of a mirror at every step along the way, even if there are significant deviations from the desired form of the surface.

5.3.3 Non-contact laser rangefinder

A measurement machine using a non-contact laser rangefinder was built by Dr. John Main at the University of Kentucky in 2001. In this machine the X-Y stage was suspended over a flange, which held the mirror in place during measurement. A sketch of this device is shown in Figure 5-2. X, Y coordinates were sent to the stage and the resulting Z data were recorded. To remove systematic errors a flat reference surface was also measured and the difference was subtracted from the raw data file.

At the time of its inception it was recognized that the laser device is only able to measure surfaces at normal or near-normal incidence. As the laser moves closer to the edge of the mirror the angle to the normal becomes too large and the data become unreliable.

In addition, as the laser moves across the stage, some cantilevering of the mechanism is inevitable. Using a reference flat cancelled out any deflection *distance*, but does not correct for a deflection *angle*. Such an angle causes cosine-type errors in measuring a flat surface, but causes a much more complex systematic error in the data from a curved surface. Of the three prior methods studied, this approach has the fewest limitations. A machine that more closely follows the contours of the mirror surface will be able to eliminate many of the limitations of this early prototype.

Laser moves in X and Y

Laser measures Z distance

Support beam bending

Mirror surface
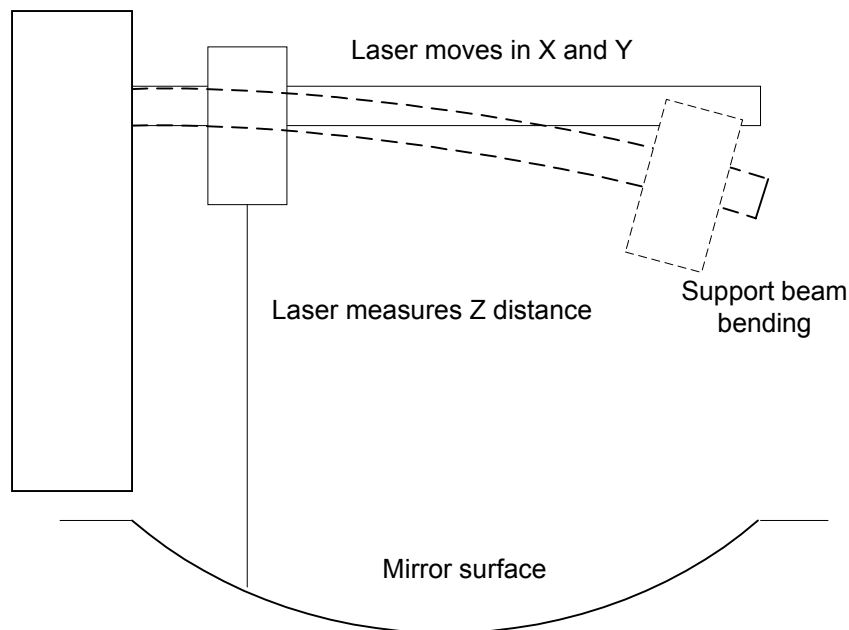
Figure 5-2. Preliminary surface measurement device.

5.4 Common Machine Components

Although two different machine designs are proposed in this chapter, both of these designs share several common elements. These include the mounting and support structure of the mirror, as well as the capacitance gage support that is combined with an interferometer.

For a thin-film mirror, much more so than a standard rigid mirror, the support is critical to producing the correct shape. As useful as they can be in many applications, kinematic constraints are not feasible for such a flexible surface. Rather a "nest" structure with a machined upper surface is described that provides uniform support to the entire flat edge of the mirror. This nest is mounted to an air bearing spindle which provides the most uniform rotational motion possible.

As discussed in Chapter 4, the capacitance gage has an active range that is insufficient for many applications, including this one. What is needed instead is the averaging ability of the capacitance gage in combination with an accurate displacement sensor, namely a laser interferometer. Such an interferometer, looking at a reflective surface mounted to the back of the capacitance gage, could accurately measure displacements even from surfaces that are not conducive to direct interferometric measurement. Motion of the capacitance gage is designed to maintain a constant distance from the target surface by means of a voicecoil and air bearing support, as described in Chapter 4. The displacement reading is therefore read from the interferometer system, which only requires that a single surface be measured continuously.

5.4.1 Mirror mount

To accurately measure the mirror surface the entire mirror must first be mounted in a way that does not induce strains or vibrations in the polymer. In the previous system described in Section 5.3.3, a large hole cut in a flat plate was used to support the edge of the mirror. Most strain in this configuration is due to gravity effects, which can be modeled if enough of the material properties are known. Since there is no way to eliminate these body forces, the best that can be done is to make them symmetric, i.e., by mounting the mirror so that it rotates around a vertical axis.

As with most gossamer optics, the mirror is designed to be supported only by its edges, so a "nest" has been designed that allows for uniform support of the edge of the mirror. The nest also has a series of holes around its upper surface that provide a slight vacuum to hold the film in place during measurement. This nest is shown in Figure 5-3. The mirror is mounted horizontally not only because this provides symmetric distortion due to gravity, but also to prevent it from collapsing under its own weight. The nest is in turn mounted on a precision air bearing spindle.
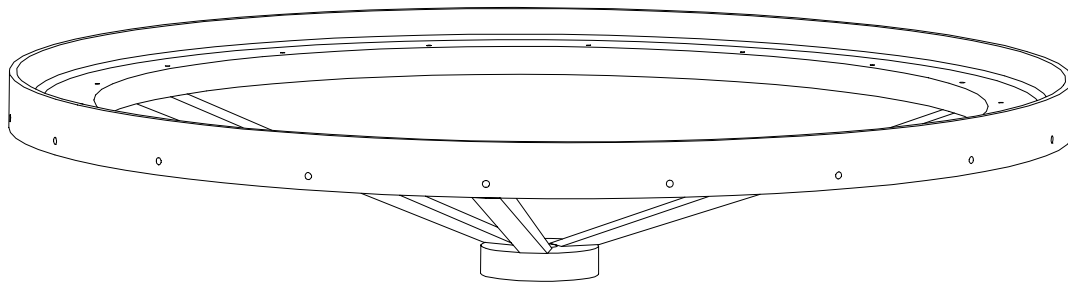
Figure 5-3. "Nest" for supporting thin flexible mirror

Because the surface shape can be profoundly affected by the position in which the edge is held, it is proposed that a registration system be implemented in the forming and measurement steps. This registration or "punch" system involves first punching precision holes in the flat polymer sheet outside the diameter of the formed mirror (see Figure 5-4). When the film is mounted prior to forming, these holes are used for alignment in the clamping mechanism. As long as the film is not drawn from under the clamp the holes will be in precisely the same position on each mirror. The metrology machine would have identical pins for precision mounting of the mirror, ensuring that the clamped edge of the mirror is not out-of-round. This system allows for reliable, repeatable mounting of the mirrors. Otherwise, the mounting of the mirror could greatly distort the edge of the mirror, an example of which is shown in Figure 5-5. Here the correct edge (as shown when the mirror was formed) is juxtaposed against a different boundary condition applied during mounting for measurement. It is clear that a mirror with such a distorted boundary condition will change its shape over nearly its entire surface.

Punches
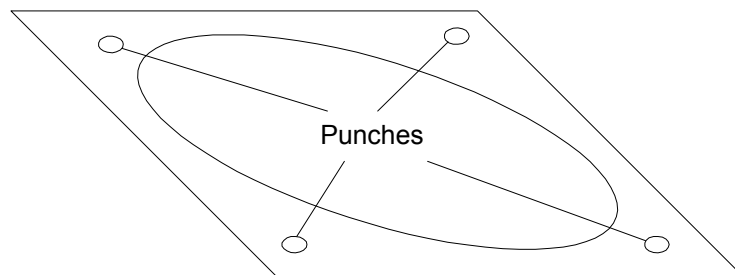
Figure 5-4. Proposed punch system.

Possible edge boundary

Correct edge boundary
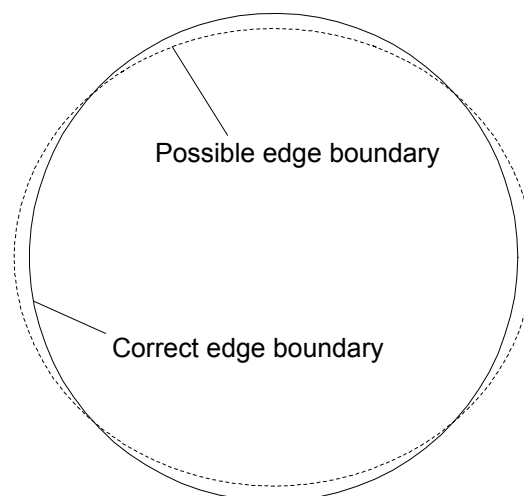
Figure 5-5. Comparison of correct edge boundary condition to likely edge support.

98

Other factors that affect the shape of the mirror include air currents, vibrations of the system, and centripetal forces. Assuming that the measurement system is sealed from currents in the surrounding air, the only air currents present near the mirror surface are those induced by the motion of the mirror and the gage. Slowing down the measurement rate (and therefore the rate of movement of the mirror and gage) is a certain way to eliminate any motion due to air currents. The tradeoff is of course increased read time for a fixed number of data points. Similarly, centripetal forces due to any rotation of the mirror can be reduced to negligible levels by reducing the read rate.

More problematic is the reaction of the surface to system vibrations. To maximize inertial damping it is proposed that the air bearing and nest structure be constructed on an existing 5-ton granite table in the Precision Systems Laboratory. If this proves insufficient to eliminate vibrations, direct damping of the mirror surface is proposed, by immersing the mirror in a viscous fluid. Unlike the mirror itself, which has very little damping, this arrangement would easily eliminate low frequency oscillations of the surface. This method would only be utilized if no other means is available to sufficiently eliminate forcing vibrations in the mirror.

As mentioned before, the rotational degree of freedom for the mirror is applied by mounting the nest on an air bearing spindle. This air bearing spindle minimizes errors due to spindle error motions, including tip and face motion errors.
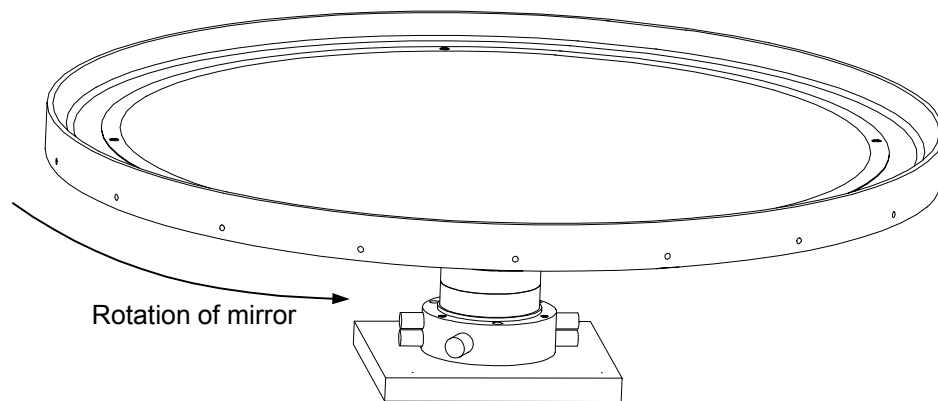
Figure 5-6. Air bearing rotation of the mirror.

5.4.2 Capacitance gage

The capacitance gage to be used in this application is identical to the device analyzed in Chapter 3 and Chapter 4. Since the mirror surface is conductive (and is grounded in both machine designs), the gage senses displacements from a nominal distance to the surface of the

mirror, approximately averaging this distance over the sensing area. As described previously, the resolution of capacitance gages ultimately depends upon the data acquisition system and the magnitude of the form errors (range of measurement), but commercial cap gages can easily achieve resolutions below 10 nm with 16-bit D/A conversion.

The advantage of using a capacitance gage to measure the displacement to the surface is in its averaging effect over the active area of the sensor (typically ~2 mm^2), thus separating out roughness from waviness wavelengths. The size of the active surface area is also compatible with the number of measurement points desired for analysis purposes. Considering for example the mirror described in Section 5.2, the area is roughly 500,000 mm^2, indicating that with a slight overlap several hundred thousand unique data points can be measured.

As discussed in Chapter 4, a capacitive gage such as that proposed can detect relatively large changes in displacement (1 mm or more on lower sensitivity settings [31]) only at the expense of resolution. The system proposed in Chapter 4, where the cap gage is mounted on a small air bearing and kept at a constant distance from the surface using a voicecoil or linear motor and closed-loop feedback, will be used in both machine designs. The feedback-controlled displacement of the capacitive gage in the radial direction will be measured by a laser interferometer system. A similar scheme has been proposed previously using a commercially available CD optical head [32], but this optical device does not have the averaging advantage provided by the capacitance gage.

One limitation of standard commercial capacitance gages is in the range of acceptable angles to the target surface. Because of the small gap and relatively large flat surface (including guard ring structure), the maximum angle of one commercial gage is calculated to be ~ 2.3 degrees at the highest sensitivity setting. Ultimately this range limits the mirror geometries that can be measured, and highlights the importance of proper alignment when setting up this machine.

To minimize thermal effects on the accuracy of the measurement, the support structure of the capacitance gage is to be made of zerodur or a similar low-CTE material. It is only necessary to use zerodur in the gap between the capacitance gage and the mirror for the interferometer, as the expansion or contraction of other components is irrelevant to the measurement.
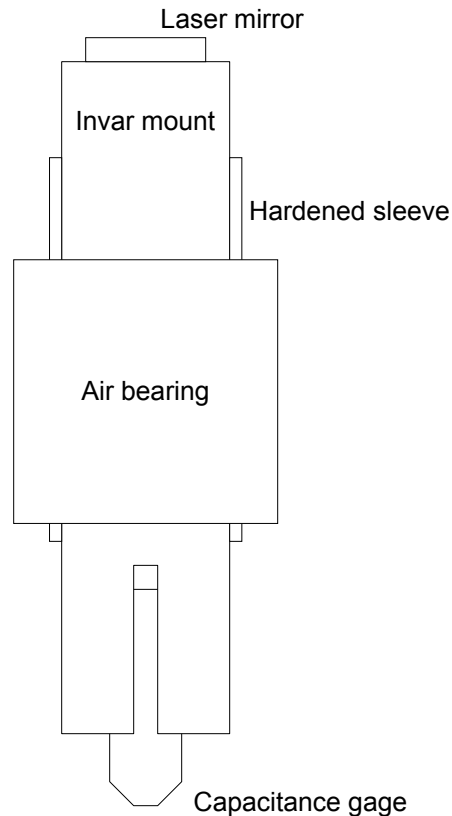
Figure 5-7. Capacitance gage mount with mirror, made of zerodur.

5.4.3 Displacement-measuring interferometer

As mentioned before, the active range of a capacitance sensor is many times smaller than the travel necessary to measure the surface of an 80 cm diameter mirror. In the previous measurement system a laser was used to measure the distance to the surface of the mirror using time-of-flight. What is proposed in this improved design is that a laser interferometer be used to measure the displacement of the capacitive sensor mount. By knowing the displacement of the sensor mount, as well as the fixed dimensions of the mount, the distance to the surface of the mirror can be measured with a precision comparable to that of the capacitance gage or the interferometer alone.

A laser interferometer is a system that uses interference from two laser pathways to determine changes in lengths of the pathways. Typically one pathway is the "reference" pathway, a fixed distance, and the other pathway changes in length. Coherent light from a laser is passed through a beamsplitter and half of the light travels each path. Upon its return the light is recombined and sent to a photodetector. If the lengths of the two paths differ by an integer

multiple of the wavelength (a typical visible wavelength is 500 nm), then the two waves interfere constructively, and the light on the photodetector is maximized. If the measurement path length changes and the paths now differ by a half wavelength, the light interferes destructively and no signal is measured by the photodetector.

Commercial interferometer systems are able to convert the signal from the photodetector into a displacement measurement. Since the system has no "zero" starting point it is only possible to make displacement measurements with an interferometer, and consequently a measurement of a mirror surface would have to be a contiguous set of data. By placing a retroreflector on the back side of the capacitance gage mount as shown in Figure 5-7, the interferometer would always be utilizing a quality optical surface for its measurement pathway. Also since the capacitance gage and its mount would only travel in the radial direction, this reference surface would always remain perpendicular to the light pathway, as required for optimal measurements.
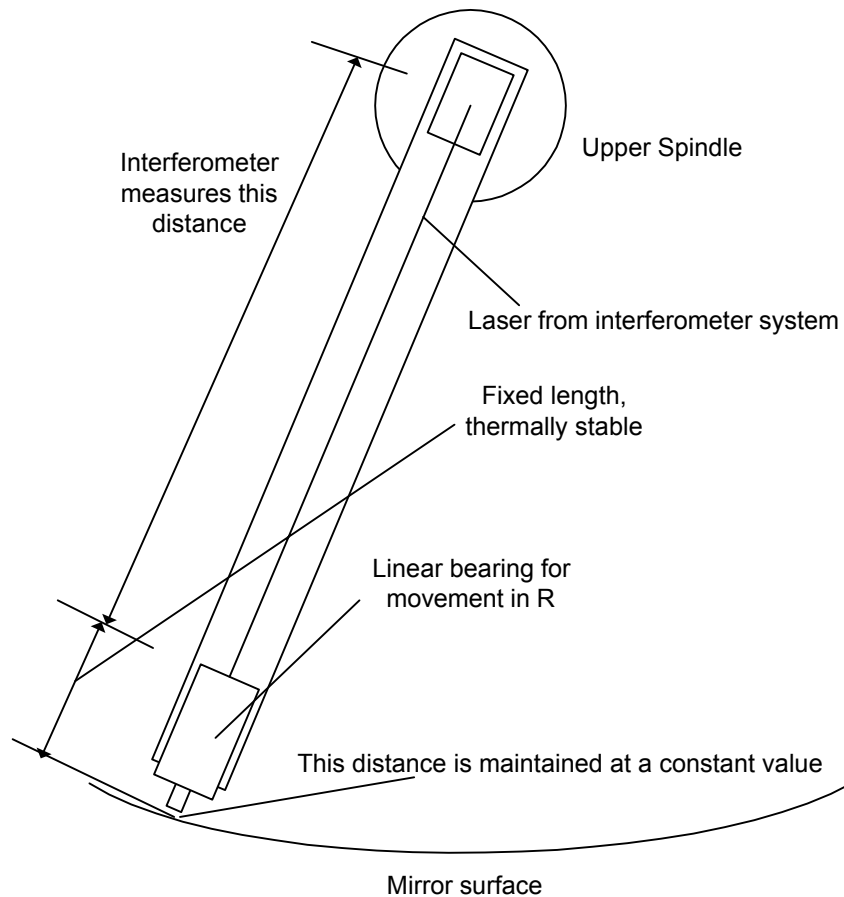
Figure 5-8. "Pendulum" design for a measurement machine.

5.5 First Design: The "Pendulum"

The pendulum design sketched in Figure 5-8 is the most straightforward of the two machine designs. The upper spindle supports a stiff but lightweight arm that in turn supports the linear bearing and voicecoil. This spindle is mounted in a large overhead structure, most likely granite, which allows for multiple mounting locations of this spindle.

The laser for the interferometer passes through the center of this spindle, then is reflected downward, along the arm, to the back side of the capacitance gage mount. As mentioned previously, this component is to be made of a low CTE material. Because this light pathway includes the main pendulum arm, the interferometer is able to measure changes in the length of this arm due to gravity, temperature fluctuations, etc. Temperature changes may also affect the surrounding granite structures, but they have a much more significant thermal mass and would therefore change much more slowly and measurably.

5.5.1 Advantage in sensor configuration

As can be seen from the diagram in Figure 5-8, the system proposed measures spherical coordinates of data points, namely R, θ, and ϕ values of the mirror surface, instead of the previous X, Y, Z measurements. These three degrees of freedom are more suitable for this type of surface, and allow for tremendous improvements in accuracy. Using standard spherical notation the R measurement is provided by the interferometer, the θ angle by the upper spindle, and the ϕ angle by the lower spindle. By aligning the upper spindle with the nominal center of curvature of the surface, the total travel in the R direction is minimized.

Another point in favor of this design is the fact that each of the three coordinates of a surface point is an independent measurement. By having each measurement produced by a separate device, the possibility of error propagation is greatly reduced. Figure 5-9 shows a downward-looking plot of paths traversed by the capacitance gage. Alternatively, circular paths could be traversed along the system, again with equal ease in recording the angular coordinates of each data point.

5.5.2 Difficulties in accommodating different curvatures

The most fundamental limitation of the pendulum design is its inability to measure a wide range of different curvatures. Since the upper spindle must be aligned with the nominal center of curvature of the film, relatively flat mirrors require mounting the spindle high above the surface.

Any offset between the spindle and this center results in added tilt between the capacitance gage and the surface. A sample plot of this increase is shown in Figure 5-10.
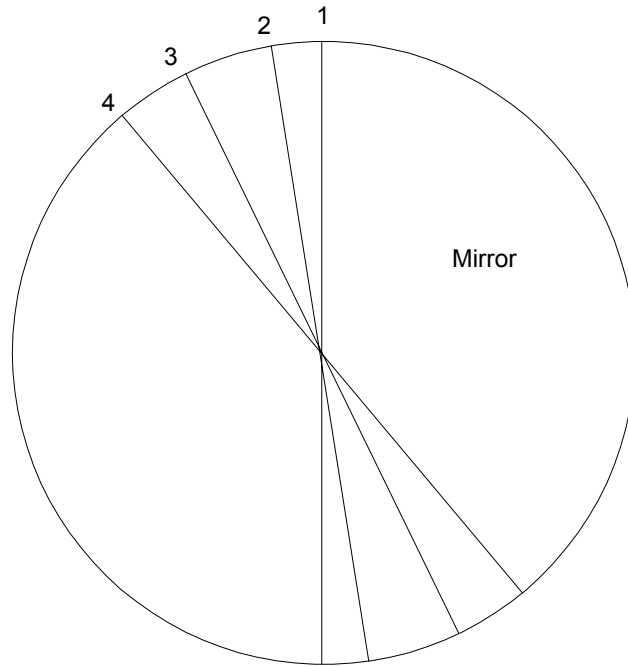
Figure 5-9. Downward-looking plot of lines (numbered) traversed by pendulum design.
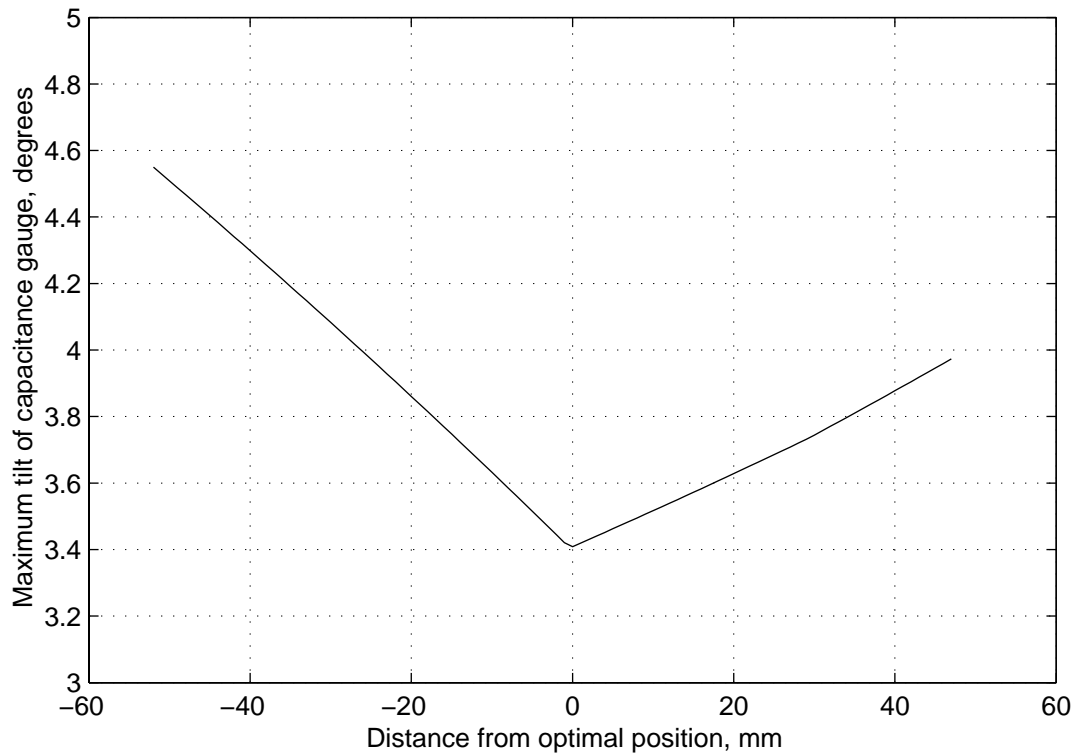
Figure 5-10. Tilt angle due to spindle offset from film center, pendulum design.

As the radius of curvature of the mirror increases, the length and mass of the arm increases, with a third-order increase in the bending angle of the arm. Even if multiple mounting locations for the upper spindle are machined into the upper granite structure, the final alignment must be achieved by raising/lowering the film, necessitating z-axis motion of the lower spindle. Alignment of the center of the film under the zero position of the pendulum arm requires x and y axis control of the lower spindle as well. With each additional translational degree of freedom, 6 additional terms are required in the error budget. The second design is able to eliminate one of these alignment translation stages.
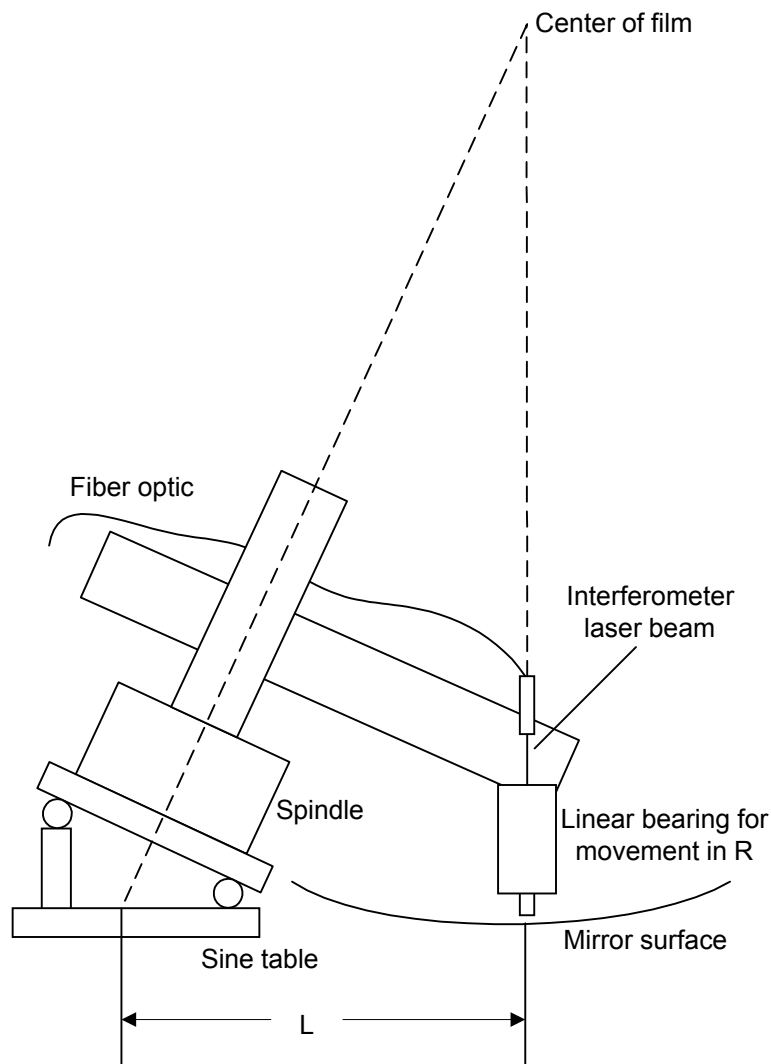
Figure 5-11. "Swingarm" design for a measurement machine.

5.6 Second Design: The "Swingarm"

The swingarm design shown in Figure 5-11 uses a different geometrical configuration to position the capacitance gage over various locations on the mirror surface. In this case a horizontal arm rotating on a tilted axis suspends the capacitance gage mount above the surface. The capacitance gage is moved in the radial direction by the same voicecoil arrangement described above. As can be seen from the figure, a huge advantage to this system is that the arm is only slightly larger than the radius of the mirror. For different radii of curvature, only the angle of the sine table changes. This geometrical relationship is given [33] by Eq. (5-1).

$$\sin\theta = \frac{L}{R} \qquad \textbf{(5-1)}$$

Where L is the perpendicular distance from probe tip to axis of rotation as shown in Figure 5-11, and R is the nominal radius of the mirror. Once the approximate angle is set by adjusting the sine table, the mirror is moved to its final position using x and y axis control. No z-axis motion of the mirror is required for alignment. As can be seen from the above equation, the swingarm design can even accommodate a mirror of infinite radius (flat surface), by setting the angle θ to zero. Finally, since this design locates the measurement equipment to one side of the surface, other equipment (e.g., optics) can be mounted overhead.

5.6.1 Swingarm design limitations

One downside of this swingarm arrangement is the difficulty in choosing the optical path for the interferometer. Current thinking is to bring the laser to the end of the arm using fiber optics, measuring just the travel of the capacitance gage relative to the end of the arm. No longer can the laser pathway measure all vertical motions of the capacitance gage mount. Instead, corrections due to arm bending and thermal drift must be included later, as described in Section 5.7.

A second difficulty arises when calculating the location on the mirror surface of measured points. As can be seen in Figure 5-12, rotating the capacitance gage causes arcs to be traced on the surface of the mirror. The position of these points is calculated from knowledge of the distance L of the machine and the angular information from the two spindles.
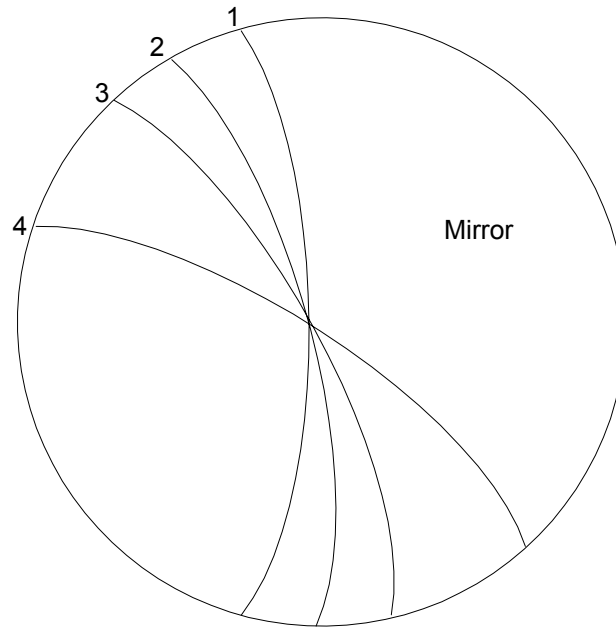
Figure 5-12. Downward-looking plot of arcs traversed by swingarm design

5.6.2 Parametric swingarm studies

To study the geometry of the swingarm model in greater detail, a skeleton model of the structural components was created in ProEngineer. This model, shown in Figure 5-13, was used to perform sensitivity studies as the arm traversed the surface. First, a spherical surface was created and the probe swept across its surface. As expected, with optimal alignment the probe surface remained equidistant and parallel to the mirror surface at all angles. Of greater interest is the clearance of the main arm with respect to the edge of the film, as plotted in the upper graph of Figure 5-14. This information is helpful when designing the arm and nest structures.
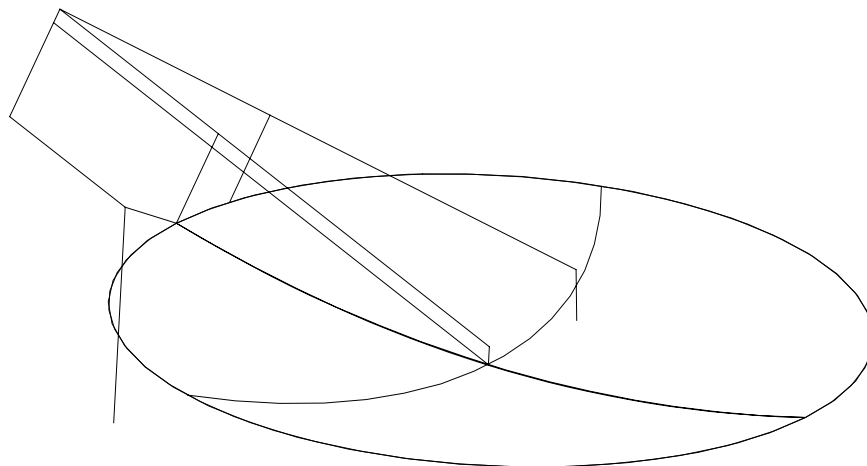
Figure 5-13. Skeleton model of swingarm design for parametric studies
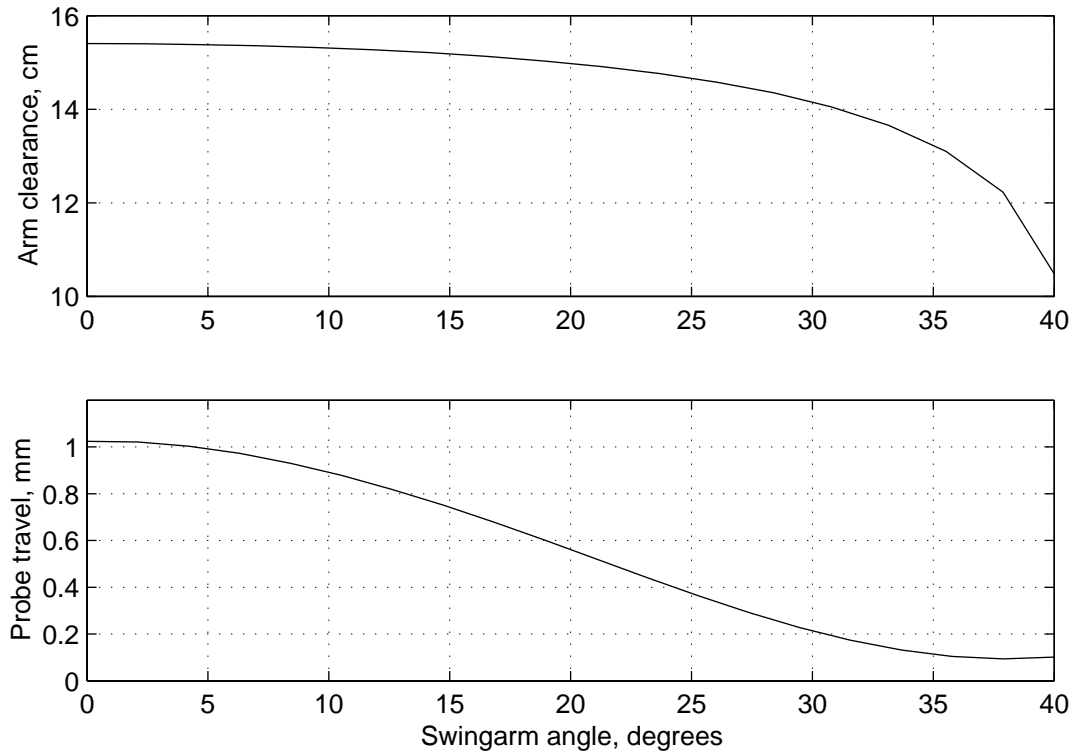
Figure 5-14. Results of two parametric studies of swingarm design.

A second study modeled a parabolic mirror surface with similar dimensions to the original, spherical surface. The lower graph of Figure 5-14 shows the radial travel such a surface would necessitate. This information is needed to determine if the air bearing and voicecoil have sufficient travel.

5.7 Postprocessing Corrections to Data

Several corrections to the raw data of this machine are anticipated and have been analyzed. These include systematic errors due to slight offsets in the capacitance gage, errors due to a tilted mirror surface relative to the capacitance gage, and finally errors due to beam bending in the machine. All of these errors can be corrected for after the collection of the raw data file, as a postprocessing step.

Not all errors can be determined prior to the building of the machine. Temperature changes in various parts of the machine alter the dimensions slightly; in both designs some of these changes will be in the sensitive direction. Only after the machine is built and installed can machine component temperatures be measured and their effect on the accuracy of the machine determined.

5.7.1 Capacitance gage offset

Chapter 4 presents a feedback loop that positions the capacitance gage at a fixed distance from the reference surface. This fixed distance is such that the capacitance gage output is zero volts, and the forces on the air bearing rotor due to the voicecoil are zero.

In a real machine some small forces will be required to maintain the position of the capacitance gage, therefore the capacitance gage will not be positioned at the nominal distance. Since the forces required will vary over the surface of the mirror, it is important to register this offset of the capacitance gage and add or subtract this displacement from the displacement measured by the interferometer.

Fortunately, the output of the capacitance gage is easily monitored and is already in a form that lends itself readily to digitization. It is proposed that during data collection every reading of the interferometer will also include a reading of the voltage output of the capacitance gage. With this information these small offset corrections can be made to the data to more accurately determine the location of the mirror.

5.7.2 Slope correction

For these large radius mirrors the capacitance gage will "see" a surface that is essentially flat. Curvature corrections such as those proposed in Chapter 3 are not needed at this scale. A similar sort of systematic error does occur whenever the capacitance gage is tilted with respect to the surface being measured, rather than being perfectly parallel.

Just as with the curvature problem analyzed in Chapter 3, deviations from the target arrangement used during calibration will result in erroneous displacement measurements. Since the capacitance gage is factory-calibrated using a parallel surface, any tilt of that surface results in the capacitance gage perceiving a smaller displacement. This tilt is shown two-dimensionally in Figure 5-16, although of course this tilt exists in three dimensions. Although the curved surface was solved using FEA, this tilted surface does not offer any axial symmetry for FEA. The computing power required for an FEA solution is therefore significantly larger.

Closed-form solutions to this capacitance problem do exist for small angles [34], one such solution is shown in Eqs. (5-2) and (5-3).

$$C = \frac{2\pi\varepsilon r^2 \cos\theta}{d}\left[\frac{1-\left(1-k^2\right)^{0.5}}{k^2}\right] \tag{5-2}$$

$$k = \frac{r\sin(2\theta)}{2d} \tag{5-3}$$
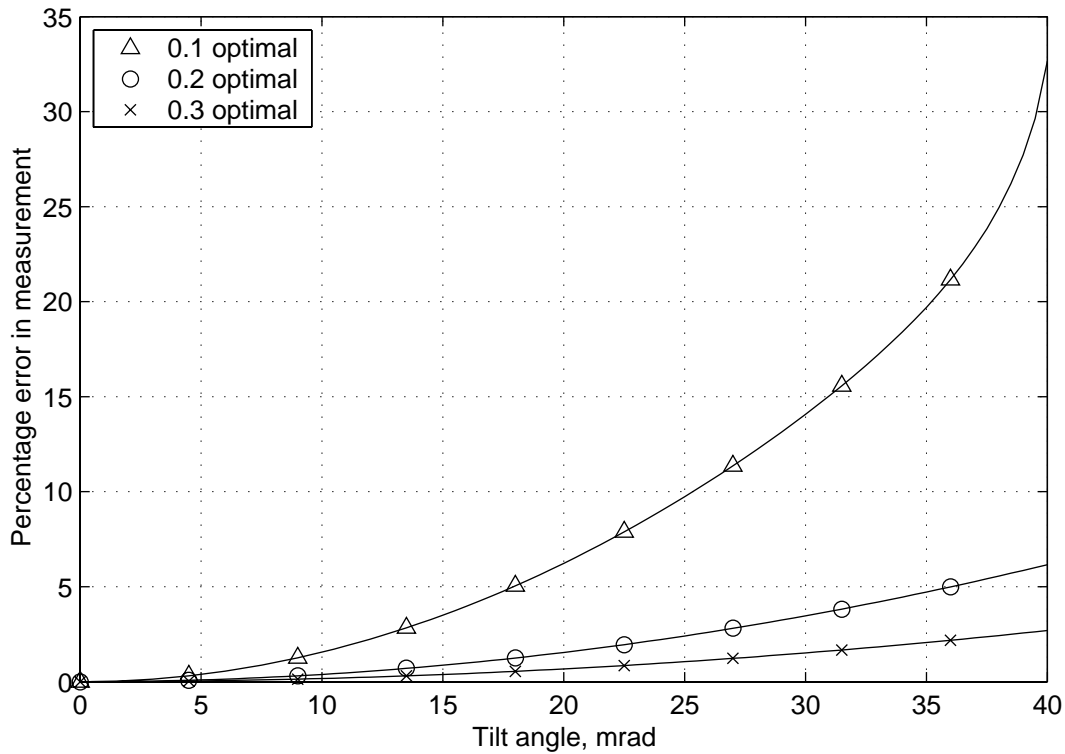
Figure 5-15. Plot of distance offset as a function of tilt angle, optimal spacing in mm.
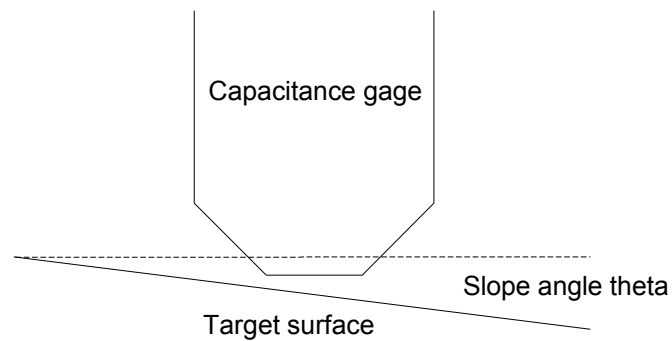
Figure 5-16. Capacitive sensing of a sloped surface.

Solving these Equations for the geometry of the capacitance gage and various nominal gap distances results in Figure 5-15. These lines show the percentage error in distance for a

110

particular spacing and tilt angle. If the tilt angle at a particular data point is known, this correction can be added to radius values from either machine design. These tilt angles can be determined by applying a gradient function (similar to those built in to Matlab) to the raw mirror data. Since the slopes are calculated from the radial distances and the radial distances are corrected slightly by using the slopes, two or three iterations of this correction may be required.

5.7.3 Use of a reference surface

Another systematic error is due to structural bending or extension of the measurement arm. As discussed previously, in the pendulum design the extension of the arm is included in the measurement of the R value by the interferometer. At any position other than vertical there also exists bending in the arm, which is manifest in both deflection and tilt at the end of the arm. Tilt errors are most likely much smaller than the tilt encountered by the cap gage simply due to the mirror surface being aspheric. Equations for deflection can be solved as a function of the arm angle, and these can be used to correct the location of the measurement point in postprocessing.

For the swingarm design, the arm is primarily in a bending mode, although the direction changes as a function of both sine table and spindle angle. For this reason it is advisable to use a hollow cylinder as the arm structure, since this geometry has a uniform moment of inertia for bending at any angle.

For either machine design, the theoretical bending needs to be tested experimentally to determine the validity of the model. It is proposed that, rather than testing individual components, the entire assembly should be testing using a known reference surface. A diamond turned (rigid) mirror such as one manufactured for a ground-based telescope can serve as a test bed to validate the functionality of the form measurement machine. Even if the form of the mirror is not ideal as long as it is known then it can serve as a reference measurement to compare against measurements from the proposed machines. The difference in the two measurements becomes the error map for the machine. This is the ultimate test of the accuracy and repeatability of this machine.

5.8 Conclusions

Accurate form measurements of large-scale reflective optics are critical to refining their manufacturing processes. Previous measurement systems suffered both from limited accuracy and a lack of ability to easily separate form error from roughness and waviness. Many of these systems were designed to measure rigid optics, not the thin-film "gossamer" optics favored for future space applications.

A non-contact measurement system is proposed that would average out these roughness and waviness variations while providing form measurements over wide variations in the radius of curvature. This system combines a capacitive gage with a displacement measuring interferometer to determine the form of the mirror with high accuracy and repeatability.

Of the two designs presented, the swingarm design has been selected due primarily to its greater flexibility in measuring a variety of surface curvatures and to its shorter arm length. Also, the lower profile of the equipment makes this design more easily built from existing machine structures. A solid model of this design is shown in Figure 5-17. To determine correction terms due to bending of the structure, a reference mirror of known form will be measured and the differences between measurements used as an error map.
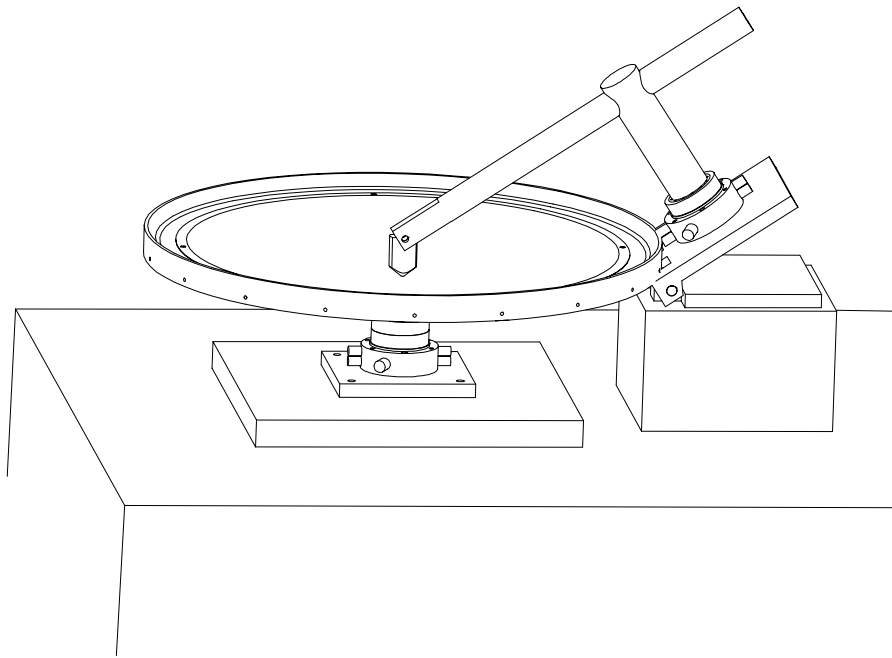
Figure 5-17. Solid model of final machine design.

6:
Conclusions and Future Work

With the prevalence of high performance sensors in the laboratory, it is important to understand the conditions under which their performance is achieved. It is also necessary to understand what effect non-ideal conditions have on those same performance parameters. This has been the focus of this study of capacitive displacement sensors. It has been demonstrated that the effects of placing the capacitance gage in proximity to a spherical target can be reproduced using finite element analysis, with results that closely match empirical measurements. The range limitations of the capacitance gage can be overcome by pairing it with an air bearing and an additional displacement sensor. Finally, a machine using these devices has been conceptualized and modeled.

6.1 Capacitive Displacement Sensors

Capacitive displacement sensors offer non-contact sensing of a wide variety of conductive surfaces using a rugged, sealed probe with no moving parts. This device is calibrated at the time of manufacture to be highly linear over its active travel range of a few hundredths of a mm. The nature of the device being electronic, the inner, sensing conductor is shielded from outside effects by both a guard ring and a grounded shell. It has been shown that the guard ring limits the fringing of the electric field at the edge of the sensing element, increasing the linearity of the device. The linearity of the output of the capacitance sensor with displacement is achieved by an electronic circuit that compares peak voltage to peak current. This output is a function of the inverse of the capacitance C, which is linear with the gap distance d.

It has been shown that several applications, including spindle metrology, cannot provide a flat reference surface for measurement by the capacitance sensor. Instead a cylindrical or spherical surface becomes the available target. Since no closed-form solution exists for modeling the complex electric field between the central, sensing conductor, the guard ring, the ground shield, and the target surface, finite element modeling is chosen to simulate a variety of different spherical targets and distances d.

113

6.2 Finite Element Modeling

The solution to the finite element electric field problem first takes the form of a scalar potential, analogous in many ways to conduction heat transfer problems. The temperature solution of a heat transfer problem is compared to the voltage potential between conductors in the electric field problem, with constant temperature surfaces mathematically identical to surfaces of conductors, where voltage is constant. The cylindrical form of the equation takes the form of Laplace when no charges are present in the system.

To solve electrostatic problems in the Ansys software a model of the geometry must be built using keypoints, lines, and areas. Since the problem to be solved is axisymmetric, two-dimensional areas are used to represent three-dimensional volumes. Once areas are meshed, the boundary conditions of constant potential are applied to the lines bordering conductors, and a special infinite condition is applied to the outer edges of the model. This condition is necessary to represent the fact that all other conductors are "infinitely" far away.

To compare the finite element solution to closed-form solutions, a two-conductor model is created of a parallel plate capacitor. The capacitance *C* of this system is solved with several different meshes and outer boundary conditions, with excellent results when compared to the theory. Next a model of the actual capacitance gage configuration is built and tested against a flat surface. For this system of four conductors, a more complicated algorithm must be used to determine the lumped capacitance values between each pair of conductors. The electric field solution can also be presented graphically, where the effects of the guard ring on the fringing of the electric field can be shown. Also, the capacitance results are compared with a closed-form solution of the guard ring geometry, again with good correlation.

Once the validity of the finite element model has been proven, the model is modified to include a spherical target surface. When these results are compared to the flat surface values, it is clear that the same distances (as measured from the center of the capacitance gage) produce very different capacitance values. It is necessary in most cases to run test cases to determine the correct distances to produce capacitance values comparable to the flat cases. Otherwise, the capacitance gage electronics would not consider the positioning of the gage to be "on-scale." These capacitance values are then analyzed to determine the appropriate method to remove the errors associated with the curved surfaces.

6.3 Nonlinear Compensation

Once the capacitance values for flat surfaces and varying-diameter spheres have been calculated using finite element analysis, the next step in the process is to plot these results and determine the best-fit lines through each set of data points. First the flat surface was plotted, since this is the basis on which the capacitance gages are calibrated. Two sets of data corresponding to the manufacturer's "fine" and "ultrafine" gain settings are fit to two different lines with similar (but not identical) slopes. By subtracting the best-fit line from the actual capacitance data, the nonlinear residual is calculated and plotted. This curve is to be compared to the same curve from the spherical surface measurements.

Because the capacitance gage is correctly calibrated for measurements of a flat surface, the finite element results can also be used to calculate the output voltage for any particular capacitance. It is important to recognize the limitations of the electronics, particularly the fact that the output will flatten out beyond its –10 V to +10 V active range.

To determine the output voltage as a function of capacitance, two methods are possible. In the first, the best-fit line from the flat target data is used to determine a linear equation between inverse capacitance and displacement. Another linear equation converts this displacement to output voltage. This method has the advantage that capacitance values outside the range included in the flat surface data can also be plugged into the linear equation with good results. In this way the capacitance values from the curved surfaces are converted into "measured" displacement. These displacements are plotted against the actual or "real" displacement that was used in the finite element simulation. These graphs provide a lookup table by which the output of the capacitance gage electronics can be converted into the actual displacement of the device.

Although this linear best-fit method is able to extrapolate beyond the original capacitance range, it was shown that the capacitance gage electronics actually remove some of the nonlinearity present with the flat target. Therefore, it is more appropriate to use a higher order polynomial fit to the data to correlate capacitance values from one simulation to the other. Finally, to produce evenly spaced data points for the final analysis, it is deemed better to fit polynomials to the spherical capacitance values, plugging in the more evenly spaced capacitance values from the flat surface analysis to determine the relative slope between displacements.

6.4 Air Bearing Support and Control

Although capacitance gages show high sensitivity to small displacements, the disadvantage of such a high sensitivity is a relatively small active range. Many applications could benefit from the non-contact, averaging abilities of the capacitance gage, but require a larger travel range than available even at the lowest gain setting.

Laser interferometers have sensitivity on par with that of a capacitance gage, but ideally require a mirror surface to accurately gage displacements. To combine these two displacement sensors into a single unit, a control system is proposed that uses the capacitance gage for sensing surface features, but maintains a constant distance to that surface. The displacement of the air bearing stage that supports the capacitance gage is, in turn, measured by the interferometer.

Such a control system was built and tested using an available capacitance gage, air bearing stage, and linear amplifier. The resulting system was modeled as a second order oscillator with damping, and evaluated using several methods. Amplitude and phase response were difficult to measure due to long settling times at low frequencies, but Bode plots did confirm the validity of the second order model. Closed loop response testing revealed large numbers of oscillations, indicative of a small damping coefficient, as expected from the air bearing support. Measuring the closed loop response as a function of various gains allowed for a determination of a second order system model. From this point, several digital filter results were tested until the desired settling time and overshoot were achieved. To accomplish these same results at lower cost, an equivalent analog control design is presented.

6.5 Large Mirror Form Measurement Machine

One such application of the air bearing support is in a machine to measure large format mirrors. Many of these mirrors are made of lightweight, flexible materials, and therefore require a non-contact gage such as the capacitance sensor. To measure these near-spherical surfaces, two machine designs were proposed and evaluated in terms of flexibility and ease of use. A mount is proposed to support such a mirror, and two air bearings spindles are used to position the mirror under the capacitance sensor. Since such a large surface will require greater travel than permitted by the capacitance gage alone, the air bearing support in combination with a laser interferometer is proposed to record displacements.

When comparing and contrasting the swingarm vs. the pendulum design, the swingarm is shown to be far simpler, but its setup is too inflexible for measuring different curvatures. Also, as many large-format mirrors are nearly flat, the apparatus required for such a radius of curvature would be impracticall large. It is therefore concluded that the swingarm design is the most promising of the two.

6.6 Future Work

There are several different areas that could be studied based on the techniques and concepts presented in Chapters 2 through 5. These primarily involve extensions of the ideas presented to other geometries and applications where they would be found useful.

6.6.1 Other capacitance geometries

The finite element analysis presented in Chapter 2 studied spherical target surfaces using an axisymmetric finite element analysis. For many high performance bearing and surface measurements a cylindrical target surface is used. Although the capacitance gage also has cylindrical symmetry, when the capacitance gage is targeting the walls of a cylinder there are only two planes of symmetry to the problem. It is necessary in this case to build a three-dimensional model of one quarter of the capacitance gage and the target surface, requiring many hundreds more elements and much greater computing power.

When comparing a cylinder to a sphere qualitatively, it is apparent that the sphere has curvature in all directions, while the cylinder has curvature along one plane of symmetry but is flat in the other plane. It is anticipated, then, that the nonlinear effect of curvature for a given cylinder diameter would be less than that for the equivalent sphere. Just as larger spheres were closer and closer to the flat data points, the cylindrical surface should approach the flat data for large diameters.

In the analysis of capacitance values found in Chapter 3, only polynomial fits to data were used to interpolate between data points. In time and with further analysis, it should be possible to create a mathematical model that more realistically portrays the effects of capacitance and target spheres. Such a mathematical model may take into account the average distance to the surface, as well as including the effective radius of the sensing element. Of greatest value would be a closed-form determination of the new gain values as a function of sphere diameter.

6.6.2 Mechanical improvements to air bearing support system

With the success of the preliminary system described in Chapter 4, including a method to implement the control electronics in the analog domain, future work should include the optimization of the dimensions of the mechanical components of the system. Although the voicecoil and air bearing functioned as expected, both were many times larger than necessary to support the weight of the capacitance gage. The optimal system must consider the mass to be carried and the forces involved.

To determine how the transfer function of a system would change as the mechanical components are modified, it is useful to revisit Figure 4-5. Changes to the mechanical components would change the voicecoil, the mass, and the damping term. For the purposes of this discussion the amplifier and the capacitance gage would remain the same.

Given the relative size of the capacitance gage compared to the air bearing rotor, it is determined that the ideal support structure should be approximately 5 times smaller (along each dimension). It is assumed that the force provided by the voicecoil is roughly proportional to the length of its windings. Reducing both the length and the diameter by a factor of 5 each results in a new gain value G_2 of 1.123 N/A, some 25 times less than previously.

If the mass is deemed to be proportional to the volume of the stator, changing all three dimensions results in a reduction of mass by a factor of 125, or a mass of approximately 34 g. This is nearly twice the mass of the capacitance gage, which weighs just 20 g.

To determine the change in the damping coefficient, we must examine a different form of the closed-form second order equation, shown in Eq. (6-1). In this form the damping coefficient c is multiplied by the velocity to produce a force. Dividing every term by the mass m results in Eq. (6-2).

$$m\ddot{x} + c\dot{x} + kx = 0 \tag{6-1}$$

$$\ddot{x} + \frac{c}{m}\dot{x} + \frac{k}{m}x = 0 \tag{6-2}$$

We can equate the terms in Eq. (6-2) to the terms in Eqs. (4-3) or (4-5). We then assume that the damping force (and therefore c) is proportional to the surface area of the air bearing. With reductions in length, height, and width of the air bearing, the resulting surface area will be

25 times less. However, this term is divided by the mass *m*, which we have already shown should be 125 times less. The final coefficient, then, is some 5 times larger. Starting with a value of 0.55, the new value for *c/m* is 2.75. The final system model is shown in Eq. (6-3).

$$G(s) = \frac{1,559,000}{s(s + 2.75)} \qquad \textbf{(6-3)}$$

Although this system has an even higher resonant frequency (about 1 kHz), what is more important is that the pole in the left hand plane has shifted further left. Recalling that the root locus tends to drift to the right as gain is increased, it is possible that our original design poles of $-1+j$ and $-1-j$ can now be achieved with a simple (fractional) gain. Faster settling times are also now more easily achieved with the lag compensator. For design poles of $-4+4j$ and $-4-4j$ the angle of deficiency is 68.5 degrees, less than what was required for the laboratory system with a settling time of 4 seconds.

A final improvement to the system is possible by testing other types of controllers. A lag compensator may be introduced to reduce the steady-state error. A PID controller may be designed to compare the results with that of the lead compensator. Ultimately the settling time of the closed-loop system may dictate the rate at which a surface can be analyzed.

Appendix A:
List of Variables

Q	Charge on a conductor
C	Capacitance between two conductors
ε_0	Electric field permeability of vacuum
ε_R	Dimensionless, relative permeability of a medium; always greater than 1
A	Area of a conductor
d	Distance between two parallel conductors
p	Pressure
T	Temperature in K
r	Radius of a circular area, or radial direction in cylindrical coordinates
C_f	Closed-form capacitance including fringe effects
f	Function to include fringing effects
s	Thickness of plate in parallel plate capacitor analysis (Chapter 1); frequency variable in analog domain (Chapter 4)
r_i	A radius that includes half the distance to the guard ring
C_g	Closed-form capacitance including factor for guard ring
χ	Correction to include guard ring geometry
w	Width of guard ring
g	Gap between central conductor and guard ring
I	Current to capacitor
V	Voltage applied to a conductor
ω	Angular frequency, in radians/s
Δd	Displacement from a nominal value, the nominal value generally being the value that produces a zero volt output from the capacitance electronics
I_1 and I_2	Forward and reverse measurements of rotating part
$R(\theta)$	Spindle radial error motion

$B(\theta)$	Surface profile of rotating part
G	Gain of a capacitance gage in V/mm or V/minch
k	Thermal conductivities in a heat transfer problem
q^B	Heat generation term in a heat transfer problem, or charge density in an electric field analysis
ϕ	Field potential solution to the electric field problem, in volts
W	Energy stored in a capacitance system due to voltage potentials applied to conductors
z	Axial coordinate in cylindrical coordinate system, frequency variable in digital domain
C_{12}	Mutual lumped capacitance value between conductors 1 and 2
D_{12}	Ground capacitance values used in CMATRIX analysis
r_{eff}	Effective radius of central, sensing conductor
d_r	Reference distance, the distance that produces 0 V on the output of the capacitance gage electronics
S_f and S_{uf}	Slopes of best-fit lines for fine and ultrafine gain settings, respectively
C_r	Reference capacitance, capacitance that corresponds to zero volts output
P_0 to P_3	Coefficients used for polynomial curve fitting
d_{meas}	Distance as given by the output electronics of the capacitance gage
d_{real}	Actual distance between closest point of spherical target surface and capacitance gage
C_{flat}	Capacitance values calculated by Ansys for a flat target surface
G_{fit}	Best-fit gain of voltage vs. distance for curved surfaces
G_{flat}	Gain in voltage per distance for flat target surface, as provided by the capacitance gage manufacturer
R	Nonlinear residue, curve remaining after straight line has been subtracted from calibration data
δd	Displacement resolution of digitized data
$R(t)$	Round target surface experimental measurement data
$F(t)$	Flat target surface experimental measurement data
m	Combined mass of all moving components in air bearing support system

c Damping term for spring-mass system

ζ Damping coefficient for second order system model

K Analog proportional filter (gain)

V_{in} Input voltage to control system

V_{out} Output voltage of control system

ω_n Natural frequency of second order system

$R_1, R_2,$ etc   Resistor values

G_c Lead compensator

G_{ZOH} Effective filter due to influence of zero order hold

Appendix B:
ANSYS Code for FEA

Electrostatic Analysis of Parallel Plate Problem

The following code modeled a simplified, parallel plate capacitor in Ansys. Two identical circular plates of finite thickness were modeled as an axisymmetric problem, and the results compared with closed form solutions. Since only two conductors exist in this problem, the calculation of the energy stored in the system, and then the capacitance, is relatively straightforward and does not require use of the cmatrix command. This code is contained in the file 2D_cap4.txt.

```
finish
/clear                    ! used to erase and start over analysis
/title, Axisymmetric Capacitor, h-Method
/prep7
!
! Defining the geometry of
! parallel plate capacitor in Ansys.
! Set units to mm, microfarads
!
emunit,epzro,8.854e-9    !epsilon in uF per mm
!
! Define Variables
pthick=0.05     ! Thickness of each cap plate
bplater=10      ! Base plate radius in mm
uplater=10! Upper plate radius
tilt=0   ! tilt angle in degrees
gap=0.05  ! gap between plates at center
V0=-5.0          ! voltage of base plate
V1=5.0           ! voltage of upper plate
rsph=20    ! radius of surrounding sphere
esz=5            ! size of element division (not used)
cdiv=20           ! number of divisions on cap surface
vdiv=7   ! number of vertical divisions
!
! Use same coordinate system for everything
csys,0
!
! Define lower rectangle
rectng,0,bplater,-pthick-gap,-gap
!
! Define upper rectangle
rectng,0,bplater,0,pthick
!
! Define surrounding rectangle
hgt=25*(gap+pthick)
rectng,0,1.5*bplater,-hgt,hgt
!
! Create lines and break for meshing
lesize,2,,,2           ! edge of plate
lesize,6,,,2           ! edge of plate
lesize,3,,,cdiv,10      ! select plate sides
lesize,7,,,cdiv,10
```

```
    lesize,1,,,cdiv,0.1
    lesize,5,,,cdiv,0.1
    lesize,9,,,cdiv
    lesize,11,,,cdiv
    lesize,10,,,6
    l,1,9                 ! line 13
    l,4,5                 ! line 14
    l,8,12                ! line 15
    lsel,s,line,,13,15,2
    lesize,all,,,vdiv,8
    l,7,11                ! line 16
    lesize,16,,,vdiv,8   ! 10 divisions, 4x size difference
    l,2,10                ! line 17
    lesize,17,,,vdiv,8   ! same as previous
    l,3,6                 ! line 18
    lesize,18,,,2
    ! create areas for element 121
    a,2,3,6,7,11,10                 ! area 4
    a,7,8,12,11                     ! area 5
    a,1,2,10,9                      ! area 6
    a,4,5,6,3                       ! area 7
    ! now make areas for outer elements
    rectng,0,2*bplater,-1.5*hgt,1.5*hgt    ! area 8
    l,9,13                 ! line 23
    l,10,14                ! line 24
    l,11,15                ! line 25
    l,12,16                ! line 26
    a,13,9,10,14           ! area 9
    a,14,10,11,15          ! area 10
    a,15,11,12,16          ! area 11
    lsel,s,line,,23,26
    lesize,all,,,1                  ! need just 1 element in gap
    lsel,s,line,,19
    lesize,19,,,cdiv,4
    lsel,s,line,,21
    lesize,21,,,cdiv,0.25
    lsel,s,line,,20
    lesize,20,,,6
    !
    ! Commands for element type, meshing.
    et,1,plane121,,,1,,,,         ! area elements for efield
    mp,perx,1,1                   ! efield relative permeability
    mat,1                         ! using material number 1
    mshkey,2
    amesh,4,7                     ! mesh the four inside areas
    et,2,infin110,1,0,1           ! boundary elements, axisymmetric
    mshkey,2
    amesh,9,11                    ! mesh outer areas
    lsel,s,line,,19,21            ! outside lines
    sfl,all,inf                   ! set these lines to infinity
    !
    ! Applying voltages to nodes at lines
    !lsel,s,,,9,12,,1     ! select lines 9-12 plus nodes, etc.
    !d,all,volt,0                 ! apply 0 volts at outer boundary nodes
    lsel,s,,,1,4,,1      ! select lower (ground) plate
    d,all,volt,V0            ! set voltage these nodes
    lsel,s,,,5,8,,1      ! select upper (tilted) plate
    d,all,volt,V1           ! set voltage these nodes
    allsel
    /gst,on
    save
    finish
    !
    /solution              ! running solver
    solve
    finish
    !
    /post1
```

```
    etable,sene,sene           ! calculating capacitance
    ssum
    *get,W,ssum,,item,sene
    C=(W*2)/((V1-V0)**2)
    *status,C
    finish
```

Code for Flat Surfaces

The following code uses the actual geometry of the capacitance gage probe, including the geometry of the guard ring. The capacitance of each pair of capacitors is calculated for a given spacing, then the values of interest are stored in a matrix *C*. Fifteen separate analyses are completed to determine the capacitance values over the entire active range of the gage. These flat surface values are used as reference points when determining the correction for spherical surfaces.

```
    finish
    /clear                    ! used to erase and start over analysis
    !
    /title, Axisymmetric Capacitance Gage, Actual Geometry
    !
    ! With version 7, changing line numbers to accommodate selection
    !
    ! Incremental changes: took out solver, this just creates geometry
    !
    ! This code produces a capacitance that is the sum of all energy in the gaps.
    ! Use this as a starting point to do the more sophisticated and automated process.
    !
    /prep7
    !
    ! Defining the geometry of
    ! the actual capacitance gage sensor
    ! Set units to mm, microfarads
    !
    emunit,epzro,8.854e-9   !epsilon in uF per mm
    !
    ! Define Dimensions of the capacitance gage
    !
    innerb=0.0675    ! Inner brass capacitance diameter, inches
    innerp=0.1249    ! Inner plastic diameter, inches
    flatdia=0.200    ! Diameter of flat area
    outerb=0.300      ! Outer brass diameter, inches
    outerp=0.330     ! Outer plastic diameter, inches
    ss=0.375         ! Stainless steel outer diameter inches
    V0=-5.0          ! voltage of base plate
    V1=5.0           ! voltage of upper plate
    gapinitmi=5.8    ! Initial gap setting in minch *********************
    gapincmi=0.2     ! Increment of the gap distance in minch
    depin=0.045      ! Depth of cap gage in inches
    slp=20           ! Upwards slope of gage in degrees
    TestDia=0.625    ! Diameter of test sphere, inches
    Agap=0.2         ! Air gap around cap gage, mm
    Cflg=0.0         ! Set to zero for flat surface, otherwise round
    Nr=1.0           ! Use to refine the mesh, 2 quadruples elements, etc
    !
    ! Convert measurements to metric and radii
    !
    innerbr=innerb*25.4/2
    innerpr=innerp*25.4/2
    flatrad=flatdia*25.4/2
    outerbr=outerb*25.4/2
```

```
   outerpr=outerp*25.4/2
   ssr=ss*25.4/2
   dep=depin*25.4
   gapinc=gapincmi*0.0254
   gapinit=gapinitmi*0.0254
   halfpt=(innerbr+innerpr)/2    ! Halfway across plastic spacer
   TestR=TestDia*25.4/2
   SimEdg=1.1*ssr                 ! Edge of simulation, fix later
   !
   ! Keypoint y values
   !
   k26y=(outerbr-flatrad)*tan(slp*3.1415926/180)
   k27y=(outerpr-flatrad)*tan(slp*3.1415926/180)
   k28y=(ssr-flatrad)*tan(slp*3.14159/180)
   k42y=TestR-(TestR**2-Cflg*innerbr**2)**0.5
   k43y=TestR-(TestR**2-Cflg*halfpt**2)**0.5
   k44y=TestR-(TestR**2-Cflg*innerpr**2)**0.5
   k45y=TestR-(TestR**2-Cflg*flatrad**2)**0.5
   k46y=TestR-(TestR**2-Cflg*outerbr**2)**0.5
   k47y=TestR-(TestR**2-Cflg*outerpr**2)**0.5
   k48y=TestR-(TestR**2-Cflg*ssr**2)**0.5
   k49y=TestR-(TestR**2-Cflg*(ssr+Agap)**2)**0.5
   k50y=TestR-(TestR**2-Cflg*SimEdg**2)**0.5
   !
   ! Center of sphere keypoint
   !
   k,100,0,-TestR
   !
   ! Use same coordinate system for everything
   !
   csys,0
   !
   ! Set the number of loops for the calculation
   G=1                ! number of different gaps to use*************
   *dim,C,table,G,2,1  ! dimension the capacitance array
   !
   ! *******************************************************
   ! Begin Loop Here
   *do,I,1,G
   /prep7
   gap=gapinit+gapinc*(I-1)
   tp=gap+dep
   !
   ! Next 3 lines erase all elements to start over geometry
   !
   asel,all
   aclear,all
   adele,all,,,1
   !
   ! Define keypoints of cap gage and ref surface
   !
   k,1,0,tp
   k,2,innerbr,tp
   k,3,halfpt,tp
   k,4,innerpr,tp
   k,5,flatrad,tp
   k,6,outerbr,tp
   k,7,outerpr,tp
   k,8,ssr,tp
   k,9,ssr+Agap,tp
   k,10,SimEdg,tp
   !
   k,21,0,gap
   k,22,innerbr,gap
   k,23,halfpt,gap
   k,24,innerpr,gap
   k,25,flatrad,gap
   k,26,outerbr,gap+k26y
```

```
k,27,outerpr,gap+k27y
k,28,ssr,gap+k28y
k,29,ssr+Agap,gap+k28y
k,30,SimEdg,gap+k28y
!
k,41,0,0
k,42,innerbr,-k42y
k,43,halfpt,-k43y
k,44,innerpr,-k44y
k,45,flatrad,-k45y
k,46,outerbr,-k46y
k,47,outerpr,-k47y
k,48,ssr,-k48y
k,49,ssr+Agap,-k49y
k,50,SimEdg,-k50y
!
! Create All Lines, Horizontals first
! Also breaking into segments for elements as needed
!
l,1,2               ! line 1
l,2,3,32*Nr,4       ! line 2
l,3,4,8*Nr,1        ! line 3
l,4,5               ! line 4
l,5,6               ! line 5
l,6,7,8*Nr,1        ! line 6
l,7,8               ! line 7
l,8,9,8*Nr,1        ! line 8
l,9,10,1,1          ! line 9, inf flag
l,22,23,32*Nr,4     ! line 10 (old 11)
l,23,24,8*Nr,1      ! line 11 (old 12)
l,26,27,8*Nr,1      ! line 12 (old 15)
l,28,29,8*Nr,1      ! line 13 (old 17)
l,29,30,1,1         ! line 14 (old 18), inf flag
!
! Need to make the following 9 lines curved for sphere
!
l,41,42,50*Nr,0.25 ! line 15 (old 19)
l,42,43,32*Nr,4     ! line 16 (old 20)
l,43,44,8*Nr,1      ! line 17 (old 21)
l,44,45,24*Nr,1     ! line 18 (old 22)
l,45,46,24*Nr,1     ! line 19 (old 23)
l,46,47,8*Nr,1      ! line 20 (old 24)
l,47,48,8*Nr,1      ! line 21 (old 25)
l,48,49,8*Nr,1      ! line 22 (old 26)
l,49,50,1,1         ! line 23 (old 27)
!
l,21,1              ! line 24 (old 28)
l,23,3,64*Nr,4      ! line 25 (old 30)
l,25,5              ! line 26 (old 32)

l,29,9,12*Nr,1      ! line 27 (old 36)
l,30,10,12*Nr,1     ! line 28 (old 37)
!
l,21,41,16*Nr,3     ! line 29 (old 38)
l,22,42,16*Nr,3     ! line 30 (old 39)
l,23,43,16*Nr,3     ! line 31 (old 40)
l,24,44,16*Nr,3     ! line 32 (old 41)
l,25,45,16*Nr,3     ! line 33 (old 42)
l,26,46,16*Nr,3     ! line 34 (old 43)
l,27,47,16*Nr,3     ! line 35 (old 44)
l,28,48,16*Nr,3     ! line 36 (old 45)
l,29,49,16*Nr,3     ! line 37 (old 46)
l,30,50,16*Nr,3     ! line 38 (old 47)
!
! New lines for conductors
!
l,21,22,50*Nr,0.25 ! line 39 (old 10)
l,22,2,64*Nr,4      ! line 40 (old 29)
```

```
      l,24,4,64*Nr,4      ! line 41 (old 31)
      l,26,6,32*Nr,4      ! line 42 (old 33)
      l,24,25,24*Nr,1     ! line 43 (old 13)
      l,25,26,24*Nr,1     ! line 44 (old 14)
      l,27,7,32*Nr,4      ! line 45 (old 34)
      l,28,8,12*Nr,2      ! line 46 (old 35)
      l,27,28,8*Nr,1      ! line 47 (old 16)
      !
      ! Define areas, all new numbers
      !
      al,1,24,39,40     ! area 1
      al,2,40,10,25     ! area 2
      al,3,25,11,41     ! area 3
      al,4,41,43,26     ! area 4
      al,5,26,44,42     ! area 5
      al,6,42,12,45     ! area 6
      al,7,45,47,46     ! area 7
      al,8,46,13,27     ! area 8
      al,9,27,14,28     ! area 9
      !
      al,39,29,15,30    ! area 10
      al,10,30,16,31    ! area 11
      al,11,31,17,32    ! area 12
      al,43,32,18,33    ! area 13
      al,44,33,19,34    ! area 14
      al,12,34,20,35    ! area 15
      al,47,35,21,36    ! area 16
      al,13,36,22,37    ! area 17
      al,14,37,23,38    ! area 18
      !
      ! Element type and meshing, still need to modify this code
      ! to account for plastic permeability, correct areas to select
      ! No changes made to code below this point
      !
      !shpp,modify,1,500          ! modify aspect ratio warning
      et,1,plane121,,,1,,,,       ! area elements for efield
      mp,perx,1,1                 ! efield relative permeability
      mat,1                       ! using material number 1 (air)
      mat,2                       ! defining type 2
      mp,perx,2,3.8               ! setting permeability material 2 (plastic)
      mshkey,2
      !
      ! Select all nonconductive areas and mesh
      !
      asel,s,area,,2,3            ! S for new selection, plastic area
      asel,a,area,,6,6            ! Add plastic section 6
      amesh,all                  ! mesh with type 2 material

      mat,1                      ! back to material type 1 (air)
      asel,s,area,,8,8           ! Air gap on side of gage
      asel,a,area,,10,17         ! Last of the air gaps
      amesh,all                  ! mesh all selected areas
      !
      et,2,infin110,1,0,1        ! infinite boundary elements, axisymmetric
      mshkey,2
      asel,s,area,,9,9           ! first infinite area
      asel,a,area,,18,18         ! second infinite area
      amesh,all                  ! mesh infinite sections
      !
      lsel,s,,,9,9               ! upper edge
      lsel,a,,,28,28             ! right edge
      lsel,a,,,38,38             ! right edge
      sfl,all,inf                ! set these lines to infinity
      !
      ! Applying voltages to nodes on certain lines
      !
      lsel,s,,,39,40,,1          ! selecting center conductor
      !d,all,volt,V1             ! apply V1 volts to center conductor
```

```
    cm,cond1,node                ! Define 1st conductor for cmatrix analysis

    lsel,s,,,41,44,,1            ! select ground ring
    !d,all,volt,V1               ! set voltage ground ring same as center
    cm,cond2,node

    lsel,s,,,45,47,,1            ! select outer shield
    !d,all,volt,0                ! set voltage of shield to ground
    cm,cond3,node

    lsel,s,,,15,23,,1            ! select lower sphere or plate
    !d,all,volt,V0               ! set voltage to V0
    cm,cond4,node
    !
    !
    allsel,all
    /gst,off                        ! graphical solution tracking off
    save
    finish
    !
    /solution                       ! running solver
    cmatrix,1,'cond',4,1,'cmat'  ! solves for all cap values
    finish
    !
    /post1
    C(I,1)=gap                       ! first value is current gap
    C(I,2)=cmat(1,4,2)               ! pulling correct value from table
    finish
    !
    *enddo
    !
    ! End of Loop
    ! ************************************************************
    !
    ! Output resulting table data to a file
    !
    /post1
    /output,flatres,txt
    *mwrite,C(1,1)
    (F10.6, E18.7)
    /output
    finish
```

Code for Spherical Surfaces

The code below for spherical target surfaces is nearly identical to the code used for flat surfaces. The number of lines, areas, and elements in the mesh all remain constant, only the location of the keypoints and the shape of the target surface changes. The capacitance values from this analysis are compared and contrasted to the flat case. Note that this code is for one radius of curvature only, and that the starting distance between the conductors is changed so that the ranges of capacitance values overlap.

```
    finish
    /clear                  ! used to erase and start over analysis
    !
    /title, Axisymmetric Capacitance Gauge, Actual Geometry
    !
    ! With version 7, changing line numbers to accomodate selection
```

```
!
! Incremental changes: took out solver, this just creates geometry
!
! This code produces a capacitance that is the sum of all energy in the gaps.
! Use this as a starting point to do the more sophisticated and automated process.
!
/prep7
!
! Defining the geometry of
! the actual capacitance gauge sensor
! Set units to mm, microfarads
!
emunit,epzro,8.854e-9    !epsilon in uF per mm
!
! Define Dimensions of the capacitance gauge
!
innerb=0.0675    ! Inner brass capacitance diameter, inches
innerp=0.1249    ! Inner plastic diameter, inches
flatdia=0.200    ! Diameter of flat area
outerb=0.300     ! Outer brass diameter, inches
outerp=0.330     ! Outer plastic diameter, inches
ss=0.375         ! Stainless steel outer diameter inches
V0=-5.0          ! voltage of base plate
V1=5.0           ! voltage of upper plate
gapinitmi=0.02   ! Initial gap setting in minch *********************
gapincmi=0.04    ! Increment of the gap distance in minch
depin=0.045      ! Depth of cap gauge in inches
slp=20           ! Upwards slope of gauge in degrees
TestDia=0.500    ! Diameter of test sphere, inches ******************
Agap=0.2         ! Air gap around cap gauge, mm
Cflg=1.0         ! Set to zero for flat surface, otherwise round
Nr=1.0           ! Use to refine the mesh, 2 quadruples elements, etc
!
! Convert measurements to metric and radii
!
innerbr=innerb*25.4/2
innerpr=innerp*25.4/2
flatrad=flatdia*25.4/2
outerbr=outerb*25.4/2
outerpr=outerp*25.4/2
ssr=ss*25.4/2
dep=depin*25.4
gapinc=gapincmi*0.0254
gapinit=gapinitmi*0.0254
halfpt=(innerbr+innerpr)/2    ! Halfway across plastic spacer
TestR=TestDia*25.4/2
SimEdg=1.1*ssr                ! Edge of simulation, fix later
!
! Keypoint y values
!
k26y=(outerbr-flatrad)*tan(slp*3.1415926/180)
k27y=(outerpr-flatrad)*tan(slp*3.1415926/180)
k28y=(ssr-flatrad)*tan(slp*3.14159/180)
k42y=TestR-(TestR**2-Cflg*innerbr**2)**0.5
k43y=TestR-(TestR**2-Cflg*halfpt**2)**0.5
k44y=TestR-(TestR**2-Cflg*innerpr**2)**0.5
k45y=TestR-(TestR**2-Cflg*flatrad**2)**0.5
k46y=TestR-(TestR**2-Cflg*outerbr**2)**0.5
k47y=TestR-(TestR**2-Cflg*outerpr**2)**0.5
k48y=TestR-(TestR**2-Cflg*ssr**2)**0.5
k49y=TestR-(TestR**2-Cflg*(ssr+Agap)**2)**0.5
k50y=TestR-(TestR**2-Cflg*SimEdg**2)**0.5
!
! Center of sphere keypoint
!
k,100,0,-TestR
!
! Use same coordinate system for everything
```

```
!
csys,0
!
! Set the number of loops for the calculation
G=15                  ! number of different gaps to use*************
*dim,C,table,G,2,1  ! dimension the capacitance array
!
! ********************************************************
! Begin Loop Here
*do,I,1,G
/prep7
gap=gapinit+gapinc*(I-1)
tp=gap+dep
!
! Next 3 lines erase all elements to start over geometry
!
asel,all
aclear,all
adele,all,,,1
!
! Define keypoints of cap gauge and ref surface
!
k,1,0,tp
k,2,innerbr,tp
k,3,halfpt,tp
k,4,innerpr,tp
k,5,flatrad,tp
k,6,outerbr,tp
k,7,outerpr,tp
k,8,ssr,tp
k,9,ssr+Agap,tp
k,10,SimEdg,tp
!
k,21,0,gap
k,22,innerbr,gap
k,23,halfpt,gap
k,24,innerpr,gap
k,25,flatrad,gap
k,26,outerbr,gap+k26y
k,27,outerpr,gap+k27y
k,28,ssr,gap+k28y
k,29,ssr+Agap,gap+k28y
k,30,SimEdg,gap+k28y
!
k,41,0,0
k,42,innerbr,-k42y
k,43,halfpt,-k43y
k,44,innerpr,-k44y
k,45,flatrad,-k45y
k,46,outerbr,-k46y
k,47,outerpr,-k47y
k,48,ssr,-k48y
k,49,ssr+Agap,-k49y
k,50,SimEdg,-k50y
!
! Create All Lines, Horizontals first
! Also breaking into segments for elements as needed
!
l,1,2               ! line 1
l,2,3,48*Nr,4       ! line 2
l,3,4,24*Nr,1       ! line 3
l,4,5               ! line 4
l,5,6               ! line 5
l,6,7,8*Nr,1        ! line 6
l,7,8               ! line 7
l,8,9,8*Nr,1        ! line 8
l,9,10,1,1          ! line 9, inf flag
l,22,23,48*Nr,4     ! line 10 (old 11)
```

131

```
l,23,24,24*Nr,1      ! line 11 (old 12)
l,26,27,8*Nr,1       ! line 12 (old 15)
l,28,29,8*Nr,1       ! line 13 (old 17)
l,29,30,1,1          ! line 14 (old 18), inf flag
!
! The following 9 lines are curved for sphere, flat equivalent
! info was removed due to possible conflict
!
larc,41,42,100,TestR        ! line 15
lesize,15,,,100*Nr,0.25
larc,42,43,100,TestR        ! line 16
lesize,16,,,48*Nr,4
larc,43,44,100,TestR        ! line 17
lesize,17,,,24*Nr,1
larc,44,45,100,TestR        ! line 18
lesize,18,,,64*Nr,1
larc,45,46,100,TestR        ! line 19
lesize,19,,,48*Nr,1
larc,46,47,100,TestR        ! line 20
lesize,20,,,8*Nr,1
larc,47,48,100,TestR        ! line 21
lesize,21,,,8*Nr,1
larc,48,49,100,TestR        ! line 22
lesize,22,,,8*Nr,1
larc,49,50,100,TestR        ! line 23
lesize,23,,,1,1
!
l,21,1               ! line 24 (old 28)
l,23,3,64*Nr,4       ! line 25 (old 30)
l,25,5               ! line 26 (old 32)

l,29,9,12*Nr,1       ! line 27 (old 36)
l,30,10,12*Nr,1      ! line 28 (old 37)
!
l,21,41,12*Nr,3      ! line 29 (old 38)
l,22,42,12*Nr,3      ! line 30 (old 39)
l,23,43,12*Nr,3      ! line 31 (old 40)
l,24,44,12*Nr,3      ! line 32 (old 41)
l,25,45,12*Nr,3      ! line 33 (old 42)
l,26,46,12*Nr,3      ! line 34 (old 43)
l,27,47,12*Nr,3      ! line 35 (old 44)
l,28,48,12*Nr,3      ! line 36 (old 45)
l,29,49,12*Nr,3      ! line 37 (old 46)
l,30,50,12*Nr,3      ! line 38 (old 47)
!
! New lines for conductors
!
l,21,22,100*Nr,0.25 ! line 39 (old 10)
l,22,2,64*Nr,4       ! line 40 (old 29)
l,24,4,64*Nr,4       ! line 41 (old 31)
l,26,6,32*Nr,4       ! line 42 (old 33)
l,24,25,64*Nr,1      ! line 43 (old 13)
l,25,26,48*Nr,1      ! line 44 (old 14)
l,27,7,32*Nr,4       ! line 45 (old 34)
l,28,8,12*Nr,2       ! line 46 (old 35)
l,27,28,8*Nr,1       ! line 47 (old 16)
!
! Define areas, all new numbers
!
al,1,24,39,40     ! area 1
al,2,40,10,25     ! area 2
al,3,25,11,41     ! area 3
al,4,41,43,26     ! area 4
al,5,26,44,42     ! area 5
al,6,42,12,45     ! area 6
al,7,45,47,46     ! area 7
al,8,46,13,27     ! area 8
al,9,27,14,28     ! area 9
```

```
!
al,39,29,15,30   ! area 10
al,10,30,16,31   ! area 11
al,11,31,17,32   ! area 12
al,43,32,18,33   ! area 13
al,44,33,19,34   ! area 14
al,12,34,20,35   ! area 15
al,47,35,21,36   ! area 16
al,13,36,22,37   ! area 17
al,14,37,23,38   ! area 18
!
! Element type and meshing, still need to modify this code
! to account for plastic permeability, correct areas to select
! No changes made to code below this point
!
!shpp,modify,1,500          ! modify aspect ratio warning
et,1,plane121,,,1,,,,       ! area elements for efield
mp,perx,1,1                 ! efield relative permeability
mat,1                       ! using material number 1 (air)
mat,2                       ! defining type 2
mp,perx,2,3.8               ! setting permeability material 2 (plastic)
mshkey,2
!
! Select all nonconductive areas and mesh
!
asel,s,area,,2,3            ! S for new selection, plastic area
asel,a,area,,6,6            ! Add plastic section 6
amesh,all                  ! mesh with type 2 material

mat,1                       ! back to material type 1 (air)
asel,s,area,,8,8            ! Air gap on side of gage
asel,a,area,,10,17          ! Last of the air gaps
amesh,all                  ! mesh all selected areas
!
et,2,infin110,1,0,1         ! infinite boundary elements, axisymmetric
mshkey,2
asel,s,area,,9,9            ! first infinite area
asel,a,area,,18,18          ! second infinite area
amesh,all                  ! mesh infinite sections
!
lsel,s,,,9,9                ! upper edge
lsel,a,,,28,28              ! right edge
lsel,a,,,38,38              ! right edge
sfl,all,inf                 ! set these lines to infinity
!
! Applying voltages to nodes on certain lines
!
lsel,s,,,39,40,,1           ! selecting center conductor
!d,all,volt,V1              ! apply V1 volts to center conductor
cm,cond1,node               ! Define 1st conductor for cmatrix analysis

lsel,s,,,41,44,,1           ! select ground ring
!d,all,volt,V1              ! set voltage ground ring same as center
cm,cond2,node

lsel,s,,,45,47,,1           ! select outer shield
!d,all,volt,0               ! set voltage of shield to ground
cm,cond3,node

lsel,s,,,15,23,,1           ! select lower sphere or plate
!d,all,volt,V0              ! set voltage to V0
cm,cond4,node
!
!
allsel,all
!/gst,off                   ! turns off graphical solution tracking
save
finish
```

```
!
/solution                       ! running solver
cmatrix,1,'cond',4,1,'cmat'  ! solves for all cap values ****************
finish
!
/post1
C(I,1)=gap                       ! first value is current gap
C(I,2)=cmat(1,4,2)               ! pulling correct value from table
finish
!
*enddo
!
! End of Loop
! ************************************************************
!
! Output resulting table data to a file
!
/post1
/output,r50v0500,txt
*mwrite,C(1,1)
(F10.6, E18.7)
/output
finish
```

Appendix C:
Matlab Code for Analysis

Capacitance and Distance Calculations

Below is the Matlab file analyze50Vimp.m, which loads the data from the capacitance calculations and produces polynomial fits between real and measured distances. This file is for the ultrafine gain setting, but a nearly identical file is used to determine the polynomial fits for the fine gain setting, with only the initial data changing.

```
% Analyze results from Ansys
% This file is for work for 50V data,
% to compare to empirical measurements
%
close all;
clear all;

% This data from file Results50Vflat.txt
rawf=[0.018288     0.1434233E-05
  0.019304     0.1369051E-05
  0.020320     0.1310086E-05
  0.021336     0.1256464E-05
  0.022352     0.1207471E-05
  0.023368     0.1162515E-05
  0.024384     0.1121103E-05
  0.025400     0.1082818E-05
  0.026416     0.1047307E-05
  0.027432     0.1014271E-05
  0.028448     0.9834500E-06
  0.029464     0.9546216E-06
  0.030480     0.9275919E-06
  0.031496     0.9021915E-06
  0.032512     0.8782723E-06];
%
% New data for different diameter spheres analyzed week of
% 6/9/03. Distance values are different so that the
% C ranges approximate that of the flat system. Raw data
% files are Results50v1000b.txt, etc. No 0.25 data this time.
%
raw0375=[0.000508     0.1450724E-05
  0.001524     0.1162308E-05
  0.002540     0.1029579E-05
  0.003556     0.9430071E-06
  0.004572     0.8789629E-06
  0.005588     0.8283043E-06
  0.006604     0.7865214E-06
  0.007620     0.7510553E-06
  0.008636     0.7203132E-06
  0.009652     0.6932360E-06
  0.010668     0.6690841E-06
  0.011684     0.6473202E-06
  0.012700     0.6275419E-06
  0.013716     0.6094399E-06
  0.014732     0.5927716E-06];
```

```
%
raw0500=[0.000508     0.1821639E-05
  0.001524     0.1438404E-05
  0.002540     0.1262719E-05
  0.003556     0.1148545E-05
  0.004572     0.1064376E-05
  0.005588     0.9980241E-06
  0.006604     0.9434770E-06
  0.007620     0.8973238E-06
  0.008636     0.8574416E-06
  0.009652     0.8224196E-06
  0.010668     0.7912724E-06
  0.011684     0.7632846E-06
  0.012700     0.7379204E-06
  0.013716     0.7147686E-06
  0.014732     0.6935061E-06];
%
% The following are from the "b" files, Results50V0625b.txt etc.
%
raw0625=[0.002032     0.1566080E-05
  0.003048     0.1394565E-05
  0.004064     0.1274906E-05
  0.005080     0.1183601E-05
  0.006096     0.1110183E-05
  0.007112     0.1049072E-05
  0.008128     0.9969377E-06
  0.009144     0.9516351E-06
  0.010160     0.9117000E-06
  0.011176     0.8760892E-06
  0.012192     0.8440332E-06
  0.013208     0.8149488E-06];
%
raw0750=[0.002540     0.1660855E-05
  0.003556     0.1493410E-05
  0.004572     0.1370833E-05
  0.005588     0.1274850E-05
  0.006604     0.1196449E-05
  0.007620     0.1130521E-05
  0.008636     0.1073887E-05
  0.009652     0.1024437E-05
  0.010668     0.9806982E-06
  0.011684     0.9416030E-06
  0.012700     0.9063526E-06
  0.013716     0.8743340E-06];
%
raw0875=[0.004572     0.1500872E-05
  0.005588     0.1390900E-05
  0.006604     0.1301350E-05
  0.007620     0.1226266E-05
  0.008636     0.1161948E-05
  0.009652     0.1105938E-05
  0.010668     0.1056523E-05
  0.011684     0.1012460E-05
  0.012700     0.9728228E-06
  0.013716     0.9368989E-06
  0.014732     0.9041318E-06
  0.015748     0.8740780E-06];
%
raw1000=[0.006096     0.1443223E-05
  0.007112     0.1351868E-05
  0.008128     0.1274599E-05
  0.009144     0.1208003E-05
  0.010160     0.1149752E-05
  0.011176     0.1098194E-05
  0.012192     0.1052111E-05
  0.013208     0.1010583E-05
  0.014224     0.9728968E-06
  0.015240     0.9384897E-06
```

```
   0.016256     0.9069101E-06
   0.017272     0.8777905E-06];
%
% Separate out the variables into two
% columns for each diameter plus flat data
%
drealf=rawf(:,1); Cf=rawf(:,2);
dreal0375=raw0375(:,1); Cr0375=raw0375(:,2);
dreal0500=raw0500(:,1); Cr0500=raw0500(:,2);
dreal0625=raw0625(:,1); Cr0625=raw0625(:,2);
dreal0750=raw0750(:,1); Cr0750=raw0750(:,2);
dreal0875=raw0875(:,1); Cr0875=raw0875(:,2);
dreal1000=raw1000(:,1); Cr1000=raw1000(:,2);
%
% Invert the capacitance values and convert to pF-1
% NEW change for improved curve fitting
%
Cfinv=1./Cf*1e-6;
Crinv0375=1./Cr0375*1e-6;
Crinv0500=1./Cr0500*1e-6;
Crinv0625=1./Cr0625*1e-6;
Crinv0750=1./Cr0750*1e-6;
Crinv0875=1./Cr0875*1e-6;
Crinv1000=1./Cr1000*1e-6;
%
% Convert all distances to minches for plotting
%
drealfin=drealf/0.0254;
dreal0375in=dreal0375/0.0254;
dreal0500in=dreal0500/0.0254;
dreal0625in=dreal0625/0.0254;
dreal0750in=dreal0750/0.0254;
dreal0875in=dreal0875/0.0254;
dreal1000in=dreal1000/0.0254;
%
% Determine polynomial fit to curved data, use 4th order
% to ensure good fit
%
P0375b=polyfit(Crinv0375,dreal0375,4);
P0500b=polyfit(Crinv0500,dreal0500,4);
P0625b=polyfit(Crinv0625,dreal0625,4);
P0750b=polyfit(Crinv0750,dreal0750,4);
P0875b=polyfit(Crinv0875,dreal0875,4);
P1000b=polyfit(Crinv1000,dreal1000,4);
%
% Use coeffs to interpolate 15 new "real" values
%
drealint0375=polyval(P0375b,Cfinv)/0.0254;
drealint0500=polyval(P0500b,Cfinv)/0.0254;
drealint0625=polyval(P0625b,Cfinv)/0.0254;
drealint0750=polyval(P0750b,Cfinv)/0.0254;
drealint0875=polyval(P0875b,Cfinv)/0.0254;
drealint1000=polyval(P1000b,Cfinv)/0.0254;
%
% Determine complete coefficients for curve
%
Pb0375=polyfit(drealfin,drealint0375,4);
Pb0500=polyfit(drealfin,drealint0500,4);
Pb0625=polyfit(drealfin,drealint0625,4);
Pb0750=polyfit(drealfin,drealint0750,4);
Pb0875=polyfit(drealfin,drealint0875,4);
Pb1000=polyfit(drealfin,drealint1000,4);
%
% Determine linear slope of real d to measured d over full range
%
Pc0375=polyfit(drealint0375,drealfin,1);
Pc0500=polyfit(drealint0500,drealfin,1);
Pc0625=polyfit(drealint0625,drealfin,1);
```

137

```
Pc0750=polyfit(drealint0750,drealfin,1);
Pc0875=polyfit(drealint0875,drealfin,1);
Pc1000=polyfit(drealint1000,drealfin,1);
%
% Fit only active area of curve
% Can't use this code, not enough data points
%
Pc0375b=polyfit(drealint0375(3:13),drealfin(3:13),1);
Pc0500b=polyfit(drealint0500(3:13),drealfin(3:13),1);
Pc0625b=polyfit(drealint0625(3:13),drealfin(3:13),1);
Pc0750b=polyfit(drealint0750(3:13),drealfin(3:13),1);
Pc0875b=polyfit(drealint0875(3:13),drealfin(3:13),1);
Pc1000b=polyfit(drealint1000(3:13),drealfin(3:13),1);
%
% Combine these slopes into a matrix to present as results
Slps=[0.375 Pc0375(1)*50
      0.500 Pc0500(1)*50
      0.625 Pc0625(1)*50
      0.750 Pc0750(1)*50
      0.875 Pc0875(1)*50
      1.000 Pc1000(1)*50];
%
% For plotting purposes fit lines to raw data
dreal0375line=polyval(polyfit(Crinv0375,dreal0375in,1),Crinv0375);
dreal0500line=polyval(polyfit(Crinv0500,dreal0500in,1),Crinv0500);
dreal0625line=polyval(polyfit(Crinv0625,dreal0625in,1),Crinv0625);
dreal0750line=polyval(polyfit(Crinv0750,dreal0750in,1),Crinv0750);
dreal0875line=polyval(polyfit(Crinv0875,dreal0875in,1),Crinv0875);
dreal1000line=polyval(polyfit(Crinv1000,dreal1000in,1),Crinv1000);
%
%
SlpsB=[0.375 Pc0375b(1)*50 dreal0375line(8)
      0.500 Pc0500b(1)*50 dreal0500line(8)
      0.625 Pc0625b(1)*50 dreal0625line(8)
      0.750 Pc0750b(1)*50 dreal0750line(8)
      0.875 Pc0875b(1)*50 dreal0875line(8)
      1.000 Pc1000b(1)*50 dreal1000line(8)]
%
% Plotting routines newly added
figure(1)
set(1,'PaperPositionMode','Manual')
set(1,'Position',[0 0 6.5*72 4.25*72])
set(1,'PaperPosition',[0 0 6.5 4.25])
%
% Plot Commands Here
plot(dreal0375in*0.0254,Crinv0375,'vk')
hold on
plot(dreal0500in*0.0254,Crinv0500,'sk')
plot(dreal0625in*0.0254,Crinv0625,'^k')
plot(dreal0750in*0.0254,Crinv0750,'dk')
plot(dreal0875in*0.0254,Crinv0875,'+k')
plot(dreal1000in*0.0254,Crinv1000,'xk')
%
plot(dreal0375line*0.0254,Crinv0375,'k')
plot(dreal0500line*0.0254,Crinv0500,'k')
plot(dreal0625line*0.0254,Crinv0625,'k')
plot(dreal0750line*0.0254,Crinv0750,'k')
plot(dreal0875line*0.0254,Crinv0875,'k')
plot(dreal1000line*0.0254,Crinv1000,'k')
%
grid on
legend('9.53 mm dia.','12.7 mm dia.','15.88 mm dia.','19.05 mm dia.','22.23 mm
        dia.','25.4 mm dia.',4)
axis([-0.003 0.03 0.2 1.8])
ylabel('Inverse Capacitance, pF^-^1');
xlabel('Distance, mm');
print -deps RoundUltraHigh.eps          %export figure to EPS format
hold off
```

138

Capacitance Tilt Calculations

The Matlab script below, from captilt3.m, uses a closed-form solution for small tilt angles

to determine the error due to tilt and plot these values.

```
% This file uses a closed-form solution from Harb, Chetwynd, and Smith
% to calculate tilt errors of capacitance gauges. This solution ignores
% fringe effects so is not exact

% captilt2 attempts to solve for the difference between the true distance
% d to the surface and the distance that a cap gauge will read, do, based
% on the assumption of parallel plates. This needs an iterative solution

close all;
clear all;

dnom=[0.1  0.2  0.3  0.4];  %nominal distances
derr=[0:0.5:40]';           %first column of solution set, mrad
rr=2.5;                     %radius of probe tip in mm
dnomlength=length(dnom);
derrlength=length(derr);
for a=1:dnomlength          %stepping through distance values
    for b=1:derrlength      %stepping through angular values
        Th=derr(b,1)*0.001;
        do=dnom(a);         %distance if perpendicular surfaces
        dg=do;              %first guess at distance
        for c=1:5           %iterative loop to solve for dg
            k(b,a)=rr*sin(2*Th)/(2*dg);
            if Th==0
                expr=0.5;
            else
                expr=(1-((1-k(b,a)^2)^0.5))/(k(b,a)^2);
            end
        dg=do*2*cos(Th)*expr;
        end
        derr(b,a+1)=100*(dg-do)/do;
    end
end

figure(1)
set(1,'PaperPositionMode','Manual')
set(1,'Position',[0 0 6.5*72 4.25*72])
set(1,'PaperPosition',[0 0 6.5 4.25])
%
plot(derr(1:9:81,1),derr(1:9:81,2),'k^',derr(1:9:81,1),derr(1:9:81,3),'ko',derr(1:9
        :81,1),derr(1:9:81,4),'kx')
hold on
plot(derr(:,1),derr(:,2),'k',derr(:,1),derr(:,3),'k',derr(:,1),derr(:,4),'k')
grid on
xlabel('Tilt angle, mrad');
ylabel('Percentage error in measurement');
%title('Percentage Error in Distance Measurements, 2.5 mm radius probe tip');
legend('0.1 optimal','0.2 optimal','0.3 optimal',2);
%axis([0.6 1.2 -4 6]);
print -deps Captilt3.eps          %export figure to EPS format
hold off
```

139

Polynomial Fitting Tests

The Matlab code below, from testpoly.m, creates polynomial fits of different orders to show the effectiveness of using higher order fits for interpolation. Conversely, higher order fits are not good for extrapolating additional data points.

```
% Using 50V data to test polynomial fits
%
close all;
clear all;

% This data from file Results50Vflat.txt
rawf=[0.018288     0.1434233E-05
  0.019304     0.1369051E-05
  0.020320     0.1310086E-05
  0.021336     0.1256464E-05
  0.022352     0.1207471E-05
  0.023368     0.1162515E-05
  0.024384     0.1121103E-05
  0.025400     0.1082818E-05
  0.026416     0.1047307E-05
  0.027432     0.1014271E-05
  0.028448     0.9834500E-06
  0.029464     0.9546216E-06
  0.030480     0.9275919E-06
  0.031496     0.9021915E-06
  0.032512     0.8782723E-06];
%
% New data for different diameter spheres analyzed week of
% 6/9/03. Distance values are different so that the
% C ranges approximate that of the flat system. Raw data
% files are Results50v1000b.txt, etc. No 0.25 data this time.
%
raw0375=[0.000508     0.1450724E-05
  0.001524     0.1162308E-05
  0.002540     0.1029579E-05
  0.003556     0.9430071E-06
  0.004572     0.8789629E-06
  0.005588     0.8283043E-06
  0.006604     0.7865214E-06];
%
% Separate out the variables into two
% columns for each diameter plus flat data
%
drealf=rawf(:,1); Cf=rawf(:,2);
dreal0375=raw0375(:,1); Cr0375=raw0375(:,2);
dreal0375in=dreal0375/0.0254;
%
% Invert the capacitance values
%
Cfinv=1./Cf*1e-6;
Crinv0375=1./Cr0375*1e-6;
%
% Next fit line to drealf=P1*Cfinv+P2 for flat surface
% This is just a check of the linearity of the flat data
%
P=polyfit(Cfinv,drealf,1);
P0375a=polyfit(Crinv0375,dreal0375,2);
P0375b=polyfit(Crinv0375,dreal0375,3);
P0375c=polyfit(Crinv0375,dreal0375,4);
%
x=[0.0:0.002:2.5];
ya=polyval(P0375a,x);
yb=polyval(P0375b,x);
```

```
yc=polyval(P0375c,x);
yain=ya/0.0254; ybin=yb/0.0254; ycin=yc/0.0254;
%
% Plot commands with sizing, etc.
figure(1);
set(1,'PaperPositionMode','Manual')
set(1,'Position',[0 0 6.5*72 4.25*72])
set(1,'PaperPosition',[0 0 6.5 4.25])
%
plot(dreal0375in*0.0254,Crinv0375,'+k')
hold on
plot(yain*0.0254,x,'-k',ybin*0.0254,x,'-.k',ycin*0.0254,x,'--k');
legend('Data','Order 2','Order 3','Order 4',2)
grid on
axis([0 0.040 0 2.5])
ylabel('Inverse Capacitance, pF^-^1');
xlabel('Distance, mm');
%
% Export figure to EPS format
print -deps Testpoly.eps
hold off
%
% Not sure what the remaining code does
%
% Convert actual (real) distances to minches
%
y2a=polyval(P0375a,Crinv0375)/0.0254;
y2b=polyval(P0375b,Crinv0375)/0.0254;
y2c=polyval(P0375c,Crinv0375)/0.0254;


drealfin=drealf/0.0254;
drealin0375=dreal0375/0.0254;

diff3=y2a-drealin0375
diff4=y2b-drealin0375
diff5=y2c-drealin0375

%
% Plug in cap values from curved surfaces to get
% dmeasin, which is the distance reading you would get
% from the cap gage electronics in inches
% Note that this does NOT include nonlinear effects from
% the flat surface. Need to redo this code
%
%dmeasin0375=polyval(P,Crinv0375)/0.0254;

drealint0375=polyval(P0375b,Cfinv)/0.0254
%figure(2)
%plot(drealfin,drealint0375,'+')
%grid on

Pc0375=polyfit(drealint0375(3:13),drealfin(3:13),1);

% Determine linear slope of real d to measured d over full range
%
%
SlpsActiv=[0.375 Pc0375(1)*50];
```

Comparison Between Theoretical and Empirical Data

Several sets of test data from Lion Precision were used to test the error removal algorithm based on the Ansys analysis of capacitance. The program below, which is contained in the file LionComp4.m, includes a set of this calibration information.

```
% Data from Lion Precision Calibration for 1.0 inch sphere 50V/mil
GapTrue=[0.233; 0.258; 0.283; 0.308; 0.333; 0.358; 0.383; 0.408; 0.433
    0.458; 0.483; 0.508; 0.533; 0.558; 0.583; 0.608; 0.633];
GapMeas=[0.191; 0.191; 0.214; 0.252; 0.290; 0.327; 0.363; 0.398; 0.433
    0.468; 0.502; 0.536; 0.570; 0.603; 0.636; 0.666; 0.668];
GapMeasNorm=GapMeas+0.567;
%
% This step assumes that coeffs have been created from empirical data
% to convert the measured data to calibrated data
%
Pb1000=[0.07846382240499 -0.40235208073235 0.83981081823174 -0.00146015186737 -
        0.06159070841960];
%
% Note that valid values are only from 4 to 14 out of 17
%
Uncorr=GapTrue-GapMeas;
err_raw=max(Uncorr(4:14))-min(Uncorr(4:14))
Corr1000=polyval(Pb1000,GapMeasNorm);
offst=Corr1000-GapTrue;
mean(offst(4:14))
err1=max(offst(4:14))-min(offst(4:14))
```

Lead Analog Design

This short program takes the system model determined from experimentation and develops an analog lead compensator for the system. This code is contained in the file LeadAnalogOnly.m.

```
% strictly analog design
s1=-1+1*j
% GzohG=303/(s1*(s1+0.55)*(0.005*s1+1))
GzohG=303/(s1*(s1+0.55))
phi=180-180/pi*angle(GzohG)
pc=50
jnk=phi+180/pi*angle(s1+pc)
zc=imag(s1)/tan(pi/180*jnk)-real(s1)
kc=1/abs(GzohG*(s1+zc)/(s1+pc))
Ts=0.010
 [numd,dend]=bilinear(kc*[1 zc],[1 pc],Ts)
```

References

[1] T. R. Hicks and P. D. Atherton, *The NanoPositioning Book, Moving and Measuring to Better than a Nanometre* (London: Queensgate Instruments and Penton Press, 1997), 50-71.

[2] L. Essen and K.D. Froome, "The Refractive Indices and Dielectric Constants of Air and its Principle Constituents at 24,000 Mc/s," *Proceedings of the Physical Society* **64** (1951), 10-B.

[3] K. S. Lion, *Instrumentation in Scientific Research* (New York: McGraw-Hill, 1959), 14-15.

[4] Ibid, 15.

[5] C. Moon and C.M. Sparks, *Journal of Research of the National Bureau of Standards* **22** (1948).

[6] Ibid, 2486.

[7] Š. Lányi, "Analysis of Linearity Errors of Inverse Capacitance Position Sensors," *Measurement Science and Technology* **9** (1998): 1762.

[8] Hicks and Atherton, Ibid, 57.

[9] M. A. Brown and C.E. Bulleid, "The Effect of Tilt and Surface Damage on Practical Capacitance Displacement Transducers," *Journal of Physics E: Scientific Instruments* **11** (1978) 429-432.

[10] M. H. W. Bonse, C. Mul, and J. W. Spronck, "Finite-Element Modelling as a Tool for Designing Capacitive Position Sensors," *Sensors and Actuators A* **46-47** (1995): 266-269.

[11] Lányi, Ibid, 1757-1764.

[12] A. E. Gee, "Fundamentals of Transducers and Instrumentation for the Precision Engineer," ASPE Tutorial, November (2001): 15-16.

[13] R. V. Jones and J. C. S. Richards. "The Design and Some Applications of Sensitive Capacitance Micrometers," *Journal of Physics E: Scientific Instruments* **6** (1973): 589-600.

[14] A. L. Hugill, "Displacement Transducers Based on Reactive Sensors in Transformer Ratio Bridge Circuits," *Journal ofPhysics E: Scientific Instruments* **15** (1982): 597-606.

[15] Calibration data, Lion Precision, type C capacitance gage, property of Precision Systems Lab, University of Kentucky.

[16] "Measurement of Out-Of-Roundness," *ANSI Standard B89.3.1-1972*, (New York: American Society of Mechanical Engineers, 1972), 22.

[17] C. J. Evans, R. J. Hocken, and W. T. Estler, "Self-Calibration: Reversal, Redundancy, Error Separation, and 'Absolute Testing'," *CIRP Annals* **45** (1996): 617-634.

[18] Evans, Hocken, and Estler, Ibid.

[19] http://www.lionprecision.com/lvdt/cap-op.html.

[20] J.-H. Zhang, L. Cai, "Profilometry using an optical stylus with interferometric readout," *Measurement Science and Technology* **8** (1997): 546-549.

[21] Bonse, Mul, and Spronck, Ibid, 266-269.

[22] K.-J. Bathe, *Finite Element Procedures* (Upper Saddle River, N. J.: Prentice Hall, 1996), 643.

[23] K. J. Binns and P. J. Lawrenson, *Analysis and Computation of Electric and Magnetic Field Problems*, (New York: Pergamon, 1973), 59-61.

[24] Calibration data, Lion Precision, type C capacitance gage, property of Precision Systems Lab, University of Kentucky.

References

[25] Machine Dynamics Research Laboratory, The Pennsylvania State University, 322 Reber Building, University Park, PA 16802.

[26] E. M. Marsh, P. Smith, R. R. Vallance, unpublished paper on the effects of non-flat surfaces on capacitance gages.

[27] Calibration data, Lion Precision, model C1-C capacitance gage, Order ID 021203-2, March 12, 2003.

[28] W. T. Thomson and M. D. Dahleh, *Theory of Vibration with Applications* (Upper Saddle River, N. J.: Prentice Hall, 1998), 33.

[29] D. S. Anderson, J. H. Burge, "Swing-arm Profilometry of Aspherics," *Optical manufacturing and testing, Proceedings SPIE* **2536** (1995): 169-179.

[30] H.M. Martin, J.H. Burge, and S.C. West, "Environmental Effects of Testing Large Astronomical Mirrors" *ASPE Proceedings of Precision Interferometric Metrology*, April 7-9 (Tucson, 1992).

[31] www.lionprecision.com/modular/3-8-cyl.html.

[32] Zhang and Cai, Ibid.

[33] Anderson and Burge, Ibid.

[34] S. Harb, D. G. Chetwynd, S. T. Smith, "Application and Performance of Capacitive Micrometry as a Super Precision Transfer Standard" *ASPE Proceedings* (Santa Fe, 1991), 17-20.

Vita

Education

Massachusetts Institute of Technology

Received a B.S. in Physics with a Minor in Music in 1991. Senior thesis documented reliability of high-speed data acquisition hardware for future use in a telescope to be built underground in Italy. Coursework included statistical physics, combinatorics and probabilities, quantum mechanics, calculus, machine design, analog circuits, and solid-state chemistry. GPA of 4.4/5.0.

University of Kentucky

Area of research is simulation and analysis of capacitive gage transducers. Courses taken include strength of materials, vibrations, finite element analysis, methods of theoretical physics, feedback control design, foundations of solid mechanics, advanced dynamics, radiation heat transfer, boundary element methods, optics, mechanics of composite materials, nonlinear oscillations, digital controls, and acoustics. GPA of 4.0/4.0.

Professional Positions Held

Texas Instruments, Versailles, Kentucky. Held position of Marketing Product Manager for ceramic capacitive pressure transducers from 1999 to 2000.

Princeton Instruments, Trenton, New Jersey. Held position of Marketing Product Manager for catadioptric UV lens and image-intensified video CCD products from 1994 to 1999. Held position of Technical Writer for all CCD camera products from 1992 to 1994.

Scholastic Honors

Recipient of Gaann Fellowship from 2000-2003.

Professional Publications

"Polishing Compacted Titanium Nitride to Optimize Growth of Nanotubes." Proceedings of the 2001 American Society for Precision Engineering Annual Meeting.

"Thermal Finite Difference Analysis of Threshold Heating for Nanoscale Machining." Proceedings of International Mechanical Engineering Conference & Exposition.

"Thermoforming of Precision Thin-Film Mirrors." Proceedings of the 2002 American Society for Precision Engineering Annual Meeting.

"Compensation of Capacitance Displacement Gages for Spherical Targets." Paper to be submitted December 2003 to the Journal of Precision Engineering.

"Nanoscale Machining with Carbon Nanotubes" Intellectual Property Update